

***In situ* X-ray Diffraction during Laser Powder Bed Fusion**

vorgelegt von
M. Sc.

Felix Schmeiser

ORCID: 0000-0001-6180-4940

von der Fakultät III - Prozesswissenschaften
der Technischen Universität Berlin
zur Erlangung des akademischen Grades

Doktor der Ingenieurwissenschaften
Dr.-Ing.

genehmigte Dissertation

Promotionsausschuss:

Vorsitzender: Priv.-Doz. Dr.-Ing. S. Müller
Gutachter: Prof. Dr. rer. nat. W. Reimers
Gutachter: Prof. Dr. rer. nat. C. Genzel

Tag der wissenschaftlichen Aussprache:
24. Mai 2022

Berlin 2022

Abstract

The *Laser Powder Bed Fusion* (LPBF) process is a generative manufacturing process, where a focused laser beam selectively melts a thin powder layer. The three-dimensional component is created layer by layer by repeating the application of a new powder layer followed by laser exposure. LPBF is becoming increasingly widespread and is the subject of much research, as the resulting material properties and possible geometric freedom are significant advantages compared to conventional manufacturing processes. At the same time, the temperature gradients associated with focused energy input lead to process instabilities and quality problems. Together with the inherent cyclic heating and cooling, a complex thermal state is the result, leading to significant residual stresses, which in the worst-case lead to cracking and failure of the manufacturing operation. In addition to the formation of residual stresses, LPBF parts inherit a characteristic microstructure, the origin of which still needs further understanding.

This thesis aims to extend the fundamental process understanding regarding the origin and evolution of internal stresses, the characteristic microstructure, and the influence of process parameters on these properties. These aims were achieved by performing *in situ* experiments with a customized LPBF system at the *High Energy Materials Science* beamline at the PETRA III synchrotron. The beamline's high energies of up to 100 keV allow experiments in transmission with a high temporal resolution to map the phenomena and mechanisms of action that occur. X-ray diffraction was used to track the evolution of lattice strains, stresses, texture, and phase composition during the LPBF process. Several underlying mechanisms of laser-matter interaction were identified by investigating a comprehensive set of process parameters and different materials.

Various thermal phenomena were demonstrated, including lateral heat accumulation in a single layer and vertical heat accumulation in the build-up direction. Additionally, a novel temperature estimation method was developed.

During the LPBF process, the stress state of the sample is changed by the laser until the very last layer. Depending on the laser parameters, a stress maximum occurs at a certain distance from the uppermost layer. This distance is increased by increasing the laser power and scanning speed. At the part edge, the stress changes from tensile to compressive with increasing distance from the top layer. The combination of low laser power and slow exposure speed resulted in a more homogeneous stress distribution than a high laser power and fast speed. It was also shown that the $\alpha \rightarrow \beta$ phase transformation in pure titanium occurs up to 400 μm below the surface during the repeated thermal cycling.

Abstract

The influence of repeated heating and cooling also affects grain growth and texture, leading to *in situ* recrystallization in areas close to the substrate. After recrystallization, an increase in diffraction peak widths was observed and attributed to the formation of micro-strains. In addition, chemical segregation effects were derived from the change in peak shape and substantiated with subsequent transmission-electronic investigations.

This thesis's findings underline the benefits and necessity of *in situ* experiments at modern synchrotron light sources. Furthermore, the acquired diffraction data revealed several phenomena only observable during the process to extend the understanding of stress formation, microstructure evolution, and phase transformations in LPBF.

Kurzfassung

Der *Laser Powder Bed Fusion* (LPBF) Prozess ist ein generatives Fertigungsverfahren, bei dem ein fokussierter Laserstrahl selektiv eine dünne Pulverschicht aufschmilzt. Durch wiederholtes Auftragen einer neuen Pulverschicht und anschließender Laserbelichtung wird ein dreidimensionales Bauteil erzeugt. LPBF findet zunehmend Verbreitung in Industrie und Forschung, da die resultierenden Materialeigenschaften und die Möglichkeiten der geometrischen Freiheit wesentliche Vorteile gegenüber konventionellen Fertigungsverfahren bieten. Gleichzeitig führen die mit dem fokussierten Energieeintrag verbundenen Temperaturgradienten zu Prozessinstabilitäten und Qualitätsproblemen. Zusammen mit dem inhärenten zyklischen Aufheizen und Abkühlen entsteht im Bauteil ein komplexer thermischer Zustand, der zur Ausbildung erheblicher Eigenspannungen führt, die zu Rissbildung, Verzug und sogar zum Abbruch des Fertigungsprozesses führen können. Neben der Bildung von Eigenspannungen weisen LPBF-Bauteile ein charakteristisches Gefüge auf, dessen Entstehungsmechanismen noch weiter erforscht werden müssen.

Ziel der vorliegenden Arbeit ist es, das grundlegende Prozessverständnis hinsichtlich der Entstehung und Entwicklung von Eigenspannungen, der charakteristischen Mikrostruktur und des Einflusses der Prozessparameter auf diese Eigenschaften zu erweitern. Um diese Ziele zu erreichen, wurden an der *High Energy Materials Science*-Beamline am PETRA III-Synchrotron *in situ*-Experimenten mit einem modifizierten LPBF-System durchgeführt. An der Beamline sind hohe Photonenenergien bis 100 keV verfügbar. Diese ermöglichen Experimente im Transmissionsmodus und, in Kombination mit dem sehr hohen Photonenfluss, eine hohe zeitliche Auflösung, um die beim LPBF-Verfahren auftretenden Phänomene und Wirkmechanismen abzubilden. Mit der Methode der Röntgenbeugung konnte die Entwicklung von Gitterdehnungen, Spannungen, der Textur und der Phasenzusammensetzung während des LPBF-Prozesses verfolgt werden. Mehrere zugrundeliegende Mechanismen der Laser-Materie-Wechselwirkung wurden durch die umfassende Untersuchung einer Reihe von Prozessparametern und verschiedener Materialien identifiziert.

Es konnten verschiedene thermische Phänomene nachgewiesen werden, darunter die laterale Wärmeakkumulation in einer einzelnen Schicht und die vertikale Wärmeakkumulation in der Aufbaurichtung. Darüber hinaus wurde eine neuartige Methode zur Temperaturabschätzung entwickelt.

Es wurde gezeigt, dass während des LPBF-Prozesses der Spannungszustand des Bauteils bis zur letzten Schicht durch den Laser beeinflusst wird. Abhängig von den Laserparametern tritt in einem bestimmten Abstand zur obersten Schicht ein Zugspannungsmaximum in der Mitte der Probe auf. Dieser Abstand vergrößert sich durch Erhöhung der Laserleistung und

der Scangeschwindigkeit. Im Gegensatz dazu wechselt das Vorzeichen der Spannung an der Bauteilkante mit zunehmendem Abstand von der obersten Schicht von Zug auf Druck. Die Kombination aus niedriger Laserleistung und langsamer Belichtungsgeschwindigkeit führte insgesamt zu einer homogenen Spannungsverteilung als eine hohe Laserleistung und schnelle Geschwindigkeit. Durch die dem Verfahren inhärente thermische Zyklierung wird die Phasenumwandlung in Reintitan mehrfach ausgelöst. Es wurde gezeigt, dass die $\alpha \rightarrow \beta$ Transformation in einer Tiefe bis zu 400 μm unterhalb der Oberfläche stattfindet.

Der Einfluss der wiederholten Erwärmung und Abkühlung wirkt sich auch auf das Kornwachstum und die Textur aus, was zu einer *in situ*-Rekristallisation in substratnahen Bereichen führt. Nach der Rekristallisation wurde eine Zunahme der Reflexbreiten beobachtet und auf die Bildung von Mikrodehnungen zurückgeführt. Darüber hinaus wurden aus der Veränderung der Reflexform chemische Segregationseffekte abgeleitet und mit anschließenden transmissionselektronenmikroskopischen Untersuchungen belegt.

Die Ergebnisse dieser Arbeit unterstreichen den Nutzen und die Notwendigkeit von *in situ*-Experimenten an modernen Synchrotronstrahlquellen. Darüber hinaus konnten anhand der Beugungsdaten mehrere Phänomene nachgewiesen werden, die nur während des Prozesses beobachtet werden können, um das Verständnis von Spannungsbildung, Mikrostrukturentwicklung und Phasenumwandlungen beim LPBF-Verfahren zu erweitern.

Table of contents

Abstract	III
Kurzfassung	V
Listings	XI
List of Figures	XI
List of Tables	XII
List of Symbols	XIII
List of Abbreviations	XIV
 I Background	 1
1 Introduction	3
Structure of this thesis	5
2 Literature review	7
2.1 Additive manufacturing of metals	7
2.1.1 Distinction to conventional manufacturing methods	7
2.1.2 The laser powder bed fusion process	9
2.1.3 Overview of laser-matter interaction	9
2.1.4 Materials for LPBF	11
2.1.5 Microstructure development in LPBF	12
2.1.5.1 Grain growth mechanisms and texture	13
2.1.5.2 Phase transformations	13
2.1.6 Residual stresses in LPBF	14
2.1.6.1 Definition and classification of residual stresses	15
2.1.6.2 Determination of residual stresses using X-ray diffraction . .	16
2.1.6.3 Residual stress analysis in LPBF applications	17
2.1.6.4 Origin of residual stresses in LPBF	19
2.1.6.5 Process parameters and their influence on residual stresses .	19
2.1.6.6 Mitigating residual stresses	22
2.2 State of the art in synchrotron technology	22
2.2.1 X-ray generation at PETRA III	23
2.2.2 Detector technology	24
2.2.3 Applications for synchrotron radiation in LPBF investigations	24

3	Aims of this work	27
4	Experimental methods	29
4.1	Conducting the <i>in situ</i> experiments	29
4.1.1	Brief description of the custom LPBF system	29
4.1.2	Experimental procedure	31
4.1.3	Calibration using LaB ₆	32
4.1.4	Materials	32
4.1.5	Process parameters	33
4.1.6	Detectors and measurement modes	35
4.2	Determining the stress-free lattice spacing d_0	36
4.2.1	Chemical composition investigations	36
4.2.2	Fabrication of specimens for d_0 investigations	37
4.2.3	Synchrotron experiments using <i>in situ</i> heating	38
4.3	Evaluation of diffraction patterns	39
4.3.1	Azimuthal integration and peak fitting	40
4.3.2	Stress calculation	41
4.3.3	Texture calculation	43
II	Publications	45
P1	In situ Microstructure Analysis of Inconel 625 during Laser Powder Bed Fusion	47
P1.1	Introduction	50
P1.2	Materials and methods	51
P1.2.1	Custom LPBF machine	51
P1.2.2	Materials	52
P1.2.3	Process parameters and measurement modes	52
P1.2.4	Experimental procedure	53
P1.2.5	Data evaluation	53
P1.3	Results	54
P1.3.1	Impact of laser irradiation on texture	54
P1.3.2	Impact of repeated laser scans on texture	56
P1.3.3	Repeated laser scanning distorts peak shape	58
P1.3.4	Ex situ microstructure analysis	59
P1.4	Discussion	59
P1.4.1	Influence of energy input	59
P1.4.2	In situ recrystallization stage	60
P1.4.3	In situ segregation stage	60
P1.5	Conclusions	61
P1.6	Acknowledgements	61
P1.7	References	62
P1.8	Evolution of preferred orientations at the edge of a sample	64

P2 Experimental observation of stress formation during selective laser melting using in situ X-ray diffraction	67
P2.1 Introduction	69
P2.2 Materials and methods	70
P2.2.1 Modified selective laser melting system	70
P2.2.2 Materials	70
P2.2.3 Experimental procedure	70
P2.2.4 In situ high energy synchrotron X-ray diffraction	71
P2.2.5 Strain-free lattice parameter	72
P2.2.6 Strain and stress analysis	73
P2.3 Results	73
P2.3.1 Influence of heat input on strains	73
P2.3.2 In-plane stresses and out-of-plane stresses	74
P2.3.3 Thermal gradient mechanism	75
P2.3.4 Thermally induced stress maximum	75
P2.3.5 Stress fields in the heat affected zone	76
P2.4 Conclusions	77
P2.5 Acknowledgements	77
P2.6 References	78
P2.7 Supplementary Information	80
P2.7.1 Supplementary Figures	80
P2.7.2 Calibration using LaB ₆	82
P2.7.3 Strain-free lattice parameter	83
P2.7.4 Temperature-dependent X-ray Elastic Constants	84
P2.8 Using <i>in situ</i> experiments to understand the part-scale stress formation and distribution	85
P2.9 Discussion of alternative data evaluation approach by Aminforoughi et al. . .	89
P3 Internal Stress Evolution and Subsurface Phase Transformation in Titanium Parts Manufactured by Laser Powder Bed Fusion – An In Situ X-Ray Diffraction Study	93
P3.1 Introduction	95
P3.2 Results and Discussion	96
P3.2.1 Evaluation of Diffraction Patterns	96
P3.2.2 Direct Observation of High-Temperature β Phase	99
P3.2.3 Phase Transformation Penetration Depth	100
P3.2.4 Parameter-Dependent Residual Stress Buildup	101
P3.2.5 Subsurface Stress Progression in a Single Layer	102
P3.3 Conclusions	103
P3.4 Experimental Section	103
P3.4.1 Modified LPBF System	103
P3.4.2 Materials	103
P3.4.3 LPBF Process Parameters and Measurement Modes	103
P3.4.4 In Situ Diffraction Experiments	104
P3.5 Acknowledgements	104

Table of contents

P3.6	References	104
III	Summary and outlook	107
5	Summary	109
6	Outlook	113
IV	Appendix	A
	References	C
	Standards and guidelines	P
	Full list of publications and related works	Q
	Acknowledgements	S

Listings

List of Figures

2.1	Classification of residual stresses by reach.	15
2.2	Schematic of crystal lattice response to stress and resulting diffraction peak shift.	16
2.3	Thermal gradient mechanism during heating and cooling.	19
2.4	X-ray sources and the evolution of their brilliance over time.	23
4.1	Schematic drawing of the LPBF system's process chamber on positioning device.	30
4.2	SEM images of feedstock material.	33
4.3	Schematic drawing of scanning strategies used in the present work.	35
4.4	Stress-free sample geometry	38
4.5	Sample environment for d_0 measurements at the P07 beamline using a furnace for <i>in situ</i> heating experiments.	39
4.6	Transforming cartesian 2D diffraction patterns to polar coordinates.	40
4.7	Steps of integration and peak analysis.	41
4.8	Schematic of the relation between diffracting lattice planes and the diffraction spots on the detector.	42
P1.1	SEM image of Inconel 625 powder.	52
P1.2	Experimental procedure.	53
P1.3	Data evaluation procedure from sector integration to peak fitting.	54
P1.4	Comparison of the influence of different energy inputs on texture.	55
P1.5	Final state texture in different build heights within a sample.	55
P1.6	Ex situ micrographs of the interface region of part and substrate for both parameter sets.	56
P1.7	Texture evolution with repeated laser passes over the gauge volume.	56
P1.8	Processing plots.	57
P1.9	Azimuthal FWHM distribution and peak shape analysis.	58
P1.10	HAADF images acquired by STEM.	59
P1.11	Sample manufactured with a laser power of $P_L = 55 \text{ W}$ and $v_L = 50 \text{ mm s}^{-1}$ observed in MM2 at $\zeta_{GV} = 200 \mu\text{m}$: Processing plots for (111) and (200) reflections. Gauge volume located at left edge of sample.	65
P2.1	a) Experimental Setup at PETRA-III P07 EH3 (DESY, Hamburg, Germany) and b) Example parts that were built using the custom SLM system.	71
P2.2	Experimental Procedure.	71

P2.3	Schematic data generation and evaluation process	72
P2.4	Strain progression for TD and BD.	73
P2.5	Strain progression in MM2, measuring position in the center of the sample. . . .	74
P2.6	Strain Progression in MM1, measuring position in the center of the sample. . . .	75
P2.7	Median d^{311} values over the whole process sorted by process parameters.	75
P2.8	Strain progression MM1, measuring position at left edge of the sample.	76
P2.9	Layer-wise median stress difference $\sigma_{TD} - \sigma_{BD}$ for complete manufacturing process in MM2.	76
P2.10	Model of the HAZ, its stress fields and the corresponding data points observed during the in situ measurements.	77
P2.11	Example diffraction patterns of a) Inconel 625 powder measured ex situ and b) bulk Inconel 625 processed by SLM measured in situ.	80
P2.12	Model representation of material's response to approaching heated zone.	81
P2.13	LaB ₆ powder diffraction pattern a) before calibration and b) after calibration and full azimuthal integration.	82
P2.14	Results of temperature-dependent d_0 measurements.	83
P2.15	Calculated Young's modulus and Poisson ratio based on the single crystal constants determined by Wang et al.	84
P2.16	Strain progression with measuring position at the left edge of the sample.	86
P2.17	Layer-wise median stress difference at left edge of sample	86
P2.18	Schematic of part-scale stress response to tensile stresses in top layer.	87
P2.19	<i>Ex situ</i> stress distribution mapping	87
P2.20	Application of $\sin^2 \alpha$ approach to a single diffraction pattern.	91
P2.21	Progression of stress difference and associated error in a constant gauge volume corresponding to section P2.3.4 using both $\sin^2 \alpha$ and Hooke's approach.	91
P3.1	Schematic of the experiment.	97
P3.2	Scanning patterns used to fabricate samples.	97
P3.3	Temperature evaluation procedure.	98
P3.4	Phase transformation of titanium during LPBF observed in a time series of diffraction pattern excerpts.	100
P3.5	Peak shift during laser exposure for two scanning strategies.	101
P3.6	Median stress difference $\sigma_{TD} - \sigma_{BD}$ for a) left edge and b) center GV positions and different sets of process parameters.	102
P3.7	Absolute stress estimation for a single subsurface layer while the laser passes over the GV.	103

List of Tables

2.1	Examples of laser applications in manufacturing processes	10
4.1	Nominal chemical compositions of used feedstock materials as provided by manufacturers	33

4.2	Process parameters used in the experiments	34
4.3	Scan vector length, count and orientation for used scanning patterns.	35
P1.1	Particle size distribution of Inconel 625 powder per sieve analysis.	52
P1.2	Parameter sets for the experiments.	52
P2.1	Sample parameters. a) Laser parameter sets b) Scanning patterns c) Process parameters that were kept constant for all samples.	71
P2.2	Numerical values of elastic constants used for calculation of stresses in figure P2.9.	84
P3.1	Process parameters.	104

List of Symbols

Symbols		
Symbol	Unit	Description
d_{hkl}	nm	Lattice spacing for reflection hkl
h	μm	Hatch distance
I	W cm^{-2}	Intensity of laser radiation
n	[]	Refractive index
P_L	W	Laser power
T	K, °C	Temperature
v_L	mm s^{-1}	Laser scanning speed
z_{GV}	μm	Distance between top layer and gauge volume
Greek symbols		
α	[]	Absorption coefficient
α	K^{-1}	Coefficient of thermal expansion (CTE)
α		Hexagonally closed-packed phase of titanium
α'		Martensitic phase of titanium
β		Face-centered cubic phase of titanium
γ	°	Sector opening angle for sector integration
ε	%, []	Lattice strain
ζ_{GV}	μm	Distance between substrate and gauge volume
η	°	Sector azimuth angle for sector integration
θ	°	Bragg angle
λ	nm, Å	Wavelength of electromagnetic radiation
ν	[]	Poisson's ratio
ρ	g cm^{-3}	Density
σ	MPa, N mm^{-2}	Mechanical stress
ϕ	°	Azimuthal angle
ψ	°	Measuring direction

List of Abbreviations

Abbreviation	Explanation
AM	Additive manufacturing
bcc	Body-centered cubic
BD	Building direction
CTE	Coefficient of thermal expansion
DESY	Deutsches Elektronen-Synchrotron
DFG	Deutsche Forschungsgemeinschaft
DIC	Digital image correlation
DMLS	Direct metal laser sintering
DRX	Dynamic Recrystallization
EDX	Energy-dispersive X-ray spectroscopy
EH1/EH3	Experimental hutch 1/3
EPBF	Electron beam powder bed fusion
ESRF	European Synchrotron Radiation Facility
fcc	Face-centered cubic
FEM	Finite element method
FIB	Focused ion beam
FWHM	Full width at half maximum
GV	Gauge volume
HAADF	High-angular annular dark field imaging
HAZ	Heat-affected zone
hcp	Hexagonal closed-packed
HEMS	High Energy Materials Science
IPK	Fraunhofer-Institut für Produktionsanlagen und Konstruktionstechnik
IWF	Institut für Werkzeugmaschinen und Fabrikbetrieb
L-scan	Longitudinal scanning pattern
LD	Longitudinal direction
LPBF	Laser powder bed fusion
MAM	Metal additive manufacturing
MM1/MM2	Measuring mode 1/2
MRD	Multiples of a random distribution

Abbreviation	Explanation
ODF	Orientation distribution function
PETRA III	Positron-Elektron-Tandem-Ring-Anlage, third generation
RS	Residual stress
SAXS	Small-angle X-ray scattering
SEM	Scanning electron microscopy
SLM	Selective laser melting
STEM	Scanning transmission microscopy
T-scan	Transverse scanning pattern
TD	Transverse direction
TEM	Transmission electron microscopy
TFT	Thin-film transistor
TGM	Thermal gradient mechanism
TI-scan	Transverse island scanning pattern
WAXS	Wide-angle X-ray scattering
WDX	Wavelength-dispersive X-ray spectroscopy
WEDM	Wire electrical discharge machining
XEC	X-ray elastic constant
ZELMI	Zentraleinrichtung Elektronenmikroskopie

Part I

Background

Light and illumination are the primary requirements for observation, which is the foundation of the scientific method. Since the wavelength and intensity of electromagnetic radiation, as a more technical term for light, determine what can be observed and measured, scientists undertook immense efforts to improve the quality of light sources for scientific purposes. One of the light sources with the highest intensities is the synchrotron, a large-scale circular facility, often spanning hundreds of meters, where electrons are kept at close to the speed of light in a vacuum tube. Forcing the electrons on a circular trajectory via strong magnets produces highly intense electromagnetic radiation that can be fine-tuned to the desired wavelength. This beam can be directed onto a sample, interacting with the irradiated matter.

The third generation of synchrotron light sources has jumpstarted the possibilities of observing complex processes in real-time. Due to the nature and properties of synchrotron radiation, time-resolved changes inside the material under investigation can be observed. The range of possibilities and scale for these process investigations is tremendous, extending from the deposition of atomic layers [Klu15] to material behavior under extreme conditions in high-pressure experiments [Che04]. Synchrotron radiation research is carried out in many fields, covering physics to biology to engineering.

For engineers, the possibility of replicating actual manufacturing conditions and investigating material behavior *in situ*¹, during the processing, offers enormous potential for both fundamental process understanding and process optimization. One class of manufacturing processes has gained exponentially increasing attention by industry and research: 3D printing or additive manufacturing (AM) has become ubiquitous in recent years to the extent that some liken it to a new industrial revolution [DAv18].

This thesis combines synchrotron radiation and AM to investigate the underlying mechanisms and phenomena in a metal part irradiated by a focused laser spot. The primary goals are to reveal the mechanisms of stress formation and evolution, phase transformations, and microstructure development. High-energy X-ray diffraction experiments are the core experimental method utilized to reach these goals. X-ray diffraction is based on interference phenomena involving electromagnetic radiation and crystalline materials, where the radiation wavelength and interatomic spacing are the same order of magnitude. Diffraction experiments can simultaneously reveal the texture, phase composition, and stress state of the material without interfering with either, which is unattainable using other measurement methods and highly desired for numerous applications, especially for *in situ* experiments.

¹According to Korsunsky, the term *in situ* is incorrect and should be replaced by *operando* [Kor20]. However, *in situ* is well established, widely used in the literature, and will be used throughout this thesis for that reason.

The stress state of a component is of particular interest due to its impact on mechanical properties, fatigue behavior, and susceptibility to crack formation. Even if no external load is applied, internal stresses may be present in the part. If the part is in mechanical and thermal equilibrium, these internal stresses are named *residual stresses*. Knowing the stress state and then altering it is crucial for successful service conditions. Furthermore, diffraction reveals the crystallographic orientations of the grains and shows if the material is textured or not, which is of particular importance to the anisotropy of the material's properties. Similarly to the stress state, the ability to fine-tune the anisotropy to the desired use case would be greatly appreciated.

Understanding and manipulating these properties in the context of AM is of great interest as the technology is still in its infancy compared to other conventional manufacturing methods. While one can debate the possibility of AM starting a new industrial revolution, its impact on engineering in the last 30 years is undoubtedly significant. During this time, numerous AM techniques have been developed with powder-bed-based processes representing one major category.

For structural applications, metals are the most important class of materials, and powder-bed processes are especially suited to manufacture metal parts additively. As the name suggests, a metal powder bed is fused selectively by a focused heat source, i. e., a laser (laser powder bed fusion - LPBF) or electron (electron beam powder bed fusion - EPBF) beam, to generate a single layer with the desired geometry. After applying a new thin powder layer on top, the process is repeated. The part is manufactured layer by layer to generate a three-dimensional shape.

This manufacturing approach has several key advantages. First of all, material usage: Since only the material needed for the part is fused together² AM is much more resource-efficient from a raw material perspective than conventional shaping processes, which generally work subtractively from a larger shape to reach the final dimensions. Secondly, AM enables the manufacturing of geometries that are not feasible using conventional methods. Therefore, three primary applications for AM in general and metal AM in particular are of vital interest:

- Topology optimization: Without any added cost, light-weight, material-efficient parts can be designed, where areas that are not load-bearing and, therefore, unneeded are not fused. Unlike conventional processes, these geometries can be manufactured in a single-step process and do not require time-consuming, expensive material removal.
- Mass customization: While mass production is not a strong point for AM, mass customization is. This term describes adjusting a part's geometry or properties to the customers' needs on a massive scale. One prime example where this is essential is medical technology and prosthetics. Custom prosthetics tailored to the patient's anatomy significantly improve the life span of the implant and ease the patient's burden.
- Unique geometries: Parts exposed to highly challenging thermal conditions such as turbine blades benefit from internal cooling channels to reduce the thermal load on the parts.

²Disregarding support structures, which may be necessary in some cases.

Due to the layer-by-layer nature of AM processes, these internal cooling channels can be easily integrated into the part from the start. Since turbine blades have a complex, curved shape, conventional manufacturing processes cannot replicate this or only do so at high added cost.

Focusing on laser powder bed fusion (LPBF), the process still suffers from reproducibility, reliability, and accuracy problems despite all of its advantages. At the core of most of these issues is the focused energy input by the laser beam. This laser spot melts the powder layer and the surface of the solidified material below. High thermal gradients are induced, causing a range of reactions from elastic to plastic deformation, phase transformations, diffusion processes, et cetera. In combination with the rapid movement of the laser spot across the powder layer, a characteristic stress state and microstructure are developed during LPBF. *In situ* experiments can shed light on these processes as they occur.

For the evaluation of stresses and microstructure, diffraction experiments are especially suited. A single diffraction pattern contains a magnitude of data on the irradiated gauge volume, including grain sizes, orientations, texture, defects, phase composition, temperature, and the stress state. With its unmatched combination of photon flux, coherence, and high energy, synchrotron radiation is the perfect tool for these types of experiments. This thesis reveals some of the underlying phenomena of the stress and microstructure formation and evolution in the LPBF process using *in situ* high-energy synchrotron radiation diffraction experiments.

Structure of this thesis

The present work constitutes a cumulative dissertation. Three peer-reviewed articles have arisen from work performed within this thesis:

- P1 F. Schmeiser, E. Krohmer, C. Wagner, N. Schell, E. Uhlmann, and W. Reimers. “In situ microstructure analysis of Inconel 625 during laser powder bed fusion”. *Journal of Materials Science* **57** (2022), pp. 9663–9677. DOI: 10.1007/s10853-021-06577-8
Version information: the manuscript has been edited and published in the journal.
The PDF version of the article can be found in chapter P1 of the dissertation.
- P2 F. Schmeiser, E. Krohmer, N. Schell, E. Uhlmann, and W. Reimers. “Experimental observation of stress formation during selective laser melting using in situ X-ray diffraction”. *Additive Manufacturing* **32** (2020), p. 101028. DOI: 10.1016/j.addma.2019.101028
Version information: the manuscript has been edited and published in the journal.
The PDF version of the article can be found in chapter P2 of the dissertation.
- P3 F. Schmeiser, E. Krohmer, N. Schell, E. Uhlmann, and W. Reimers. “Internal Stress Evolution and Subsurface Phase Transformation in Titanium Parts Manufactured by Laser Powder Bed Fusion—An In Situ X-Ray Diffraction Study”. *Advanced Engineering Materials* **23** (2021), p. 2001502. DOI: 10.1002/adem.202001502

1 Introduction

Version information: the manuscript has been edited and published in the journal.
The PDF version of the article can be found in chapter P3 of the dissertation.

These three articles serve as the main part of this thesis. They are preceded by a literature review, a summary of this thesis's objectives and a detailed description of the experimental methods. The findings will be summarized and related to the specified goals following the articles. Finally, an outlook on possible future investigations will be given.

The three publications have individual bibliographies complying with the respective journal's standards. There is an additional bibliography at the end of this document which contains the references cited in the remaining thesis.

Literature review 2

In this section, the current state of the literature in both laser powder bed fusion and synchrotron radiation technology is reported. While each article presented in part II of this thesis features an individual introductory section tailored to their respective contents, this chapter covers a broader spectrum and serves as a general overview of the mentioned topics.

2.1 Additive manufacturing of metals

Since the company EOS released their Direct Metal Laser Sintering (DMLS) system in 1994, numerous other metal additive manufacturing (MAM) processes and systems have been developed and are sold worldwide [Woh20]. While 3D printing at home using polymer filaments has become more affordable and approachable, additively manufacturing metallic materials has remained exclusive to industrial and academic users due to the associated costs of such machines, safety considerations, and necessary periphery. Despite almost 30 years of research and development, industrial applications of MAM are still sparse compared to conventional methods. The limited industrial adoption of MAM is essentially caused by a lack of fundamental process knowledge. Though it is possible to create dense, fault-free parts, certain areas such as the formation of residual stresses are still not fully understood. From the range of available MAM processes, this thesis deals with the laser powder bed fusion (LPBF) process and its advantages and drawbacks, which will consequently be the focus of this section.

2.1.1 Distinction to conventional manufacturing methods

The choice of the appropriate manufacturing process depends on several factors. For specific applications, metal additive manufacturing offers unseen possibilities and advantages. The geometric freedom of design is one of the main opportunities presented through MAM. It is possible to manufacture parts with geometries that cannot - or only with high added cost - be fabricated using conventional processes. For example, internal cooling channels to increase working temperatures and life spans of turbine blades are of great interest. Furthermore, biomimicry and bioinspired design can be used for topological optimizations for weight-saving and increased aesthetic appeal [DuP19]. However, there is still untapped potential and ground to cover by designers, engineers, and researchers here, and design rules must be established.

In addition to design possibilities, the capabilities of MAM for cost and resource-effective rapid prototyping are unmatched. Adjustments can be implemented quickly without creating new casting molds or machining programs, which often has to be done by hand in the early prototyping stages using conventional manufacturing methods. Similarly, parameter studies can be conducted fast and efficiently to determine the optimal manufacturing conditions. Since only the material needed for the part is molten or deposited in MAM, and unused powder can be recycled (with a small caveat discussed in section 2.1.2), there is no added cost due to material waste as it occurs in machining. Ideally, MAM processes involve only two steps: manufacturing the part itself and removal from the substrate or baseplate. Conventional manufacturing can involve numerous process steps from several of the main groups mentioned above. Parts often have to be machined to ensure geometrical accuracy and low tolerances, while an optimized MAM process delivers a near-net-shape geometry directly.

Another unique advantage of MAM is the possibility to manipulate the material's properties *in situ*, directly during the manufacturing process. As explained in more detail in the next section, targeted adjustment of the processing parameters facilitates an *in situ* heat treatment. Furthermore, MAM processes are suited for innovative material development and alloy design techniques using several feedstock materials, such as *in situ* alloying or multi-material applications.

Despite all of the mentioned advantages, additive manufacturing might not suit every application. First of all, currently, MAM parts generally require post-process heat treatments to obtain the desired mechanical and microstructural properties. Furthermore, surface qualities do not yet match those of machined or polished parts, so applications that require a flawless surface finish will need a further processing step in the end. However, the necessity of post-processing might be alleviated by further technological improvements.

While geometric design freedom is one of MAM's main advantages, the overall size of the parts is constrained by the process environment. In powder bed-based processes, the size of the building chamber and its exposable area are the limitations, while powder feed processes such as directed energy deposition depend mainly on the range of motion of the nozzle. The building rate becomes a limiting factor for large-scale parts as process times increase linearly with part size. Consequently, using MAM for mass production is rarely appropriate yet. Specific part geometries might be suited, especially if many parts can be fitted onto a single substrate and, therefore, into a single manufacturing process. However, in general, and indeed for larger parts, conventional manufacturing processes are superior in mass production, which is further amplified by the consistency issues with MAM processes mentioned before. Another possible application for MAM is hybrid manufacturing, where conventionally manufactured parts are upgraded, finished, or joined using additive manufacturing technologies.

The unique strengths of metal additive manufacturing qualify it for specific applications, but, in the author's opinion, MAM will not replace conventional manufacturing methods by any stretch. It is, however, another tool that extends the current possibilities and allows for the exploration of new designs, properties, and materials.

2.1.2 The laser powder bed fusion process

As the name suggests, laser powder bed fusion (LPBF) is a powder bed-based manufacturing process. A thin powder layer is applied upon a substrate, which can but does not have to be the same material as the powder feedstock. The powder layer thickness can be adjusted and depends on other process parameters, but commonly used are thicknesses between 30 μm to 50 μm . A focused laser beam is then deflected onto the metal powder to expose the desired cross-section. Afterward, the building platform is lowered, a new powder layer is applied, and the laser exposure is repeated with the alterations necessary to produce the final geometry of the part. After the building process is completed, the excess powder is removed. One current research topic is the possibility of recycling this used powder, which is hindered by possible oxidization processes and contaminations [Raz21; San20].

During the process, the build chamber is kept under a circulating inert gas atmosphere which is constantly filtered. The inert gas, e. g. argon or nitrogen prevents oxidization and the ignition of molten metal and is therefore necessary from both a part quality and a safety point of view.

After the production process is completed, the part is still connected to the substrate plate and has to be removed as one of the post-processing steps associated with LPBF. Other possible treatments include further mechanical post-processing such as surface improvements [Mal21], support removal [Cec19], and hot-isostatic pressing [Kun20] as well as heat treatments to relieve residual stresses [Wan19] and manipulate the microstructure [Mar18].

The LPBF process is characterized by over 130 parameters which may influence the final part [Reh05]. The choice of laser power P_L and scanning speed v_L is one of the most influential aspects of the resulting part quality. The laser power and speed are chosen so that the exposed metal powder is molten and adheres to the substrate below. If the laser power is too low, a phenomenon called *balling* can occur [Yap15]. Balling leads to bead-like structures and may cause the production process to fail by blocking the recoating mechanism. On the other hand, if the laser power is too high, *keyholing* may occur [Gon14]. In this case, the melt pool has a high penetration depth, causing remelting of the material below, which can lead to undesirable porosity [Kin14].

2.1.3 Overview of laser-matter interaction

Several complex interaction phenomena occur when a focused laser beam is directed onto a metal surface. These phenomena are utilized for a range of laser processing applications from all of the manufacturing groups defined in the German standard DIN 8580, see table 2.1. For LPBF, which is classified as group 1, primary shaping, the interaction with the powder surface and the underlying metal is of particular relevance. The phenomena are classified into optical interaction, thermal interaction, and energy coupling.

When considering a perpendicular laser beam incidence on a material's surface, the relationship in equation 2.1 can be assumed.

Table 2.1: Examples of laser applications in manufacturing processes

Process Group	Example of laser application
1 Primary shaping	Laser powder bed fusion, Directed energy deposition
2 Forming	Laser sheet bending
3 Cutting	Laser cutting
4 Joining	Laser welding
5 Coating	Laser cladding
6 Changing material property	Laser-shock peening, Laser hardening

$$P_0 = P_R + P_T + P_A \quad (2.1)$$

The total incident laser power is divided into the reflected part P_R , the transmitted part P_T , and the absorbed part P_A with their respective fractions dependent on the radiation's and material's properties. Reflection can occur in a directed or a diffuse manner. A metal powder bed, for example, will generally lead to a diffuse reflection into the process chamber. The reflected radiation is somewhat wasted energy in LPBF. Transmission does not play a role in the case of metals and commonly used laser sources. Absorption, however, is the mechanism that delivers energy into the irradiated material. The degrees of reflection, transmission, and absorption depend on the wavelength, polarisation, and incidence angle of the radiation and the optical properties of the material, such as the absorption coefficient α and the refractive index n . Furthermore, the amount of absorption is determined by the incident intensity and the geometry as well the chemical composition of the exposed surface. For optimal processing conditions, the absorbed fraction of the laser power should be maximized.

The absorbed energy leads to a thermal interaction in the material. In LPBF, several material responses are possible depending on the radiation intensity [Bli13]:

Heating	$I \sim 10^3 \text{ W cm}^{-2}$,
Melting	$I \sim 10^5 \text{ W cm}^{-2}$,
Vaporization	$I > 10^6 \text{ W cm}^{-2}$,
Ionization	$I \sim 10^8 \text{ W cm}^{-2}$,
Sublimation	$I > 10^9 \text{ W cm}^{-2}$

where a controlled melting regime is certainly the goal. As seen in the list, insufficient energy input does not melt the exposed material, while an excessive radiation intensity leads to undesired effects such as vaporization and plasma formation. These effects interfere with the chemical composition and the process stability. When the metal powder absorbs energy, it is heated and melted given the appropriate radiation intensity. Inside the melt pool, convection phenomena such as Marangoni flow occur [Cla20]. Around the melt pool, a heat-affected zone is formed and heat is transferred into the surrounding material via conduction. Previously solidified material is, therefore, affected numerous times as subsequent layers are exposed, thereby experiencing a sort of *in situ* heat treatment.

2.1.4 Materials for LPBF

LPBF can be applied to a wide range of materials, each presenting its own set of opportunities and challenges [Yad21]. For example, the laser absorption characteristics differ immensely between different materials, which necessitates the use of lasers emitting at a particular wavelength for specific materials. Current research is, for example, focused on using green lasers for copper and its alloys [Nor22] while an infrared laser with a wavelength of 1070 nm was used in this study. Furthermore, the rheological properties of the feedstock vary. The feedstock powder material's particle distribution has to be adjusted regarding the material. Otherwise, flowability problems can occur. Nonetheless, LPBF carries the potential for innovative materials development techniques using multiple feedstock powders, such as multi-material applications [Wal21] and *in situ* alloying [Mos21]. Additionally, the development of AM-specific alloys is one of the most promising and vital areas of research to use the potential of AM fully.

Despite these possibilities, commercially available alloys initially developed for other purposes are generally used for LPBF to date. Several alloy systems are being thoroughly researched regarding their LPBF processability and resulting properties, ranging from aluminum alloys [Abo19], steels [Hag21], high entropy alloys [Ost21] to nickel alloys [Zha18] and titanium alloys [Zha21].

Nickel-base alloys are especially suited for demanding high-temperature and high-pressure service conditions due to their corrosion resistance, temperature-stable mechanical properties, and creep resistance. One alloy that is being extensively researched is Inconel 625, which is a solution strengthened nickel-base alloy with additions of chromium, molybdenum, niobium, iron, manganese, and silicon [Kar21; Tia20b]. Due to its properties, the main applications for Inconel 625 are turbine blades in aerospace technology. As mentioned in the introduction, one of the most promising applications of LPBF is the possibility of integrating cooling channels in curved structures such as turbine blades in a single manufacturing step, which illustrates the broad interest in Inconel 625 for LPBF. However, Inconel 625 is prone to segregation of molybdenum and niobium, and Inconel 625 parts manufactured by LPBF generally have high residual stresses [Kar21]. These two effects can be detrimental to a component's performance and require further research, so Inconel 625 was chosen as one of the materials to study in this thesis.

Titanium and its alloys are another class of metals of particular interest to the LPBF community, partly caused by their limited machineability. Additionally, its high specific strength, low density, and biocompatibility make titanium especially suited for biomedical applications. In combination with the geometric freedom LPBF offers, the prospect of customized prosthetics tailored to the patient's anatomy is one of the essential advantages of using LPBF. Titanium experiences a phase transformation at elevated temperatures, section 2.1.5.2, which can be triggered multiple times during LPBF processing. This phase transformation impacts the microstructure, as the two phases are connected by a crystallographic orientation relationship, which can be manipulated by targeted alloying [Bar18]. In the present thesis, commercially-

pure titanium will be investigated to illuminate the phase transformation *in situ* and discuss the impact of the repeated laser scanning inherent to LPBF.

2.1.5 Microstructure development in LPBF

The focused energy input and localized melting and solidification processes result in microstructural features exclusive to LPBF-fabricated parts. Microstructure development is a continuous process that extends further than the initial solidification of the molten powder due to the repeated heating and cooling cycles during the laser exposure of subsequent layers.

The initial formation of the microstructure depends on the melt pool created during laser exposure. Depending on the process parameters, the melt pool shape varies, impacting how heat is dissipated into the surrounding material. As noted by DebRoy et al., the melt pool shape „can be oval or tear-dropped on the top surface, and semicircular or keyhole in cross-section depending on the heat source intensity and scanning speed“ [Deb18].

The shape is generally classified as *conduction mode* or *keyhole mode*. In keyhole mode, the melt pool's penetration depth reaches several layers below the powder, creating a deep cavity. This high penetration depth is generally appropriate for welding since it improves the process's energy efficiency as the laser beam is reflected numerous times inside the cavity [Rai07]. However, keyhole mode can be disadvantageous in LPBF since it can induce unwanted porosity in the final part [Kin14].

Therefore, conduction mode is commonly preferred in LPBF. Conduction mode occurs below a certain energy input threshold, producing a semicircular melt pool shape. Also, the vaporization of metals, which can lead to problems with keyhole mode, is considered negligible in conduction mode [Pat20].

A typical LPBF microstructure, based on conduction mode melting, is characterized by columnar grain growth oriented in building direction. However, columnar growth can be averted by adjusting the processing parameters as reported by Dehoff et al., who were able to tailor the grain orientation in a localized way in electron beam additive manufacturing [Deh15]. In addition to the grain orientation, there are significant variations in the grain size distribution depending on several factors, such as the feedstock powder material and the processing parameters. The possible grain sizes range from submicron diameters [Zaf21] to single-crystal final parts [Pis21].

In addition to the columnar grain structure, LPBF samples show intragranular, cellular substructures, which do not correspond to a crystal orientation variation and have a size of about 0.5 μm . At these subgrain boundaries, chemical segregation and a high dislocation density were found, first reported by Saeidi et al. for austenitic steels [Sae15]. According to Bertsch et al., the dislocations are the result of plastic deformation caused by thermal stresses due to mechanical constraints [Ber20]. The tangled dislocation network induces a hardening effect, as confirmed by Voisin et al. [Voi21]. Cellular substructures were reported for numerous materials, including

Inconel 625, where reduced dislocation density and dissolution of the cellular structure were achieved after prolonged annealing [Gol20].

2.1.5.1 Grain growth mechanisms and texture

During solidification of molten material, seed crystals are formed at the solidification front, which subsequently grow. Crystallites with different orientations compete during this stage, with several studies reporting that crystallites with an orientation perpendicular to the melt pool apex dominate [DiW16; Sun18; Wan20; Wei16; Yin18]. This preferred direction of growth is caused by the thermal gradient being the largest in this direction [DiW16]. The preferred crystallographic orientation depends on the crystal structure of the material, e.g. face-centered cubic (fcc) materials such as Inconel 625 exhibit a preferred $\langle 100 \rangle$ direction [Was62].

Pham et al. studied the grain growth in cubic alloys in relation to the local thermal gradient and the isotherm velocity. They report that the grain growth is often restricted to the center of the melt pools and identified the misalignment of the thermal gradient and existing grain orientations as the cause for side-branching. Additionally, their study showed that a chessboard scanning strategy with a scan vector rotation of 67° between layers disrupts the usual columnar grain growth. [Pha20]

As mentioned above, the melt pool shape impacts the grain growth and the resulting crystallographic texture. Grains grow inwards from the outside of the melt pool with the growth direction perpendicular to the melt pool boundary. Therefore, deep keyhole melt pools show substantial variations of the melt pool front normal, resulting in a weakly textured material. On the contrary, shallower melt pools associated with conduction mode result in more parallel grain growth and a stronger preferred crystallographic orientation. LPBF parts generally show epitaxial grain growth, which further enhances the crystallographic texture [Bas16].

In addition to the initial solidification after laser exposure, adjacent melt tracks and rescanning influence grain growth. In chapter P1, texture and related phenomena are discussed in-depth.

2.1.5.2 Phase transformations

Certain materials undergo a solid-state phase transformation corresponding to a crystal structure change when passing a particular temperature. In case of commercially-pure titanium grade 1 for example, the low-temperature, hexagonally close-packed (hcp) α phase transforms into a body-centered cubic (bcc) β phase at a temperature of 882°C [Zwi74]. The two phases are connected via the Burgers orientation relationship. In LPBF, the phase transformation initially occurs after the primary solidification of the molten powder. The material crystallizes in the high-temperature phase and then transforms during the rapid cooldown. However, repeated thermal cycling is one of the unique features of LPBF. Even the solidified material gets reheated to high temperatures and possibly undergoes the phase transformation several times, especially

during the first few subsequent molten layers. These repeated phase transformations impact the microstructure and resulting properties of the finished part.

The phase transformation can occur in different ways. If the cooling rate is sufficiently high, the transformation will happen in a diffusion-less shearing mode, which is called a martensitic transformation. Often, LPBF-processed materials that undergo a temperature-related phase transformation show martensitic phase fractions in their microstructure, which has been reported for steels [Tia20a] as well as titanium alloys [Hua20].

For commercially-pure titanium grade 1, the cooling rate threshold is 10^3 K s^{-1} and the martensitic start temperature is 850°C [Lüt07]. If the cooling rate is below 10^3 K s^{-1} , the microstructure solely consists of the α phase. Above that threshold, the martensitic α' phase occurs, which was shown by Oh et al. [Oh04]. In LPBF, cooling rates up to 10^8 K s^{-1} occur, depending on the processing parameters [Att17; Sci17]. Still, the microstructure of LPBF-processed commercially-pure titanium grade 1 generally consists of a mixture of the α and α' phase. Due to the repeated thermal cycling in LPBF, repeated phase transformations can occur as well as recrystallization, which influence the microstructure and phase composition. It has to be noted that for commercially-pure titanium grade 1, the difference between α and α' grains is morphological, and their crystal structure is equal.

To fully understand the phase transformation phenomena in LPBF, *in situ* experiments have to be carried out. Zhao et al. were the first to experimentally observe the martensitic phase transformation in Ti-6Al-4V *in situ* under LPBF conditions [Zha17]. Hocine et al. also performed *in situ* X-ray diffraction experiments using a custom LPBF machine. They found a relation between the scan vector length and the β phase duration. Shorter scan vectors lead to slower cooling and longer retention of the β phase. The longer retention leads to larger primary β grains and influences the subsequent α' formation in its texture and morphology [Hoc20b]. Calta et al. investigated both Ti-6Al-4V and Ti-5553 by *in situ* X-ray diffraction and found a linear correlation between the laser power and the β lifetime. Additionally, they reported peak broadening for both the α and β phases, which they relate to an increase in dislocation density and chemical segregation processes [Cal20].

All the *in situ* studies mentioned above focus on the initial phase transformation after the primary melting and solidification. However, the effect of repeated thermal cycling during the following layers is evaluated in chapter P3 of this thesis.

2.1.6 Residual stresses in LPBF

If sufficiently high, residual stresses can severely impact the final part quality and even disrupt the manufacturing process itself. For example, certain alloys are prone to cracking caused by residual stress build-up in the parts as they are produced. In the worst case, the build-up of residual stresses causes delamination during or after laser exposure, disrupting the building process and even damaging the machine. Residual stresses can also cause unwanted deformation after removing the part from the baseplate, reducing the geometrical accuracy. Furthermore,

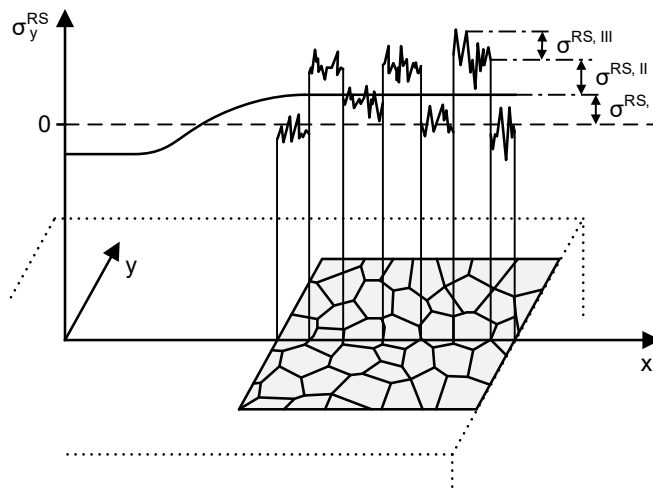


Figure 2.1: Classification of residual stresses by reach. Graphic adapted from [Eig95].

residual stresses impact the part's mechanical properties, for better or worse, which can impair the fatigue life of parts in service conditions.

The following sections give a general introduction to residual stresses and their measurement. Subsequently, phenomenological considerations regarding their formation and evolution during and after the LPBF process are reported. As mentioned above, many process parameters influence the final part quality, so an overview of various process parameters and their influence on the residual stresses is given.

2.1.6.1 Definition and classification of residual stresses

Residual stresses are defined as elastic stresses present in a material without any external load [Mac73]. They are caused by inhomogeneous elastic or elastoplastic deformations. Residual stresses are generally classified by their reach and their impact [Eig95], figure 2.1. In this thesis, the terminology of Macherauch et al. will be used [Mac73].

- **Type I** residual stresses span over a large number of grains. They are sufficiently constant over an extensive volume. Any interference with their equilibrium will result in a macroscopic deformation.
- **Type II** residual stresses span over a single grain or a small number of grains. Interference with their mechanical equilibrium may result in a macroscopic deformation.
- **Type III** residual stresses extend over distances of a few interatomic spacings and are caused by lattice defects such as dislocations. Interference with their mechanical equilibrium does not cause a macroscopic deformation.

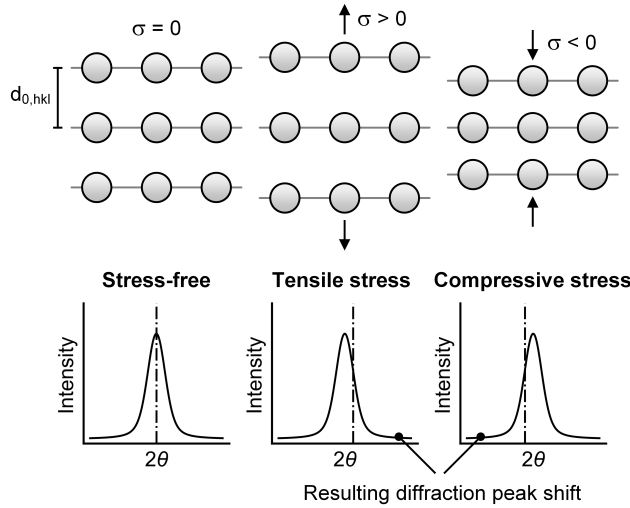


Figure 2.2: Schematic of crystal lattice response to stress and resulting diffraction peak shift.

2.1.6.2 Determination of residual stresses using X-ray diffraction

In X-ray diffraction, the interaction of metals with X-rays is utilized. When electromagnetic radiation hits a periodic structure with a periodicity in the same order of magnitude as the radiation wavelength, interference phenomena can occur. Crystalline materials, such as metals, are characterized by their periodic lattice structure, with interatomic spacings similar to X-ray wavelengths. Arbitrary planes can be placed in these lattices, characterized by their Miller indices hkl , which denote the fraction of the three primary axes of the crystal structure [Shm06]. Every lattice plane has a characteristic interplanar spacing, denoted by d_{hkl} , which is influenced by the stress state of the material, see figure 2.2.

Residual stresses cannot be measured directly via X-ray diffraction. Instead, the lattice plane displacement is determined. The lattice plane's diffraction angle is measured and related to the lattice spacing via Bragg's equation equation 2.2.

$$n\lambda = 2d \sin \theta \quad (2.2)$$

If the stress-free lattice spacing d_0 is known, the lattice strain can be calculated following equation 2.3. Determining the stress-free lattice spacing can be challenging on its own, though, and a wrong d_0 can have a drastic impact on the accuracy of the calculated stress values, see section 4.2.

$$\varepsilon = \frac{d_{\text{measured}} - d_0}{d_0} \quad (2.3)$$

The lattice strain is related to the stress by Hooke's law, equation 2.4.

$$\varepsilon_{ij} = \frac{\nu + 1}{E} \sigma_{ij} - \delta_{ij} \frac{\nu}{E} \sigma_{kk} \quad \text{with} \quad \delta_{ij} = \begin{cases} 1, & \text{if } i = j, \\ 0, & \text{if } i \neq j. \end{cases} \quad (2.4)$$

Voigt's notation can be used for the elastic constants, equation 2.5.

$$\frac{1}{2} s_2 = \frac{\nu + 1}{E} \quad \text{and} \quad s_1 = -\frac{\nu}{E}, \quad (2.5)$$

Considering the geometrical transformation between a sample coordinate system and a laboratory coordinate system, Voigt's notation, and the stress tensor equation (omitted here for the sake of brevity), the lattice strain in a macroscopically isotropic, polycrystalline material is related to the stress following equation 2.6. This equation is often called the fundamental equation of residual stress analysis. Its deduction has been well reported, e. g. in [Eig95; Hau97; Noy87; Rei08; Spi19].

$$\begin{aligned} \varepsilon_{\varphi, \psi} = & \frac{1}{2} s_2 (hkl) \left[\sigma_{11} \cos^2 \varphi \sin^2 \psi + \sigma_{22} \sin^2 \varphi \sin^2 \psi + \sigma_{33} \cos^2 \psi \right. \\ & \left. + \sigma_{12} \sin 2\varphi \sin^2 \psi + \sigma_{13} \cos \varphi \sin 2\psi + \sigma_{23} \sin \varphi \sin 2\psi \right] \\ & + s_1 (hkl) [\sigma_{11} + \sigma_{22} + \sigma_{33}] \end{aligned} \quad (2.6)$$

2.1.6.3 Residual stress analysis in LPBF applications

Besides diffraction methods using different types of radiation, mechanical methods and modeling are widely used to determine residual stresses.

Recently Schröder et al. published a review paper concerning diffraction-based residual stress measurements for LPBF [Sch21]. Laboratory X-ray diffraction, synchrotron radiation diffraction, and neutron diffraction are standard diffraction methods for residual stress determination. The main advantages of neutrons are their high penetration depth and the possibility of evaluating specific gauge volumes due to secondary apertures and an arbitrary diffraction angle. While the entire sample thickness is irradiated in synchrotron diffraction experiments in transmission mode, in neutron diffraction, the detector is generally placed in a 90° angle to the primary beam. By adjusting the primary and secondary apertures, the geometry of the gauge volume can be chosen. By translating the specimen, the location of the gauge volume can be adjusted as well, thereby allowing the opportunity to investigate arbitrary locations and volumes of the sample.

Disadvantages of neutrons are the scarcity of neutron sources and the long acquisition times during measurements due to the comparatively low flux. Performing *in situ* measurements with neutrons during the LPBF process is not possible at the moment. Furthermore, beamtime

efficiency and throughput are drastically reduced compared to synchrotron radiation diffraction experiments. Nevertheless, several insightful *ex situ* studies of LPBF parts have been published [Goe20; Ser21; Wan17].

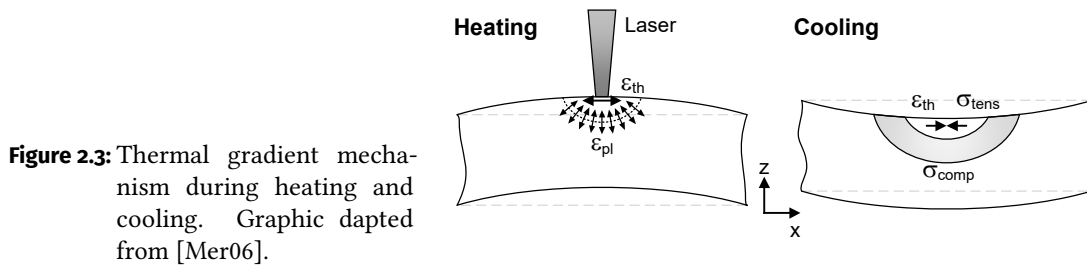
Synchrotron radiation diffraction can be performed using monochromatic or polychromatic radiation. Aminforoughi et al. developed a robust method for residual stress determination in LPBF parts using monochromatic radiation in transmission mode, which is an adaptation of the conventional $\sin^2 \psi$ method commonly used in laboratory X-ray experiments [Ami21]. Their approach will be discussed in detail in section P2.9.

Due to the short acquisition times thanks to the high photon flux, many measurement points can be obtained in a short time. A two-dimensional distribution mapping of the lattice spacings, strains, and stresses can be acquired quickly by arranging the measurement points in a close-meshed grid. These mappings illustrate the distribution of strains and stresses in the sample to reveal general trends and distribution phenomena as presented by Phan et al. [Pha20].

Another possibility to obtain such two-dimensional stress distributions is the so-called contour method. Contrary to the methods mentioned above, this is a destructive testing method intervening with the mechanical equilibrium of the specimen. Here, a combination of numerical modeling and mechanical cutting is used. The specimen is carefully cut, and the resulting displacement on the cutting surface is measured. The displacement data serves as a boundary condition for a finite element model of the specimen. This model is then used to calculate the residual stress distribution of the stresses normal to the cutting plane. [Pri13]

The contour method has been established as a viable, nevertheless destructive, form of residual stress measurement in LPBF applications. Levkulich et al. investigated the impact of process parameters on the residual stress distribution [Lev19], while Phan et al. used a combination of measurement techniques to evaluate the residual stress distribution in bridge-shaped specimens [Pha19].

Other mechanical and, therefore, destructive residual stress measurement techniques include hole drilling and, on a microscopic scale, FIB-DIC. Both follow the same basic principle as the contour method: Interference with the mechanical equilibrium will lead to mechanical deformation in a stressed material. By measuring the displacement, the causative residual stresses can be calculated. The displacement can be measured directly using strain gauges or digitally using digital image correlation (DIC). Strain gauges are positioned around the planned location of the hole to drill. DIC is based on comparing digital images acquired concurrently to material removal. In FIB-DIC, which is short for *focused ion beam – digital image correlation*, the first part refers to the mode of cutting. Here, the sample is prepared in a special device, which is usually part of a scanning electron microscope (SEM) and equipped with an ion beam cannon, allowing exact material removal. The resulting displacement is derived from the deformation captured by concurrent SEM image acquisition and digital image correlation. Due to the microscopic scale of material removal, FIB-DIC allows the determination of residual stresses on an intergranular (type II) as well as intragranular (type III) level, see section 2.1.6.1 [Kor09], while hole drilling in general, depending on the size of the drill bit and the grain size of the



material, measures type I residual stresses. FIB-DIC has been used by Song et al. for additively manufactured components [Son20], while conventional hole-drilling has been reported quite extensively [Bar19a; Che20; Rob18].

2.1.6.4 Origin of residual stresses in LPBF

Since then, research has focused on empirical and numerical residual stress investigations. A comprehensive, mechanistic model of the evolution of residual stresses is still missing to date.

Mercelis and Kruth identified two mechanisms that cause residual stresses, schematically shown in figure 2.3. Adapted from sheet laser bending, the *thermal gradient mechanism* (TGM) generates residual stresses. The focused energy input by the laser induces large thermal gradients due to the rapid heating and comparatively slow heat conduction. In the heat-affected zone (HAZ), the material's strength significantly decreases while the material simultaneously expands. The thermal expansion is restricted since the heated material is bonded to the previously solidified material below, inducing compressive elastic strains. Due to the material's reduced strength, plastic deformation ensues. As the heated material cools down, it shrinks, now restricted by the material below. The hindered contraction induces tensile stresses in the top layer and compressive stresses beneath.

These mechanisms result in a characteristic distribution of residual stresses in LPBF parts. Several researchers reported similar general trends. Using finite element (FE) modelling [Den17; Din11; Wil18] and experiments [And18; Vra14] and a combination of both [Gan19], the top and bottom layers are commonly found to be in tension while the center of the part is in compression.

2.1.6.5 Process parameters and their influence on residual stresses

The magnitude and distribution of residual stresses depend on the heat input and the cooling conditions. This section discusses the influence of various process parameters on residual stresses. Unfortunately, most studies are somewhat limited in their transferability since identical parameter sets are rarely used, and each process parameter can influence the final product. For many parameters, contradicting findings are found in the literature. As one example, Mercelis

and Kruth found the highest stresses perpendicular to the scanning direction [Mer06]. On the other hand, Kruth et al. reported the opposite and found the lowest stresses perpendicular to the scanning direction [Kru12]. This discrepancy can be caused by several factors, ranging from the differing part geometries to the scanning strategies.

The so-called scanning pattern comprises the entirety of individual scan vectors. It is characterized by the scan vectors' length, spacing, orientation, and possible inter-layer changes. These parameters influence the thermal management and the resulting residual stress state.

Several studies found that a reduction of the scan vector length reduces the residual stress magnitude [Liu16; Mat02]. Lu et al. investigated the so-called island scanning strategy and the influence of the individual islands' size. An island size of $2 \times 2 \text{ mm}^2$ resulted in the lowest residual stress in their study, which they related to a stress release due to cracking. Due to the combination of good density and residual stress state, they concluded that an island size of $5 \times 5 \text{ mm}^2$ was the best choice for their specific application of mold inserts with a cooling channel [Lu15].

Robinson et al. compared various scanning strategies and their impact on residual stresses using a variety of measurement techniques. They found no benefit of using island scanning regarding residual stresses. In their study, bidirectional parallel scanning with a 90° rotation between layers leads to the lowest residual stresses. [Rob18]

In general, an individual layer's scanning pattern comprises a contour, contour fill, and hatching pattern, each of which is scanned with individual laser parameters. The contour is used to improve the surface quality of the part. The hatching ensures dense parts and the contour fill vectors connect the two. Artzt et al. found that contour scanning is a trade-off between residual stresses and surface quality, where contour parameters that lead to lower roughness also induced higher residual stresses [Art20]. The combination of various scan directions and laser parameters in a single layer illustrates the complex thermal history of LPBF parts and the intricate development of residual stresses.

The individual hatch vectors in a single layer are exposed with specific laser powers and scanning speeds, both of which impact the heat input and, thereby, the stresses. However, the relationship between laser power, scanning speed, and resulting stress state is complex. Mukherjee et al. projected a linear rise of residual stress with increasing laser power and, likewise, a linear reduction with increasing scanning speed using numerical modelling [Muk17]. Similarly, Bian et al. reported an increase in tensile stresses when increasing the laser power while keeping other parameters constant [Bia20]. Ali et al. also showed that lower laser powers combined with lower scanning speeds reduce residual stresses [Ali18]. On the other hand, Xiao et al. reported a non-monotonous stress response to changes in the laser power, scanning speed, and hatch spacing, where the scanning speed was found to have a more substantial impact on the final stress state than the other two parameters [Xia20]. Supporting this, Shiomi et al. showed a decrease of residual stress magnitude by increasing the scanning speed up to a specific turnaround point, after which residual stresses increased again [Shi04].

Along with the laser scanning parameters such as laser power and scanning speed, the part's geometry also has to be considered due to its close relation to the residual stresses, especially

their magnitude. While approaches to standardize test geometries have been published, these are rarely used in other studies [Moy12; Tay21].

Overhang structures are a geometrical detail featured by most real-world applications of LPBF. The powder is molten without solidified material to bond to below to create these overhangs. The resulting down-skin areas are challenging from surface quality and residual stress perspectives. Since the thermal conduction through the powder is much worse than through solid material, heat accumulates here, often leading to undesirable, residual stress-induced distortions [Kam19]. Support structures are often used to prevent these geometrical deviations and facilitate the part production, but they have to be removed after the process [Han18]. Since post-processing increases time and cost, it is generally desired to consider and counteract the possible distortions in the original design of the parts to ensure geometrical accuracy.

In addition to the part geometry, even the position of the part on the substrate affects the residual stresses. According to Casavola et al., their study found stress differences of more than 100 MPa for parts with equal geometry and processing parameters depending on their positioning [Cas08]. The material and thickness of the substrate also influence the residual stresses. Mercelis and Kruth concluded that increasing the thickness of the substrate would reduce the stress magnitude in the part [Mer06]. If the part and substrate are not the same material, strain incompatibilities can be induced due to differences in the thermal expansion, causing further residual stresses and possible part deformation when the substrate is removed.

The results above illustrate the difficulties in accurate residual stress determination and interpretation for LPBF parts. Generally, the process parameter sets are not identical, making results hard to compare. Sometimes, the process parameters are not disclosed at all. Additionally, commercially used scanning strategies and their complexity make it tough to dissect the influence of individual laser tracks on stress formation.

To better understand how residual stresses are generated and how they develop, it is necessary to disentangle the LPBF process to isolate individual effects, for example, by using simplified process parameters, i. e. unidirectional scanning patterns. Additionally, the stress-free lattice spacing must be precisely determined when using diffraction methods to determine residual stresses. Chemical changes during melting and possible partial vaporization have to be considered not only from powder to final part but also as gradients in the final part. Uncertainties in the d_0 value can drastically affect the calculation of absolute stress values, possibly even returning the wrong sign for the stresses [Hau97; Wit07]. Ultimately, only *in situ* experiments allow the experimental observation of the stress formation and evolution mechanisms as they occur and are therefore essential to further the fundamental process knowledge.

2.1.6.6 Mitigating residual stresses

Since residual stresses, predominantly if tensile, can be detrimental to a part's performance, their reduction is desirable in most cases. Besides the parameter influences mentioned above, two more in- and post-process adjustments are presented here.

Firstly, both the powder bed and the substrate plate can be preheated to reduce the thermal gradient relative to the energy input by the laser. The reduced thermal gradient lowers the residual stresses in the final part. This effect has been reported for substrate temperatures up to 250 °C, which reduced residual stresses up to zero [Buc14; LeR18; Shi04]. Simultaneously, preheating the substrate might influence the microstructure of the part as prolonged times at higher temperatures promote grain growth and might cause the formation of precipitates [Bar19b].

Secondly, post-process heat treatment for stress relief is commonly used, with suitable heat treatment procedures being available from conventionally manufactured parts. However, relieving the stresses results in a plastic deformation, which reduces the geometrical accuracy and might necessitate further post-processing to obtain the desired shape. Therefore, averting the generation of significant residual stresses in the first place, during the process, is highly desirable.

2.2 State of the art in synchrotron technology

The possibility of performing *in situ* experiments using X-rays has emerged only fairly recently. High photon fluxes are necessary to allow short acquisition times that enable high temporal resolutions in engineering and materials science applications. Specific processes such as LPBF occur on such short time scales that relevant phenomena occur in fractions of a second. Conventional laboratory X-ray tubes cannot be used for such experiments. However, the development and advancements of synchrotron light sources laid the groundwork to enable investigations such as those presented in this thesis. Since the discovery of synchrotron radiation in the 1940s, the steadily improved design and execution of dedicated sources of synchrotron radiation have led to dramatic increases in peak photon fluxes as shown in figure 2.4 [Rob15]. Synchrotron X-rays offer superior collimation, high intensity and brightness, a vast adjustable energy spectrum, and a defined temporal structure and polarization compared to ordinary laboratory X-rays.

In short, a synchrotron is a device where electrons are kept on a circular path at close to the speed of light. Since accelerated charges emit electromagnetic radiation, the circular motion results in intense electromagnetic radiation emitted in the tangential direction [Jae20]. This radiation is tuned and amplified in insertion devices, i. e., wigglers and undulators, which are characteristic of the third generation of synchrotron sources. As the name suggests, these devices are inserted in the straight sections of the storage ring between the bending magnets. Besides (damping) wigglers, undulators have emerged as the most influential component of

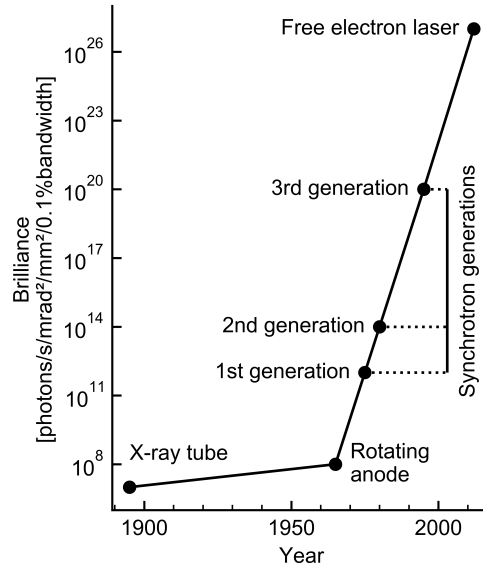


Figure 2.4: X-ray sources and the evolution of their brilliance over time. Graphic adapted from Als-Nielsen and McMorow [Als11].

modern synchrotron sources. An undulator features a closely-spaced, periodic magnetic structure of alternating polarity and is several meters long. When the electron beam travels through the undulator, the beam path oscillates in the horizontal plane. At each bend, overlapping radiation cones are emitted, resulting in constructive interference and amplification of the radiation intensity, which can be used for a range of experiments. The resulting radiation wavelength can be adjusted and optimized for the desired application by manipulating the gap between the individual magnets. [Bil05; Rob15]

2.2.1 X-ray generation at PETRA III

PETRA III (short for *Positron Electron Tandem Ring Accelerator*) at Deutsches Elektronen-Synchrotron (DESY) located in Hamburg-Altona, Germany is a storage ring with a circumference of 2.304 km operating at 6 GeV. It has the highest brilliance of any synchrotron facility in the world exceeding 1021 ph/(s mm² mrad² 0.1% bw). Experiments can be conducted at 24 different beamlines divided onto three experimental halls. [HAS21]

The experiments presented in the present thesis were carried out at the P07 High-Energy Materials Science (HEMS) beamline operated by Helmholtz-Zentrum Hereon GmbH. The design, execution, facilities, and equipment of the beamline were detailed by Schell et al. [Sch13]. This beamline offers an energy range of 50 keV to 200 keV and a maximum photon flux on the sample of 5×10^{12} ph s⁻¹ at 100 keV by virtue of a in-vacuum undulator IVU-21 [Deu21]. The maximum beam size is 1×1 mm².

The HEMS beamline offers several stations to conduct experiments. In the present work, beam-times were conducted at the EH1 side station and the EH3 main station. Both endstations

feature precise positioning systems and a variety of detectors for wide-angle diffraction experiments. The EH3 main station has a significantly higher photon flux than EH1 and allows shorter exposure times and higher acquisition rates.

2.2.2 Detector technology

Since Wilhelm Conrad Röntgen first discovered X-rays on a fluorescent film, remarkable breakthroughs have been achieved in X-ray detection. Modern area X-ray detectors feature a two-dimensional matrix of sensitive pixels using a variety of detection technologies to convert a radiant power distribution into an electrical signal [He09]. In the present study, two different detector systems were used.

The first detector is a PERKINELMER XRD 1621¹. The detector features an array of 2048×2048 pixels with a pixel size of $200 \times 200 \mu\text{m}^2$, resulting in an active area of about $410 \times 410 \text{ mm}^2$. In this array, each pixel includes an amorphous silicon photodiode and a switching thin film transistor (TFT) in the same electrical circuit and has a counter depth of 16 bit (maximum counts: 65 536). A caesium iodide (CsI) scintillator is used to convert the incident X-rays into visible light to activate the photodiodes. [Per06]

The second detector that was used is a Pilatus3 X CdTe 2M by DECTRIS, Baden, Switzerland. It has a resolution of 1475×1679 pixels with a $172 \times 172 \mu\text{m}^2$ pixel size. Due to its panel design with an array of 3×8 modules, the detector surface has an inactive area of 8.5 %. Each pixel has a counter depth of 20 bit, resulting in a maximum of 1 048 576 counts. The detector technology is described as a hybrid single-photon counting system free of signal noise and dark current. X-rays are absorbed by the detector surface and directly converted into an electric signal without converting it to visible light first, with every absorption event being counted individually. The detector modules have to be water-cooled during use. [Dec20]

2.2.3 Applications for synchrotron radiation in LPBF investigations

Several notable *in situ* experiments using synchrotron radiation have been reported in the literature in recent years. The two main applications are imaging and diffraction methods.

Several research groups have reported *in situ* X-ray radiography experiments with custom LPBF (or LPBF-like) systems. The first study to document these kinds of experiments was published by Zhao et al. in 2017 [Zha17]. In 2018, Calta et al. and Leung et al. presented their findings [Cal18; Leu18]. Then, Wakai et al. introduced their experimental setup [Wak20]. These imaging experiments delivered valuable information regarding the laser-matter interaction and showed how porosity is formed and how cracks develop at extremely high acquisition speeds.

¹This detector is now sold by VAREX IMAGING, Salt Lake City, USA, who acquired the Medical Imaging division from PERKINELMER (<https://www.vareximaging.com/varex-imaging-acquires-perkinelmer-medical-imaging>, last visited on: May 31, 2022).

One other imaging method is tomography, which creates a three-dimensional reconstruction of the sample, especially its inner structure. Various contrast-detection mechanisms allow phase analyses, crack detection, and porosity analysis. A group from the European Synchrotron Research Facility (ESRF) presented an experimental setup that allows for *in situ* tomography experiments during LPBF. After the laser exposure of a single layer is finished, the sample is rotated while being irradiated by the synchrotron beam to gather a single tomogram. This way, the researchers can detect the defect formation and evolution after each layer [Lhu20]. Tomography is also extensively used in *ex situ* applications. When using synchrotron radiation as a light source, researchers profit from submicron resolutions and fast acquisition times, especially compared to laboratory-scale X-ray sources.

The second main field of LPBF research next to imaging methods are scattering experiments, especially *in situ*. In addition to their imaging results, Zhao et al. also presented diffraction experiments analyzing the phase transformation of a titanium alloy using wide-angle X-ray scattering (WAXS) [Zha17]. Hocine et al. presented a custom, advanced LPBF system designed for *in situ* diffraction experiments under realistic LPBF conditions. Their system was primarily used in reflection mode to investigate phase transformations and thermal strain evolution in a titanium alloy [Hoc20a; Hoc20b]. Also, in 2020, Calta et al. compared the cooling kinetics of two titanium alloys in LPBF using their custom system [Cal20].

Moving to smaller scattering angles in small-angle X-ray scattering (SAXS), Wahlmann et al. reported *in situ* diffraction investigations simulating the cyclic heating and cooling conditions during LPBF in a quick-responding furnace. They analyzed the precipitation and dissolution of the γ'' phase in a nickel-base alloy [Wah19]. Later, they also performed *in situ* diffraction experiments with the custom LPBF system also used for this thesis [Uhl20] under actual LPBF conditions, employing a combination of SAXS and WAXS measurements [Wah21]. Synchrotron radiation diffraction is also widely used for *ex situ* applications to investigate texture as well residual strains and stresses, see section 2.1.6.3.

Aims of this work

3

The literature review in chapter 2 demonstrated the uncertainties still associated with LPBF despite its growth and success and the need for investigations of in-process phenomena. One facilitator of *in situ* experiments that emerged only recently is the extremely high photon flux and brilliance of third-generation synchrotron X-ray sources. The associated high energies allow increased transmittable material thicknesses, enabling the replication of realistic LPBF conditions. In the present work, high-energy X-rays are used for *in situ* diffraction experiments to elucidate some of the beforementioned uncertainties and augment the fundamental process knowledge. In consequence, four primary goals are set for this study.

The *first goal* of this work is to investigate microstructural responses to laser processing. The impact of laser irradiation during the initial melting and solidification severely impacts the microstructure. Special care will be taken to investigate the effect of the repeated laser scanning and inherent heat treatment in LPBF. This thermal cycling impacts the phase composition, grain growth, crystallographic texture, microstructural defects, and the chemical composition of the material. *In situ* diffraction allows observing these reactions as they occur.

The *second goal* is to identify and explain the phenomena of stress formation and evolution in LPBF experimentally. As mentioned before, conventional *ex situ* experiments detect the final state of the part, not how it got there. While *ex situ* stress measurements give essential insights into the influence of processing parameters on the final stress state, the fundamental knowledge of the underlying mechanisms is crucial to achieving total process control. Therefore, *in situ* diffraction experiments are used to resolve these mechanisms to reach the second goal.

The *third goal* of this work is devising an approach for *in situ* temperature evaluations. Stresses are developed in solidified material and, therefore, inside the part, where temperature measurements are not possible during the process. Moreover, the part is embedded in loose powder in LPBF, which poses further challenges towards a metrological temperature analysis. Therefore, the thermal expansion of the crystal lattice, which is reflected in the diffraction patterns, shall be used to analyze the material's temperature.

Finally, based on the temperature and knowledge of the corresponding stress-free lattice parameter, the *fourth goal* of this thesis is the determination of absolute stress values, which will add to the more generalized stress formation and evolution phenomena discussed above.

In order to achieve these goals, an experimental setup is used that replicates the industrial process in detail. This LPBF device is designed to be integrated and used at the experimental

3 Aims of this work

facilities at the *High Energy Materials Science (HEMS)* beamline at the PETRA III synchrotron. Additionally, the importance of the stress-free lattice spacing will be considered via a distinctive set of experiments to investigate temperature and chemical composition dependencies. *Ex situ* microstructure analyses will complement the *in situ* diffraction experiments, which are the focal point of this work. The combination of this LPBF device and the highly temporally resolved X-ray diffraction data aims at giving unprecedented insights into the LPBF process.

4

Experimental methods

This chapter features a detailed description of the experimental procedure regarding the *in situ* experiments, other utilized characterization methods, and the d_0 investigations.

4.1 Conducting the *in situ* experiments

4.1.1 Brief description of the custom LPBF system

The custom LPBF system is designed to replicate the conventional, industrial LPBF process with minor adaptations to facilitate concurrent X-ray diffraction experiments. The primary deviations are the build volume capacity on the one hand, which allows manufacturing a single part with maximum dimensions of $70 \times 10 \times 3$ mm, and, on the other hand, the X-ray transparency of the chamber, which enables the realization of *in situ* X-ray diffraction experiments in the first place [Uhl17]. In the dissertation of Erwin Krohmer [Kro22], an in-depth discussion of the conceptualization, design, and functionality of the experimental system is provided, and the comparability to a conventional LPBF system is examined in detail. The present section shall merely give a brief overview of the mode of operation.

The custom LPBF system consists of three modules: the control cabinet, the recirculation and filtration system, and the process chamber. The control cabinet houses the laser, electronics, and the controlling computer as an interface for system control. The second module consists of a circulation pump and a two-step filtration system, ensuring a clean atmosphere in the process chamber without residual particles and contamination emerging during laser-matter interaction.

Lastly, the process chamber represents the centerpiece of the machine, which is schematically shown in figure 4.1. A system of three linear axes facilitates the replication of the LPBF process. The first axis moves the building platform laterally in the transverse direction (TD), perpendicular to the incident X-ray beam direction. On the one hand, this axis moves the platform into the recoating position, and on the other hand, the rough lateral position of the measuring volume of the synchrotron beam is set in this way. Since the synchrotron beam is stationary, its position relative to the sample can be changed by moving the build platform in TD.

The second axis realizes the vertical movement in the building direction (BD). It should be noted that the glassy carbon plates are affixed to the first axis and do not change their position when the build platform is moved downwards or upwards. The static vertical position of the

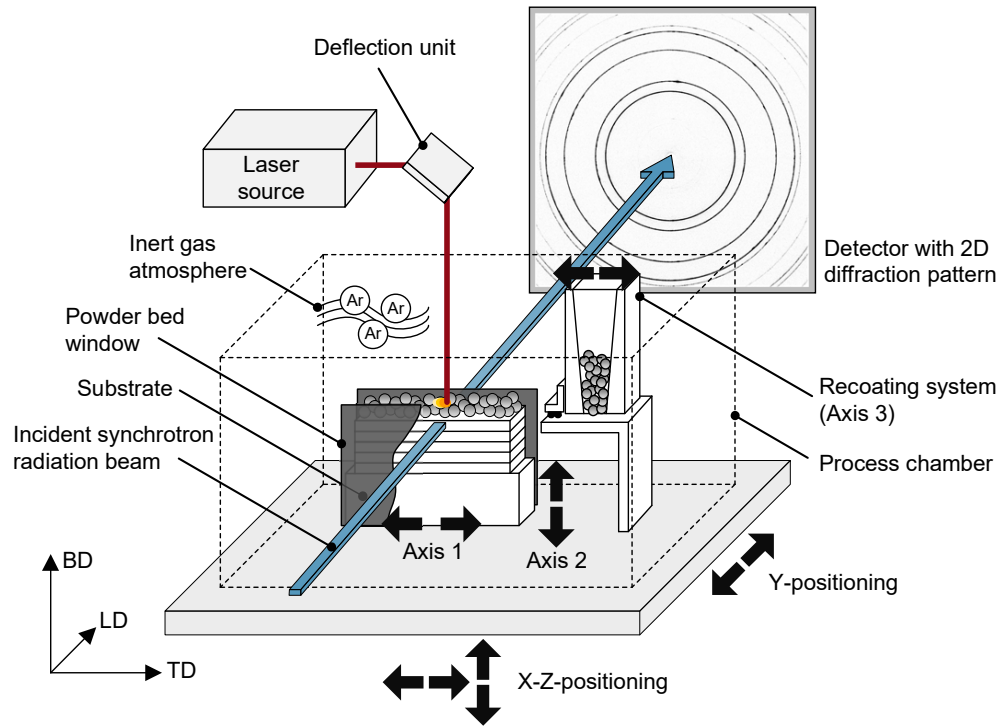


Figure 4.1: Schematic drawing of the LPBF system's process chamber on positioning device.

glassy carbon ensures that the upper edge of the powder bed always remains at the same height relative to the coating mechanism. The third axis, moving parallel to the first axis, is used for powder recoating. A hopper is mounted on this axis, filled with powder, and open at the bottom. A plate prevents uncontrolled powder outflow in the hopper's idle position. Although a small amount of powder is spilled, it collects on the plate and thus closes the opening automatically. During coating, the build platform is first moved towards the hopper's idle position and remains there. The hopper is then moved over the build platform to the end of the substrate plate and back again. The hopper is designed so that when the hopper is moved back towards the idle position, an elastomer lip sweeps aside the excess powder and levels and smooths the powder bed.

Above the chamber, the deflection unit, also called the scanner, is mounted, which is responsible for focusing and deflecting the laser beam. It can be actively cooled using an external water-cooling unit and is connected to the laser by a fiber optic cable. The laser is a YLR-400-AC manufactured by IPG LASER GMBH, Burbach, Germany, operating in continuous wave mode at a wavelength of $\lambda_L = 1070 \text{ nm}$. It has a nominal power output of $P_L = 400 \text{ W}$. The experimental system is equipped with several safety mechanisms that prevent the accidental leakage of laser radiation. These safety mechanisms are integrated into the interlock system at PETRA III. Consequently, the laser can only be switched on if the door of the experimental hutch is locked.

4.1.2 Experimental procedure

Before a test can be started, the substrate plate and the glassy carbon platelets must be inserted into the sample holder. It is essential to ensure that the substrate plate is installed as level as possible to achieve a uniform powder layer thickness. Both the substrate plate and the glassy carbon plates are fixed with screws.

Since the first layer is decisive for the bonding of the manufactured component to the substrate plate, special care is taken with applying the first powder layer. Due to manufacturing tolerances of the substrate plates and variations during insertion, the first layer's thickness is adjusted manually for each sample. The aim is to set the thickness so that the substrate surface is still slightly shimmering through the powder but is completely covered at the same time. Stepwise lowering or raising of the substrate plate enables the precise configuration.

After the first layer has been applied, the measurement volume is selected by moving the entire process chamber on the experimental hutch's positioning table. It is verified that the correct aperture size is set. An edge scan is then performed to determine the top edge of the powder. The desired vertical position of the measuring volume can then be set by moving the process chamber upwards the desired distance. In measurement mode 1, section 4.1.6, for example, 150 μm distance to the surface is selected.

Then, the process chamber is flushed with argon before carrying out a manufacturing process. Residual oxygen can lead to process complications due to oxidation and be a potential safety hazard when using flammable materials. For this purpose, the process chamber is sealed, and the argon flow is started. Excess oxygen is forced out through a simple outlet valve. When the oxygen content, measured by an O_2 sensor, reaches the threshold value of 2000 ppm, the circulation pump is switched on to purge oxygen from the rest of the system as well. The target value at which a production process can be started is an oxygen content of 1000 ppm.

When that level is reached, the experimental hutch is searched and locked as per the synchrotron facility's safety guidelines. With the gauge volume set, the appropriate scan vector file is loaded, and the laser and build parameters are set and checked so that the LPBF system is ready to start the process.

Simultaneously, the image acquisition parameters are set, and the X-ray beam shutter is opened. File names, acquisition rate and mode, and the number of acquired images are checked. Depending on the measurement mode, see section 4.1.6, the detector is armed, or image acquisition is started manually. Then, the manufacturing process is begun and runs automatically for the specified amount of layers. It begins with the laser exposure of the first layer. Then, the build platform is moved down by one layer thickness, the recoating mechanism is executed as described above, and, after the build platform reaches its idle position again, laser exposure is repeated for the next layer.

After the process is finished, the circulation pump is turned off and sealed. The process chamber is opened, and excess powder is vacuumed using a wet separator. Then, the glassy carbon platelets are taken out, and eventually, the sample can be extracted from the process chamber. Before the following experiment is started, the hopper fill level is checked and replenished if necessary.

4.1.3 Calibration using LaB_6

During the LPBF system's installation, the process chamber is mounted on either the heavy-load hexapod (P07 EH3) or the XZ-table (P07 EH1). Subsequently, the detector distance is set to gather an appropriate number of diffraction rings on the detector's active area. After this adjustment, the sample-detector distance is kept constant for the remainder of the beamtime unless a material change occurs. The sample-to-detector distance has to be determined with the highest precision possible to enable the correct evaluation of the diffraction angles and, therefore, internal stresses. A calibration measurement using lanthanum hexaboride (LaB_6) powder provides the relevant data. The LaB_6 sample is placed between the glassy carbon windows to ensure the exact positioning like the actual samples during the *in situ* experiments. A diffraction pattern of LaB_6 is collected with the same beam and exposure parameters as the *in situ* measurements. This calibration measurement is evaluated using the python software library *pyFAI*, see section 4.3.

4.1.4 Materials

In the present thesis, two different materials were investigated: Inconel 625 and commercially-pure titanium grade 1. Inconel 625 is a nickel-base alloy with high strength, creep resistance, and excellent corrosion behavior that makes it suitable for demanding environments such as heavy water plants [Sha01]. It is widely used in LPBF applications. Due to its high strength even at elevated temperatures, high residual stresses occur when Inconel 625 is processed via LPBF, which makes it particularly interesting for *in situ* stress analysis during LPBF. In the present work, an Inconel 625 powder feedstock material supplied by M4P MATERIAL SOLUTIONS GMBH, Magdeburg, Germany, was used. Figure 4.2a shows a SEM image of the powder, whose particle size ranged from 20 μm to 63 μm . Additionally, the nominal chemical composition as supplied by the manufacturer is given in table 4.1.

Titanium was chosen as a second material to investigate for several reasons. First of all, commercially-pure titanium grade 1 is a pure metal without alloy elements and minuscule contaminations, see table 4.1. This purity dramatically simplifies the complex matter of d_0 since a lack of other elements naturally means that the chemical composition does not change during processing. It can be safely assumed that the feedstock powder d_0 is equal to the final parts' d_0 regardless of the processing parameters. Secondly, commercially-pure titanium grade 1 undergoes a phase transformation from the low-temperature, hexagonal closed-packed α phase to the high-temperature body-centered cubic β phase. Understanding how, where, and when the phase transformation occurs during LPBF and how it impacts the stress state

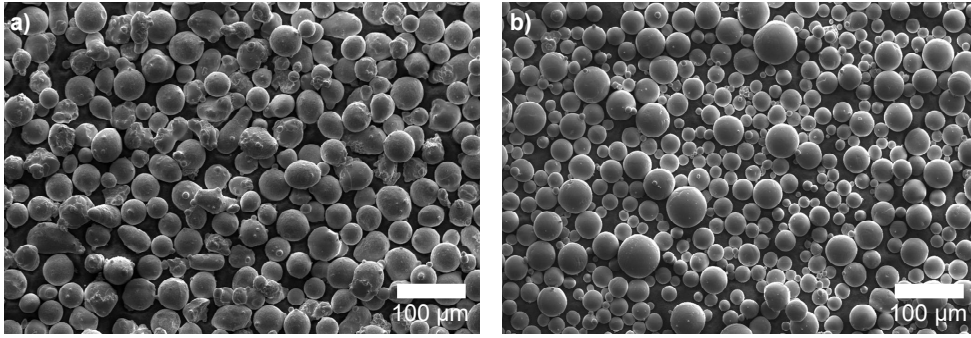


Figure 4.2: SEM images of feedstock material kindly provided by Erwin Krohmer. a) Inconel 625 b) Commercially-pure titanium grade 1

will add to the basic process understanding. The commercially-pure titanium grade 1 powder was procured from ADVANCED POWDERS & COATINGS, Quebec, Canada, and is shown in figure 4.2b.

In addition to the feedstock materials, glassy carbon plates were acquired from HTW HOCHTEMPERATUR-WERKSTOFFE GMBH, Thierhaupten, Germany. These platelets were used as X-ray transparent powder bed boundaries. Parts were built on substrates with the substrate material varying with the feedstock. Inconel 625 parts were manufactured onto S355J2 steel substrates, while commercially-pure titanium grade 1 parts used titanium grade 2 substrates.

4.1.5 Process parameters

The process parameter sets investigated during the *in situ* experiments were determined in preliminary experiments at the INSTITUT FÜR WERKZEUGMASCHINEN UND FABRIKBETRIEB (IWF) by Erwin Krohmer [Kro22]. The laser power P_L and scanning speed v_L were chosen under part quality considerations, i. e., least amount of porosity, and experimental aspects, i. e., maximum

Table 4.1: Nominal chemical compositions of used feedstock materials as provided by manufacturers

Inconel 625		Titanium	
Element	wt%	Element	wt%
Ni	balance	Ti	balance
C	< 0,03	C	0.01
Mo	8,4	O	0.12
Cr	20,7	N	0.03
Si	0,6	H	0.002
Mn	0,4	Fe	0.03
Nb	3,5	Others	0.4
Fe	0,5		

Table 4.2: Process parameters used in the experiments

	Set 1	Set 2	Set 3
	$P_L = 55 \text{ W}$	$P_L = 165 \text{ W}$	$P_L = 275 \text{ W}$
	$v_L = 50 \text{ mm s}^{-1}$	$v_L = 456 \text{ mm s}^{-1}$	$v_L = 760 \text{ mm s}^{-1}$
L-Scan	In625, Ti	In625	In625, Ti
T-Scan	In625	In625	In625
TI-Scan	Ti	-	Ti

data acquisition rate. Both the industrial standard and „slower“ parameter sets were evaluated with slower scanning speeds allow for higher data densities concerning the maximum acquisition rates of the detectors used in the experiments.

Eventually, laser powers of $P_L = 55 \text{ W}$, 165 W and 275 W and corresponding scanning speeds of $v_L = 50 \text{ mm s}^{-1}$, 456 mm s^{-1} and 760 mm s^{-1} were chosen. The parameters are shown in table 4.2.

In addition to the laser parameters, the scanning pattern, also called scanning strategy, was identified as a second central influencing factor on the manufactured part's condition. The scanning strategy has a deciding impact on the heat input and the resulting temperature gradients in the working plane and the material below. The investigated patterns were chosen under similar considerations as the laser parameters. In total, three individual scanning patterns were evaluated. They are shown schematically in figure 4.3. All investigated scanning patterns feature parallel, unidirectional scanning vectors without meandering, oriented parallel to one of the principle observed directions, either TD or LD, to conform to the assertions formulated in section 2.1.6.5.

The longitudinal scanning pattern (L-scan) has unidirectional scanning vectors parallel to the transmission direction of the primary synchrotron beam and the through-thickness direction of the part. Hatches are scanned from left to right. The transverse scanning pattern (T-scan) features unidirectional scanning vectors perpendicular to the incident beam direction, parallel to the movement of the build platform, TD. The hatch direction is bottom to top, from incidence point to exit point regarding the synchrotron beam. The transverse island scanning pattern (TI-scan) utilizes unidirectional scanning vectors perpendicular to incident beam direction with the length of individual vectors equal to the L-scan. Thereby, the area to be exposed is divided into nine islands that are scanned from left to right, with each islands' hatches being scanned from bottom to top first.

For all experiments presented here, the part shape was kept constant. Thin cuboid, wall-like components were built with dimensions of $20 \times 5 \times 2.5 \text{ mm}$.

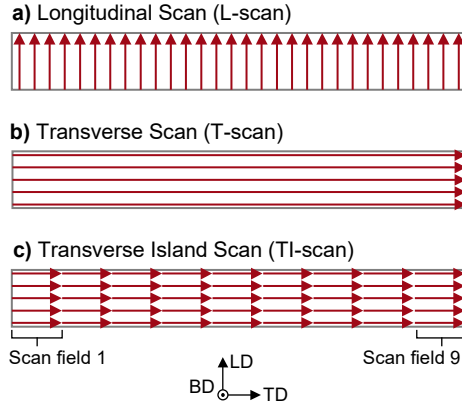


Figure 4.3: Schematic drawing of scanning strategies used in the present work. a) Longitudinal scanning b) Transverse scanning c) Transverse island scanning

4.1.6 Detectors and measurement modes

Different techniques were used for image acquisition in this work, depending on the detector and the experimental facility. Experiments at the main station P07 EH3 could be conducted with higher acquisition rates due to higher available photon fluxes than the side station P07 EH1. Additionally, the Pilatus detector was procured later and was not available for the first experiment sessions.

- **PERKINELMER XRD1621, measurement mode 1:** Here, the *post trigger* function of the detector was used. At the beginning of the experiment, a single dark image is recorded, which is then subtracted from all subsequent light images. In this way, a pre-specified number of diffractograms, for example, 20 000 for experiments with $P_L = 55$ W, were recorded in series. This type of image acquisition records many unusable blank images that must be sorted out before further processing.
- **PERKINELMER XRD1621, measurement mode 2:** In this measurement mode, the process chamber had to be manually shifted by one layer thickness after exposure of each layer. Therefore, the *post trigger* function could not be used here for the entire process. Instead, the *post trigger* was reset before each exposure, significantly reducing the number of images since only one layer was recorded. Thereby, the number of blank images was drastically reduced, although sorting and filtering were still required. In practice, however, this variant proved to be prone to user errors, so layers were sometimes missing because the manual triggering was forgotten.

Table 4.3: Scan vector length, count and orientation for used scanning patterns.

Name	$ \vec{v}_L $	$n_{\vec{v}_L}$	Orientation
L-Scan	2.38 mm	168	$\vec{v}_L \parallel \text{LD}$
T-Scan	19.68 mm	19	$\vec{v}_L \perp \text{LD}$
TI-Scan	2.38 mm	19×11	$\vec{v}_L \perp \text{LD}$

- **DECTRIS Pilatus3 X CdTe 2M:** The Pilatus detector offers the possibility to be triggered by an external signal. Similar to the *post trigger* function of the Perkin-Elmer, the number of images to be acquired was set before the experiment was started, depending on the parameter set. The detector is then „armed“ and starts the serial image acquisition as soon as the laser exposure is started. This way of execution is similar to that of measurement mode 2, since the detector had to be armed again before each layer, and errors could occur here as well. However, with this variant, the fewest blank images were generated, and filtering was simplified since the start of each layer’s image acquisition was held constant relative to the laser exposure.

4.2 Determining the stress-free lattice spacing d_0

There are several methods to determine this value accurately. Various factors influencing d_0 have to be considered [Wit07]:

- Chemical composition,
- temperature,
- and microstructure.

Concerning this thesis, the chemical composition can be assumed as constant for commercially-pure titanium since the amount of contamination is negligible, and no changes during the LPBF process are expected. However, the nickel-base alloy Inconel 625 has several alloying elements whose weight fractions can change due to vaporization. Therefore, the chemical composition had to be evaluated after the manufacturing process.

The temperature is one of the critical aspects of the present work. Following Withers et al., even a temperature change of $\Delta T = 10$ K causes a change in d_0 in the range of 10^{-4} and lead to an inaccurate stress calculation [Wit07]. Therefore, the temperature in the gauge volume during the *in situ* experiments has to be known (or at least approximated). Additionally, the corresponding d_0 at that temperature must be determined.

4.2.1 Chemical composition investigations

It has been reported in the literature that the highly focused, localized energy input during LPBF can lead to local d_0 changes. For example, Wang et al. showed changes in d_0 over the height of the manufactured part [Wan17]. The Inconel 625 samples built as part of the present thesis were investigated regarding their chemical composition and potential compositional gradients using *ex situ* wavelength-dispersive X-ray spectroscopy (WDX).

The WDX experiments were carried out at the ZENTRALEINRICHTUNG ELEKTRONENMIKROSKOPIE (ZELMI) at TECHNISCHE UNIVERSITÄT BERLIN. The specimens were embedded in epoxy resin and cured following standard metallographic practices. For each specimen, the TD-BD plane was ground, polished, and coated with a thin layer of carbon to ensure the electric conductivity of the resin.

In a JEOL JXA-8530F WDX device, the composition was then analyzed in the same regions observed during the *in situ* experiments, e. g., the left edge, center, and right edge of the sample. The probe diameter was set to 20 μm . Line scans along the building direction were performed to investigate compositional gradients along this axis. Seven elements were analyzed: Nickel, chromium, molybdenum, niobium, silicon, iron, and manganese.

Results of WDX experiments For a given sample, several observations were made. First, a diffusion zone was found between the steel substrate and the Inconel 625 sample. In this zone, a gradient of iron was detected. While iron is the principal constituent of the substrate, it is also part of the nominal composition of Inconel 625 with a contribution of $x_W \approx 0.5 \text{ wt}\%$ according to the manufacturer's specification. Increased iron contents were found up to 250 μm into the Inconel 625 part. Besides that, no clear trends or gradients were found for any other investigated elements. Stochastic changes in composition by up to 1 % were observed, which are generally within the error limits of the characterization method. Furthermore, the WDX gauge volume only had a diameter of 20 μm and a few microns in depth compared to the synchrotron gauge volume with its dimensions of $0.75 \times 0.07 \times 2.5 \text{ mm}^3$.

Similar to the building direction, the differences between the left edge, center, and right edge measuring positions were deemed stochastic, too, due to the lack of discernible gradients and trends. Therefore, it was concluded that a single d_0 value was sufficient per parameter set. Nevertheless, the WDX analyses showed different chemical compositions for the various sets of process parameters, likely due to the varying energy input caused by manipulating the laser power and scanning speed together with the scanning pattern. Therefore, each parameter set demanded an individual d_0 determination.

4.2.2 Fabrication of specimens for d_0 investigations

After completing the WDX experiments, specimens were produced for d_0 measurements. These specimens had to fulfill several requirements. They were manufactured on the same LPBF machine using the same process parameters as the *in situ* and WDX samples to ensure identical chemical composition. Secondly, the subsequent diffraction experiments with concurrent heating had to measure a stress-free condition. Such a state was achieved by cutting out small cuboids from the LPBF parts, see figure 4.4a. For each part, three cuboids were removed via wire electrical discharge machining (WEDM) at FRAUNHOFER-INSTITUT FÜR PRODUKTIONSANLAGEN UND KONSTRUKTIONSTECHNIK (IPK). Several specimens were produced per part and parameter set to improve the statistics of the d_0 measurements. The geometry of the cuboids was chosen according to the experimental conditions at the P07 beamline at PETRA III.

The biggest beam aperture at the P07 beamline is $1 \times 1 \text{ mm}$. The specimens need to be fully immersed in the synchrotron beam, as that way, the equilibrium and, therefore, the stress-free state is measured, see section 2.1.6.1. Therefore, the specimens were produced with an edge length of 700 μm for complete immersion, see figure 4.4b.

4 Experimental methods

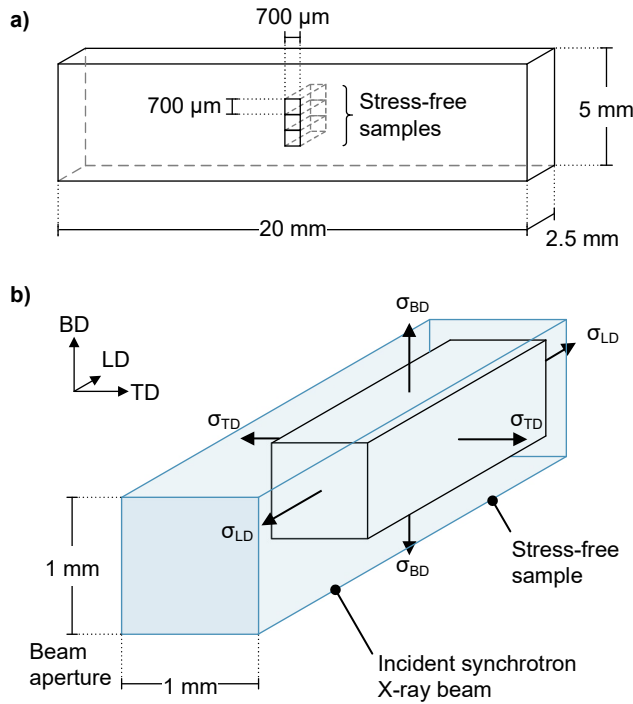


Figure 4.4: a) Stress-free sample geometry and sampling positions in relation to the whole specimen. b) Stress-free sample fully immersed in the incident synchrotron beam. Since equilibrium conditions have to be fulfilled, the resulting diffraction pattern shows the stress-free lattice spacing d_0 .

4.2.3 Synchrotron experiments using in situ heating

In situ diffraction experiments were carried out at the P07 beamline at PETRA III to determine the stress-free lattice spacing d_0 . Additionally, the specimens were placed in an ANTON PAAR DHS1100 furnace, which was kindly provided by HELMHOLTZ-ZENTRUM BERLIN to determine the temperature dependence of d_0 as well. The experimental setup is schematically shown in figure 4.5.

For each parameter set, three cuboids are placed inside the furnace. Since full diffraction rings were to be collected, the specimens had to be raised from the heating plate to prevent shadowing of the lower part of the diffraction cone. A 10 mm high steel block was placed on the furnace's heating plate, followed by a sheet of glassy carbon with a thickness of 1 mm. The glassy carbon prevented the X-ray irradiation of the steel block below, which would have resulted in diffraction and possible peak overlap with the Inconel 625 reflections. Since glassy carbon is amorphous, partial irradiation only resulted in diffuse scattering, not impeding the d_0 analyses. Additionally to the specimens, a thermocouple is placed on the glassy carbon to confirm that the programmed temperature of the heating plate is reached.

The specimens are placed parallel to the incident beam at the rear end of the glassy carbon plate so that the diffraction cone is unattenuated. Then, the measuring positions are determined by moving the sample stage accordingly. These three measuring positions are examined for each temperature step during the experiment. The temperature is increased in $\Delta T = 50$ K increments up to a maximum temperature of $T = 800^\circ\text{C}$. Here, the thermocouple on top of

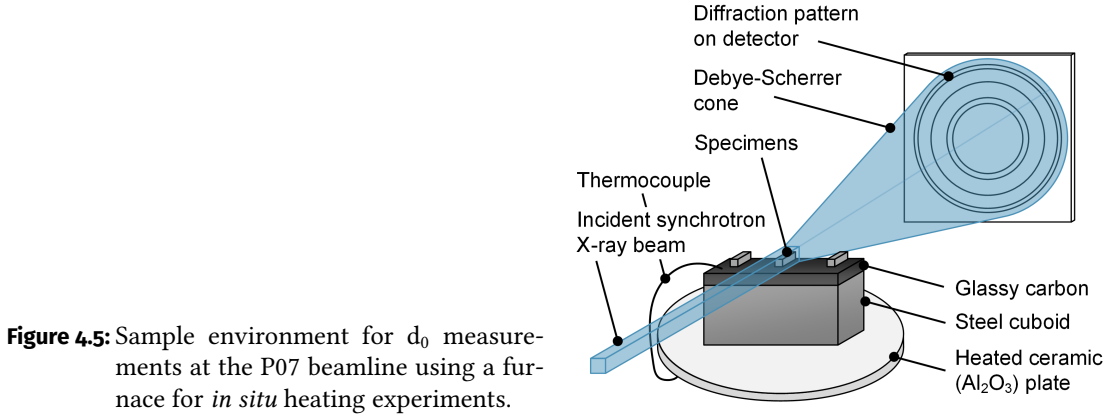


Figure 4.5: Sample environment for d_0 measurements at the P07 beamline using a furnace for *in situ* heating experiments.

the glassy carbon references the actual temperature. Due to the block of steel and the glassy carbon plate between the heating plate and the specimens, the temperature for the heating plate has to be set significantly higher.

A 2D diffraction pattern was collected for every specimen at each temperature increment. During the subsequent analyses, the peak position of the (311) reflection was evaluated depending on the temperature to determine $d_0(T)$. The results are shown as part of the first publication's supplementary information in section P2.7.3.

4.3 Evaluation of diffraction patterns

For the research project that this thesis is part of, around 800 000 diffraction patterns were acquired in total. Naturally, automated data analysis routines had to be developed. A 2D diffraction pattern is essentially a $M \times N$ matrix, where each value corresponds to a photon count or intensity. The columns and rows have to be converted into polar coordinates so that the intensities can be evaluated as a function of the radius and the azimuth, figure 4.6. In this thesis, this coordinate transformation and subsequent analysis was performed using two software (packages): *Fit2D* [Ham98] and *pyFAI* [Ash15].

As a first step, the calibration measurement of a reference LaB_6 diffraction pattern is evaluated, see section 4.1.3. This calibration yields essential parameters for the coordinate transformation to integrate the experimental diffraction patterns afterward. Several parameters are calculated by the software using input parameters such as the pixel size and resolution of the detector, as well as the photon energy:

- The distance between the detector and the sample,
- the rotation of the detector,
- the distortion of the detector,
- and the beam center, which is the location on the detector where the incident X-ray beam meets the detector plane.

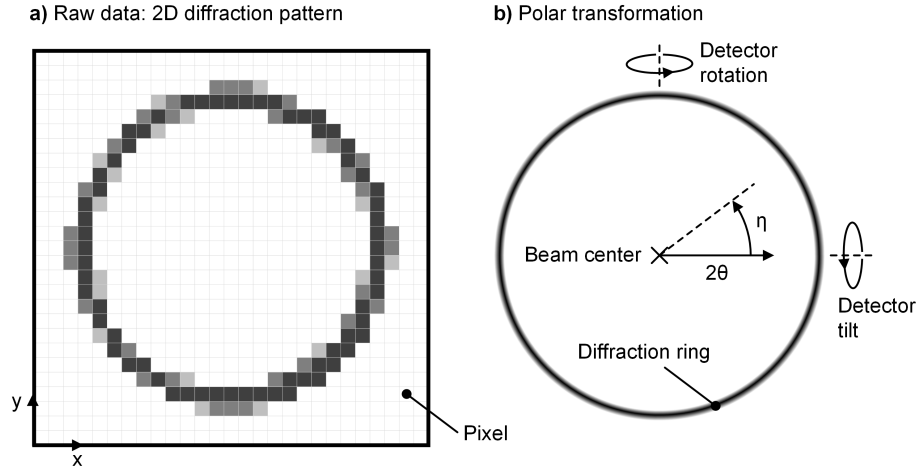


Figure 4.6: Transforming cartesian 2D diffraction patterns to polar coordinates. a) Schematic of raw pixel diffraction data. b) Polar angles in relation to diffraction ring and detector parameters to consider.

Since the lattice spacings of the LaB_6 powder are very well known, the parameters mentioned above can be inferred from its diffraction pattern with high precision, thereby providing the basis for the subsequent integration. The calibration parameters are saved in a specific format to be easily referred to by the utilized software packages afterward.

4.3.1 Azimuthal integration and peak fitting

For this study, azimuthal integration was used, yielding $I(2\theta)$ data for a specific φ range. This type of integration can be performed for the full azimuthal range (*full integration*) or for a set interval (*sector integration*), visualized in figure 4.7a.

The resulting line profile, figure 4.7b, is then split up into the individual peaks. A background correction is performed for each peak individually by linear regression based on ten data points, five on each side next to the peak. The resulting linear function is then subtracted from the peak profile, figure 4.7c. Now, the peak profile is approximated with a PseudoVoigt function using the python library *lmfit* [New14] and a least-squares approximation algorithm.

In addition to the fitting data, the integrated intensity of the peak profile is calculated following the trapezoid rule. In total, the following data is collected and saved for further analyses:

- Peak position 2θ
- Lattice spacing calculated from peak position via equation 2.2
- Full-width half maximum (FWHM)
- Integrated intensity

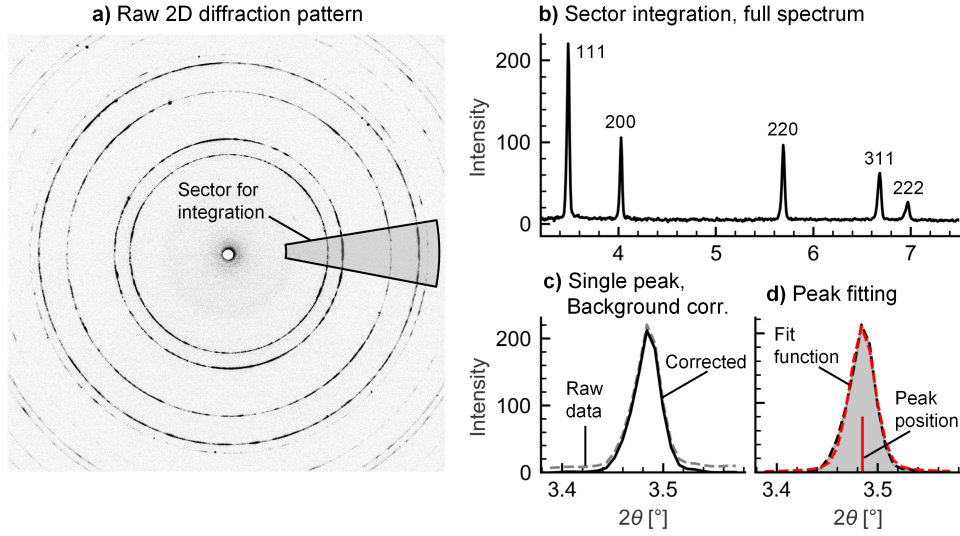


Figure 4.7: Steps of integration and peak analysis. a) Raw diffraction pattern converted to greyscale with a sketch of the sector for integration. b) 1D diffraction profile for highlighted sector. c) Extracted single reflection with corrected background. d) Fitted function to gather peak parameters.

- Maximum intensity
- Correlation coefficient R^2
- Associated errors for peak position, lattice spacing, FWHM

Generally, both full and sector integration were performed for each diffraction pattern. Unless stated differently, a sector size of 5° was chosen, resulting in 72 sectors per diffraction pattern. For Inconel 625, the first five peaks were evaluated, resulting in

$$(72 + 1) \text{ line profiles} \times 5 \text{ peaks} \times 9 \text{ parameters} = 3285 \text{ data points}$$

per diffraction pattern.

4.3.2 Stress calculation

In section 2.1.6.2, the fundamental equation of residual stress analysis was introduced. The application of equation 2.6 necessitates the consideration of the geometrical conditions of the experimental setup in this study to connect the azimuthal lattice spacings to the sample coordinate system.

In this study, the X-ray diffraction experiments were performed in transmission geometry, i. e., the specimen was placed between the incident synchrotron radiation beam and the detector, figure 4.8. Therefore, the entire thickness of the material is irradiated and contributes to the diffraction signal on the detector. This corresponds to a measuring direction of $\psi = 90^\circ$.

4 Experimental methods

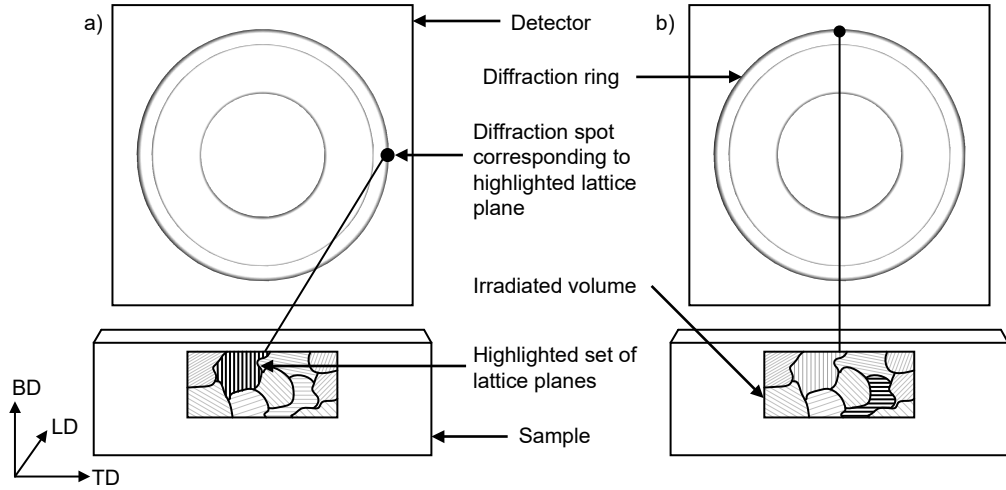


Figure 4.8: Schematic of the relation between diffracting lattice planes and the diffraction spots on the detector. a) case for TD, b) case for BD.

At the same time, full diffraction rings were collected, allowing the analysis of the full azimuthal range for this measuring direction. Therefore, equation 2.6 can be simplified to equation 4.1.

$$\begin{aligned} \varepsilon_{\varphi, \psi=90^\circ} = \frac{1}{2} s_2(hkl) [\sigma_{11} \cos^2 \varphi + \sigma_{22} \sin^2 \varphi + \sigma_{12} \sin 2\varphi] \\ + s_1(hkl) [\sigma_{11} + \sigma_{22} + \sigma_{33}] \end{aligned} \quad (4.1)$$

Considering the two principal directions $\varphi = 0^\circ$ and $\varphi = 90^\circ$, the equations 4.2 and 4.3 illustrate the relation of the measured lattice strains to the internal stresses.

$$\varepsilon_{\varphi=0^\circ, \psi=90^\circ} = \varepsilon_{11} = \frac{1}{2} s_2(hkl) \sigma_{11} + s_1(hkl) [\sigma_{11} + \sigma_{22} + \sigma_{33}] \quad (4.2)$$

$$\varepsilon_{\varphi=90^\circ, \psi=90^\circ} = \varepsilon_{22} = \frac{1}{2} s_2(hkl) \sigma_{22} + s_1(hkl) [\sigma_{11} + \sigma_{22} + \sigma_{33}] \quad (4.3)$$

In this thesis, the laboratory coordinate axes, which correspond to the assumed principal stress directions, are called TD, BD and LD. Therefore, the correlation to the strains and stresses from equations 4.2 and 4.3 is assigned as follows in the set of equations 4.4.

$$\begin{aligned} \varepsilon_{11} &= \varepsilon_{TD}, & \sigma_{11} &= \sigma_{TD} \\ \varepsilon_{22} &= \varepsilon_{BD}, & \sigma_{22} &= \sigma_{BD} \\ \varepsilon_{33} &= \varepsilon_{LD}, & \sigma_{33} &= \sigma_{LD} \end{aligned} \quad (4.4)$$

The diffraction patterns do not contain information regarding the strains in the transmission direction. It is, therefore, not possible to determine the full triaxial stress tensor from a single 2D diffraction pattern. In the second and third publications, chapter P2 and chapter P3, different approaches are presented that tackle this problem.

4.3.3 Texture calculation

The calculation of textures is based on sector integration and the relation of peak intensities and crystal symmetry. For each sector, all five peaks of Inconel 625 that were captured were evaluated as described in section 4.3. The actual texture determination was performed using the *Matlab* software package *MTEX* [Bac10]. A detailed explanation of the procedure is given in chapter P1.

Part II

Publications

In situ Microstructure Analysis of Inconel 625 during Laser Powder Bed Fusion


In the following article, the microstructure development in Inconel 625 parts was evaluated *in situ* during LPBF processing. Comprehensive peak profile analyses revealed the material's response to the initial laser impact, repeated scanning, and variation of processing parameters. To the author's knowledge, this study is the first to observe *in situ* texture changes during LPBF directly. Furthermore, a visualization approach to display temporally resolved texture changes is introduced in this study. Analyses of peak widths and asymmetry reveal other microstructural phenomena such as recrystallization and segregation growth during the initial manufacturing process. After the original article, additional unpublished findings are presented in section P1.8.

Bibliographic data	
Title	In situ Microstructure Analysis of Inconel 625 during Laser Powder Bed Fusion
Authors	Felix Schmeiser, Erwin Krohmer, Christian Wagner, Norbert Schell, Eckart Uhlmann, Walter Reimers
Journal	Journal of Materials Science
Publisher	Springer Nature
Publication Date	8th November 2021
Reference	Journal of Materials Science 57 (2022): 9663-9677
DOI	10.1007/s10853-021-06577-8
My contribution	Planning, executing, and evaluating the <i>in situ</i> LPBF diffraction experiments at PETRA III; Data analysis, interpretation, visualization; Supervising and interpreting the TEM investigations; Writing the manuscript

The manuscript is inserted in the following pages. The article is reprinted under the open access CC BY license (<https://creativecommons.org/licenses/by/4.0/>)



In situ microstructure analysis of Inconel 625 during laser powder bed fusion

Felix Schmeiser^{1,*} , Erwin Krohmer², Christian Wagner¹, Norbert Schell³, Eckart Uhlmann^{2,4}, and Walter Reimers¹

¹Institute for Materials Science and Technology, Metallic Materials, Technische Universität Berlin, Ernst Reuter Platz 1, 10587 Berlin, Germany

²Institute for Machine Tools and Factory Management (IWF), Technische Universität Berlin, Pascalstraße 8-9, 10587 Berlin, Germany

³Helmholtz-Zentrum Hereon, Max-Planck-Str. 1, 21502 Geesthacht, Germany

⁴Fraunhofer Institute for Production Systems and Design Technology (IPK), Pascalstraße 8-9, 10587 Berlin, Germany

Received: 1 July 2021

Accepted: 29 September 2021

Published online:

8 November 2021

© The Author(s) 2021

ABSTRACT

Laser powder bed fusion is an additive manufacturing process that employs highly focused laser radiation for selective melting of a metal powder bed. This process entails a complex heat flow and thermal management that results in characteristic, often highly textured microstructures, which lead to mechanical anisotropy. In this study, high-energy X-ray diffraction experiments were carried out to illuminate the formation and evolution of microstructural features during LPBF. The nickel-base alloy Inconel 625 was used for in situ experiments using a custom LPBF system designed for these investigations. The diffraction patterns yielded results regarding texture, lattice defects, recrystallization, and chemical segregation. A combination of high laser power and scanning speed results in a strong preferred crystallographic orientation, while low laser power and scanning speed showed no clear texture. The observation of a constant gauge volume revealed solid-state texture changes without remelting. They were related to in situ recrystallization processes caused by the repeated laser scanning. After recrystallization, the formation and growth of segregations were deduced from an increasing diffraction peak asymmetry and confirmed by ex situ scanning transmission electron microscopy.

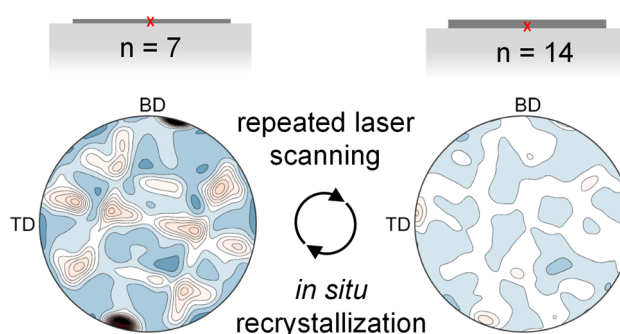
Handling Editor: Sophie Primig.

Address correspondence to E-mail: felix.schmeiser@tu-berlin.de

<https://doi.org/10.1007/s10853-021-06577-8>

 Springer

GRAPHICAL ABSTRACT



Introduction

Additive manufacturing facilitates the fabrication of arbitrarily complex geometries and tailored material properties using a range of different materials. Laser powder bed fusion (LPBF) is a process especially suited for the production of metal parts. LPBF employs focused laser radiation to melt a powder bed selectively. After laser exposure, the material solidifies immediately, and a new powder layer is applied, resulting in the layer-wise fabrication of the desired geometry. The selective and both locally and temporally varying energy input leads to a complex heat flow and temperature distribution, which govern the solidification and grain growth regime. Precise knowledge of the interaction of laser parameters and microstructural response within the workpiece opens up the prospect of tailored microstructure design.

Several properties characterize the microstructure of crystalline material, e.g., phase composition, microscopic defects such as porosity, and nanoscopic crystal lattice defects. Additionally, the grains' size, morphology, and crystallographic orientation severely impact the material's mechanical properties. The entirety of all crystallographic orientations in a polycrystalline material is summarized as its texture.

The texture is often described as the deviation from a random orientation distribution. The texture of a polycrystal is created during processes that define the microstructure, such as solidification and crystallization of a molten mass, recrystallization, and plastic deformation. The texture is determined by factors with a directed impact, such as mechanical

force in plastic deformation or a directed heat flow during solidification [1].

A textured material exhibits anisotropic properties, e.g., Young's modulus, ductility, strength, and hardness. In LPBF, the directed solidification initially determines the texture as the material is exposed with a focused laser beam. The grain growth and the texture in a LPBF manufactured specimen are influenced by the melt pool geometry and the thermal gradients acting in the component [2]. As the melt pool solidifies, grains nucleate at the solidification front. During the subsequent grain growth, grains with different orientations compete [3]. Several studies found that grains with an orientation parallel to the melt pool boundary normal dominate during this phase [2, 4–6]. This preferred orientation results from the heat flow, which has its largest magnitude in the melt pool boundary's normal direction [7]. The preferred orientation is, furthermore, dependent on the crystal lattice. For example, face-centered cubic (fcc) metals such as the nickel-base alloy Inconel 625 grow in the preferred $\langle 100 \rangle$ direction [1].

The melt pool geometry depends on several factors, e.g., thermal conductivity, energy absorption, and heat flow [6, 8]. Gong et al. [9] investigated the influence of different laser powers and scanning speeds on the melt pool geometry. They found that high laser powers and low scanning speeds lead to the keyhole effect. Here, the melt pool shows a broad opening at the top and tapers toward the bottom. The keyhole has a high penetration depth due to the high laser intensity and energy input, resulting in the remelting of previously solidified material.

Furthermore, keyholing leads to undesirable porosity [10]. Contrarily, a combination of low laser power and high scanning speeds leads to the balling effect. If the energy input is insufficient, the layer below will be insufficiently wetted. Spherical melt pools and bead-like structures are formed, which impede the following layers and can disrupt the manufacturing process by jamming the powder recoating mechanism [11].

The energy input also impacts grain growth. Higher laser powers lead to deeper melt pools, lower laser powers to shallower melt pools. In shallower melt pools, the normal vectors on the melt pool boundaries are more parallel than in deeper melt pools. They are parallel to the building direction of the part, therefore resulting in a preferred orientation in the building direction [6]. The melt pools are deeper when using lower scanning speeds or high laser powers, leading to a more significant variation of the melt pool boundary normal directions [4]. Therefore, crystallites do not only grow in the building direction, resulting in a lower preferred orientation [6]. Sun et al. [4] concluded that texture development could be controlled via process control. They successfully built parts from 316L, which showed a $\langle 011 \rangle$ fiber texture instead of the commonly found $\langle 001 \rangle$ for fcc alloys by using an increased laser power and a multi-scan method.

Yin et al. [5] found a dependence between the orientation of grain growth and laser power and scanning speed using FEM simulations for Ti-6Al-V4 processed via LPBF. They concluded that the layer number exerts an influence on the melt pool geometry and, therefore, on the grain orientation. For small layer numbers, the substrate plate strongly influences heat dissipation. Here, the crystal orientations show substantial deviations from the building direction. With increasing layer numbers, the melt pool becomes shallower, and the grain growth changes toward the building direction after a few layers. [5]

Several approaches to tailor the microstructure via process parameter manipulation have been published to date. Roehling et al. [12] adjusted the shape of the laser beam to generate preferable microstructures and mechanical properties. Dehoff et al. [13] showed that tailored, site-specific textures could be designed by varying the process parameters. The typical route is a post-process heat treatment, usually aimed at achieving a recrystallized microstructure [14]. For Inconel 625, Marchese et al. [15] investigated the microstructural

evolution after various heat treatments and found a recrystallized microstructure after a solution heat treatment. Sabzi et al. [16] recently presented the first experimental proof that dynamic recrystallization (DRX) occurs during LPBF as well, using ex situ EBSD measurements and thermomechanical modeling. However, an in situ observation of DRX during LPBF has not been reported yet.

Since DRX impacts the crystallographic texture, high-energy synchrotron radiation diffraction is well-suited for its investigation. In situ diffraction experiments so far have been focused on phase transformations [17], cooling dynamics [18, 19], and internal stresses [20, 21]. Recently, Wahlmann et al. [22] presented results regarding the in situ formation of precipitates, another important constituent of the microstructure, in a nickel-base superalloy using synchrotron radiation diffraction and the LPBF device from the present study's group.

To the authors' knowledge, for LPBF, in situ texture analyses using high-energy synchrotron radiation have not been reported so far. Using a custom-built LPBF machine designed for in situ diffraction measurements, experiments using Inconel 625 were carried out to determine the development of texture and the influence of repeated laser scanning on the microstructure.

Materials and methods

Custom LPBF machine

In previous work, a custom LPBF process chamber was developed and integrated into the modular LPBF machine AconityMINI from Aconity3D GmbH, Herzogenrath, Germany, to realize in situ X-ray diffraction experiments with synchrotron radiation [23]. The custom LPBF machine is equipped with a 400 W Ytterbium fiber laser YLR-400-AC from IPG Laser GmbH, Burbach, Germany. The laser source emits light with a wavelength of 1070 nm in continuous wave. The laser is focused and deflected on the powder bed with an Axialscan-30 from Raylase GmbH, Wessling, Germany, with a focus diameter of ca. 60 μm in $1/e^2$ specification. Before processing, the process chamber was sealed and purged with argon. During the processing, a clean argon atmosphere was maintained by using a filtration unit connected to the process chamber and

coupled to a circulation pump. The powder bed was sandwiched between two glassy carbon windows. Inlet and outlet windows for the synchrotron radiation in the process chamber are made from polyimide foil. An automatic powder recoating mechanism inside the purged process chamber ensured the additive manufacturing of multi-layer parts without interrupting the experiment for manual operations.

Materials

The nickel-base alloy 625, commonly referred to as Inconel 625, was used as powder material and purchased from m4p material solutions GmbH, Magdeburg, Germany. The particles were nitrogen-atomized and exhibited mostly spherical shapes, Fig. 1, with particle sizes ranging from 20 μm to 63 μm , Table 1. The median circularity of the

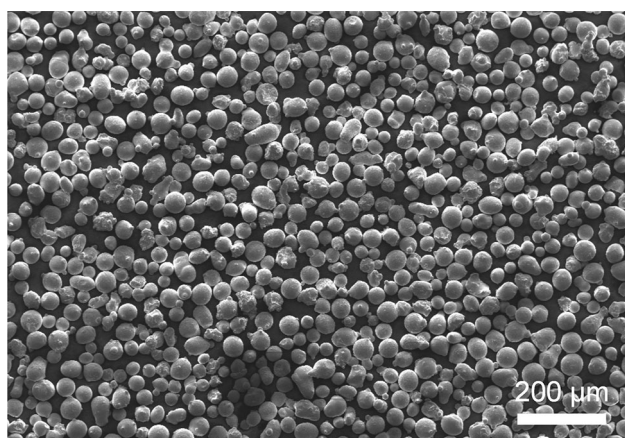


Figure 1 SEM image of Inconel 625 powder.

Table 1 Particle size distribution of Inconel 625 powder per sieve analysis

0–20 μm	20–40 μm	40–50 μm	50–63 μm	+ 63 μm
0.68%	67.64%	29.42%	2.26%	0.0%

Table 2 Parameter sets for the experiments

Parameter unit	Laser power P_L [W]	Scanning speed v_L [mm/s]	Line energy E_L [J/mm]	Scanning pattern	Hatch distance h_L [μm]	Layer thickness Δz [μm]
Set 1	55	50	1.1	Longitudinal	120	50
Set 2	275	760	0.36			

particles, calculated with Eq. 1, was 0.85 with circ = 1 equaling a perfect circle.

$$\text{circ} = 4\pi \times \frac{\text{Area}}{\text{Perimeter}^2}, \quad (1)$$

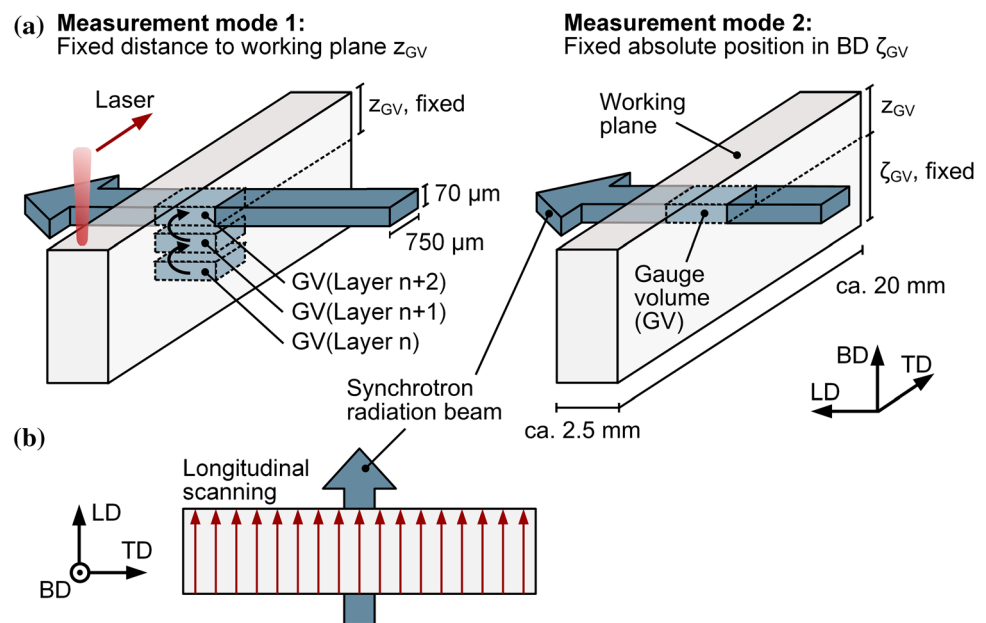
Structural steel S235 plates with a size of 70 \times 20 \times 3 mm³ were used as substrate material.

Process parameters and measurement modes

Two different LPBF parameter sets were investigated, Table 2. They are composed of two pairs of laser power P_L and scanning speed v_L ranging from a low laser power $P_L = 55$ W and low scanning speed $v_L = 50$ mm/s to a high laser power $P_L = 275$ W and a high scanning speed $v_L = 760$ mm/s. The ratio of laser power P_L to scanning speed v_L is denoted as line energy E_L . The scanning pattern featured unidirectional scanning vectors aligned longitudinally to the incident synchrotron radiation beam, Fig. 2. Cuboid samples ca. 20 \times 2.5 \times 5 mm³ in size were produced out of 100 layers with a layer thickness of $\Delta z = 50$ μm . Laser scanning was set to start at the left edge and finish at the right edge of the sample geometry. Two different measurement modes were used. In measurement mode 1 (MM1), the gauge volume (GV) distance to the working plane, z_{GV} , is kept constant throughout the measurement of all the 100 layers. In measurement mode 2 (MM2), the absolute gauge volume position in the sample is maintained such that a defined volume element of the sample, defined by its distance to the sample-substrate interface, ζ_{GV} , is tracked throughout the process.

In this study, the axis parallel to the incident synchrotron radiation beam is called longitudinal direction (LD), which spans the working plane together with the transverse direction (TD). The third axis is parallel to the part height and called the building direction (BD).

Figure 2 Experimental procedure: **a** Measurement modes and gauge volume positioning; **b** Laser scanning pattern.



Experimental procedure

In situ diffraction experiments were carried out at PETRA III, Deutsches Elektronen-Synchrotron (DESY) in Hamburg, Germany. The High Energy Materials Science (HEMS) beamline P07 [24], which is operated by Helmholtz-Zentrum Hereon, features a heavy load 6-axis positioning system on which the process chamber of the custom LPBF machine was mounted. A PerkinElmer XRD1621 area detector was used for diffraction pattern acquisition. For the diffraction experiments, synchrotron radiation energies of 87 and 98 keV were used. The synchrotron radiation beam size was set to 750 μm in TD and 70 μm in BD, Fig. 2.

The diffraction patterns were acquired with an exposure time $t = 0.1$ s and frequency $f = 10$ Hz. Patterns were collected as layer-wise image series when the laser emission was active. The series measurement started with the laser being turned on and ended at the end of laser scanning. Therefore, not the whole cooling process after the laser impact was observed.

To complement the in situ diffraction experiments, two specimens were analyzed after production using standard metallographic preparation methods. For both parameter sets, the TD-BD plane was polished and etched in a solution of 1.5 ml hydrogen peroxide and 50 ml hydrochloric acid for $t = 45$ s. This preparation emphasized grain structures and melt

pool boundaries in the subsequent optical microscopy using a Zeiss Axioskop 50.

Additionally, one sample, manufactured using $P_L = 55$ W, was investigated by scanning transmission electron microscopy (STEM) at Zentraleinrichtung Elektronenmikroskopie (ZELMI) of Technische Universität Berlin. The specimen was cut using a focused ion beam on a FEI Helios Nanolab 600 FIB to ensure that the subsequent STEM analysis probed the same gauge volume as the in situ diffraction experiments in MM2. The investigations were carried out using a JEOL JEM-ARM300F2 STEM with a cold field emission gun and a probe-Cs corrector operating at an acceleration voltage of 300 kV and equipped with a JEOL Dual-EDX system using two 160 mm² SDD detectors. High-angular annular dark-field images (HAADF) were acquired because of their high sensitivity to the atomic number of the probed material.

Data evaluation

The detector calibration and integration were performed using the Python library pyFAI [25], pole figures were generated using MTEX [26]. The detector calibration was performed using a standard LaB6 powder sample to determine the detector-sample distance and the detector tilt for accurate integration results. Subsequently, the diffraction patterns were integrated in 5° sectors, resulting in 72 line profiles, including the first five hkl reflections for each

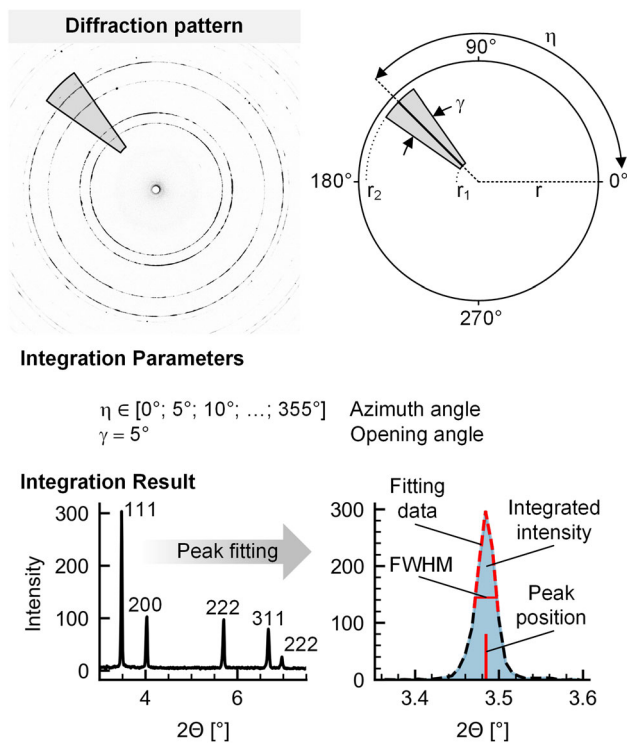


Figure 3 Data evaluation procedure from sector integration to peak fitting.

diffraction pattern, Fig. 3. For each reflection, background subtraction was performed. Then, the integrated intensity was calculated following the trapezoid rule.

Additionally, the peak position was determined by fitting the line profile with a PseudoVoigt function using the python library LMFIT [27]. This fitting function also yielded the full width at half maximum (FWHM) of the reflections. For the fitting, only the top 60% of each peak were considered due to a slight asymmetry of the profiles, further discussed in Sect. 3.3. The peak positions and integrated intensities were converted to a format readable by MTEX to calculate the orientation distribution function (ODF), which was then plotted as a pole figure. This procedure was derived from Wenk and Grigull [28].

Representative results gathered from in situ experiments illustrate the evolution of microstructural features during LPBF. The data is presented based on two visualization styles. Pole figures represent the standard method of conveying texture. They show a color-coded intensity distribution as multiples of a random distribution (MRD). Each pole figure is calculated considering both the intensity and symmetry of the first five hkl reflections. The

colormap chosen for plotting the pole figures emphasizes deviations from a random distribution, which would equal no preferred orientation. In this work, pole figures are used to visualize single texture states.

Temporally resolved texture evolution is visualized by time-dependent integrated intensity distributions, which are called processing plots in this study. These distributions show the azimuthal intensity for the (111) and (200) reflections. This way, local changes in the intensity distribution over time are visible. These visualizations do not contain the same amount of information as pole figure plots, though, which is why they are used complementarily.

Results

Impact of laser irradiation on texture

In Fig. 4, the impact of the laser scanning over the gauge volume is shown for two different energy inputs, denoted by the different laser powers P_L . For both laser powers, the changes in texture are documented for a single layer. Pole figures are given for the initial state, before laser impact, and the final state, at the end of the laser scanning time. Additionally, time-resolved intensity changes are made visible through the processing plots. Here, azimuths of 0° , 180° , and 360° correspond to TD, while 90° and 270° correspond to BD. In both measurements, the gauge volume was positioned at $z_{GV} = 150 \mu\text{m}$ below the top surface of the part. The azimuthal intensities for the (111) and (200) reflections were normalized for each sample since the respective experiments were conducted with varying incident beam intensities and energies.

The 275 W sample showed an intensification of the orientation distribution after the laser has passed over the gauge volume. The same parallel lines persist, with the intensities being much higher after the laser peak. The pole figures confirm this observation. The (200) pole figure shows an intensification of texture as the maximum MRD value increases. The local intensity maxima around BD are much more pronounced in the final state than the initial state. Similar textures were found in other build heights as well, Fig. 5, showing that this parameter set leads to a homogeneous texture in the part.

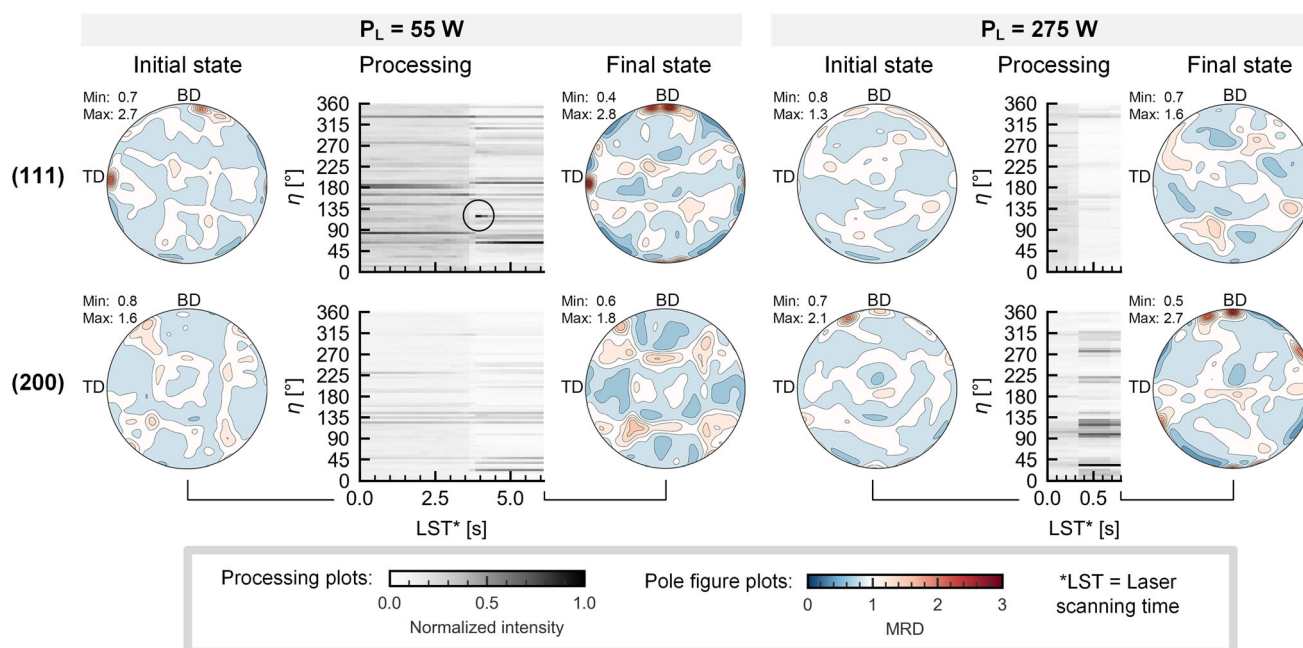


Figure 4 Comparison of the influence of different energy inputs on texture: Intensity distribution throughout a single layer in MM1 for $n = 50$, $z_{GV} = 150 \mu\text{m}$. Circled area in processing plot for $P_L = 55 \text{ W}$ shows high intensity that rapidly decreases after laser impact.

The 55 W sample, on the other hand, shows a different orientation distribution after the laser impact compared to before. Initially, the highest intensities were found for the (111) reflection in both TD and BD. As the laser scans over the gauge volume, a high-intensity spot appears at 120° , which fades quickly. The intensity line in BD shifts toward 45° , while the one at 180° is shifted to a larger azimuth angle. The (200) reflection shows lower intensities than the (111) reflection with less distinctive features, except for intensity lines emerging between 20° and 45° after laser impact. The (200) pole figures change drastically from the initial to the final state, reflecting the (200) reflection's response to a (111) fiber texture. In the (111) pole figure, a spot at TD is visible in both the initial and final states, while a slightly inclined spot from BD appears to shift counterclockwise in the final state.

In Fig. 6, optical micrographs of the part-substrate interface regions of both samples are shown. This section was chosen because of the clarity of the melt pool boundaries. The low laser power and high line energy result in clearly deeper melt pools than the higher laser power, which features broader and shallower melt pools. The higher laser power shows columnar grains parallel to BD, which surpass the

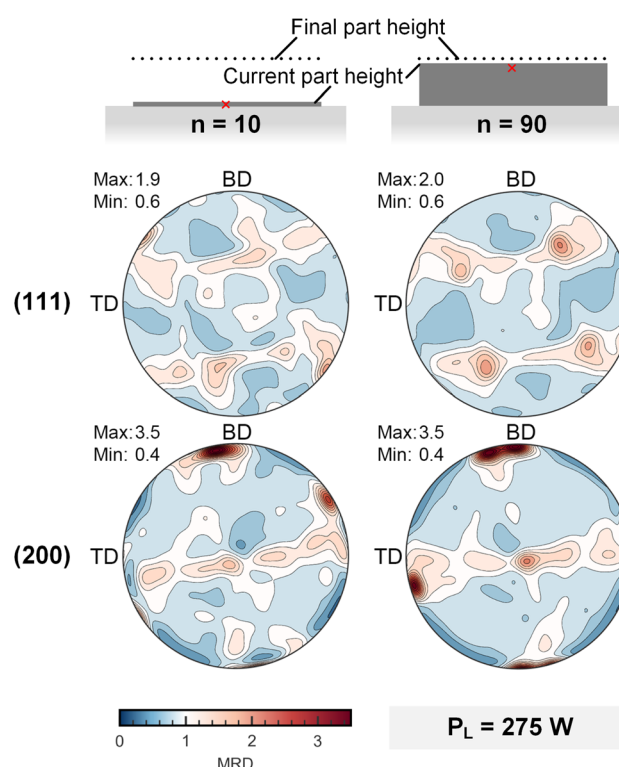


Figure 5 Final state texture in different build heights within a sample manufactured with a laser power of $P_L = 275 \text{ W}$ and observed in MM1 at $z_{GV} = 150 \mu\text{m}$.

Figure 6 Ex situ micrographs of the interface region of part and substrate for both parameter sets.

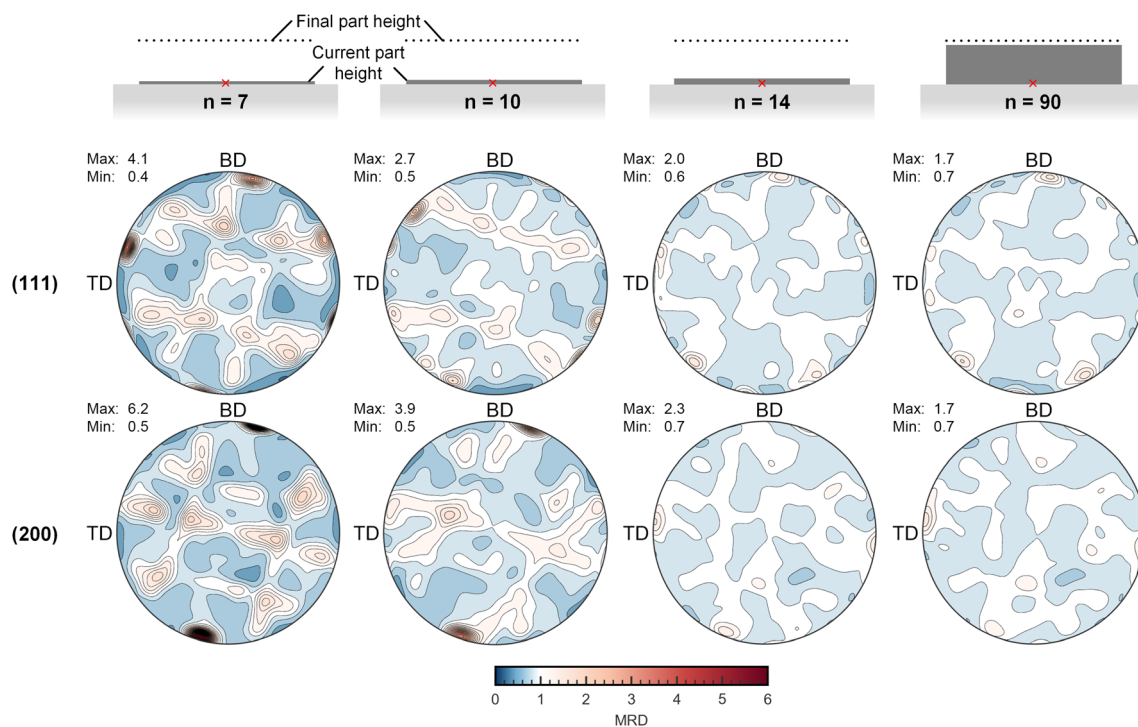
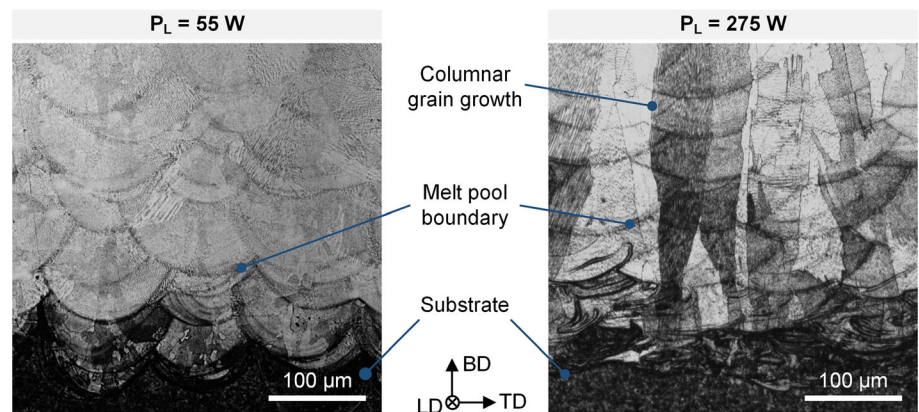


Figure 7 Texture evolution with repeated laser passes over the gauge volume within a sample manufactured with a laser power of $P_L = 55$ W and observed in MM2 at $\zeta_{GV} = 250$ μm .

melt pool boundaries. The grains visible in the micrographs are larger for the high laser power than for the low laser power, where the grain morphology appears less oriented.

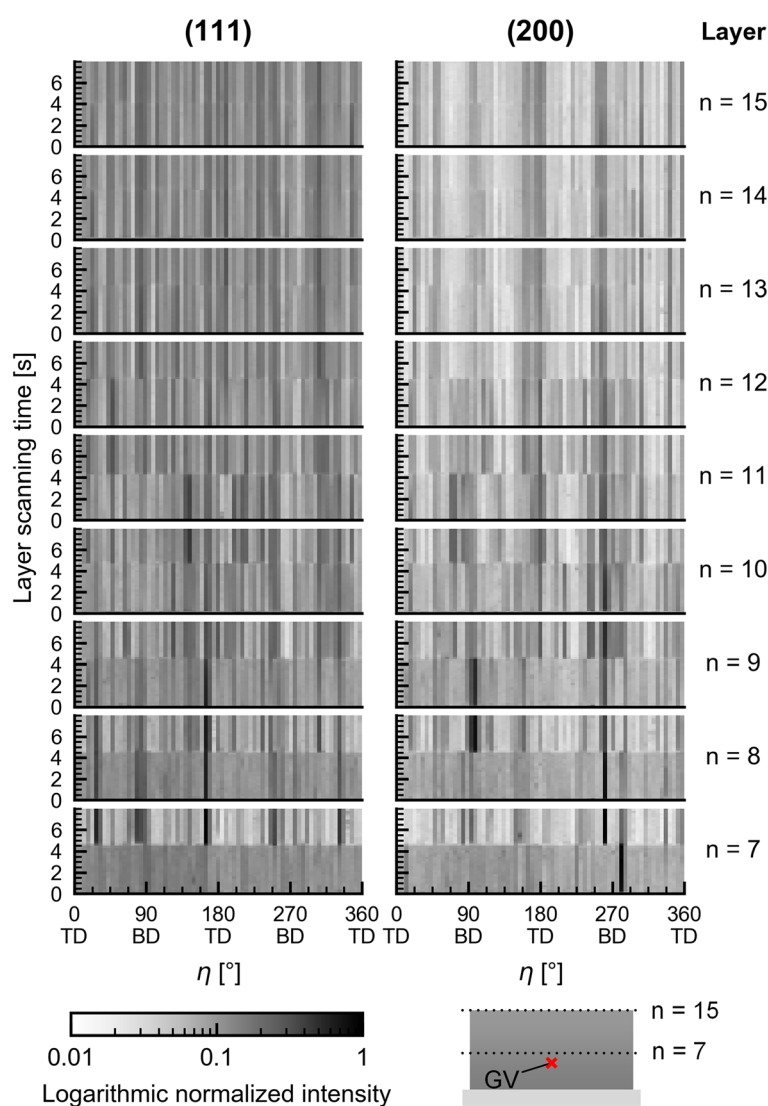
Impact of repeated laser scans on texture

Another phenomenon appears when observing a constant gauge volume throughout the whole process. Figure 7 shows pole figures of the same gauge volume at increasing numbers of total layers. Each

pole figure represents the final state after laser scanning, similar to Fig. 4. The gauge volume was located in the center of the fifth layer of the sample at $\zeta_{GV} = 250$ μm . For each pole figure set, the total number of layers is given below the estimated total part height at that moment. For $n = 7$, consequently, two additional layers of solidified material were above the gauge volume, five layers for $n = 10$ et cetera.

Initially, a bimodal fiber texture is observed at $n = 7$. The (200) plane shows a strong preferred

Figure 8 Sample manufactured with a laser power of $P_L = 55$ W and observed in MM2 at $\zeta_{GV} = 250$ μm : Processing plots for (111) and (200) reflections.



orientation in building direction with a slight inclination. Lower intensity ribbons along the TD plane indicate a (200) fiber texture. Simultaneously, the (111) pole figure shows a fiber texture, too, with the fiber axis slightly tilted from the equatorial plane TD.

At $n = 10$, five layers have been exposed atop the gauge volume, equaling five additional laser passages and about 250 μm of solidified material above. Here, the (111) fiber texture seems to have almost completely vanished, while the (200) fiber texture is still visible and pronounced. Still, the maximum intensity is significantly reduced compared to $n = 7$. At $n = 14$, the intensities are further reduced. The (111) pole figure has completely changed compared to its initial state at $n = 7$, and the fiber texture for the (200) plane is further weakened, signified by a

maximum intensity of only 2.4 compared to 6.2 for the first pole figure.

In Fig. 8, the changes in the intensity distributions are temporally resolved. The azimuthal intensity distribution for the (111) and (200) reflections are shown layer by layer from $n = 7$ to $n = 15$. A logarithmic intensity scale was used to unveil all intensity changes in an extensive range for this figure.

The laser passage over the gauge volume is visible in each plot, signified by a slight intensity change at about $t = 4$ s. As more material is deposited above the gauge volume, this effect gets weaker. At $n = 7$, the initial (111) texture seen in the corresponding pole figure in Fig. 7 is created. Before the laser impact, the intensity distribution appears homogeneous. Afterward, five significant lines emerge,

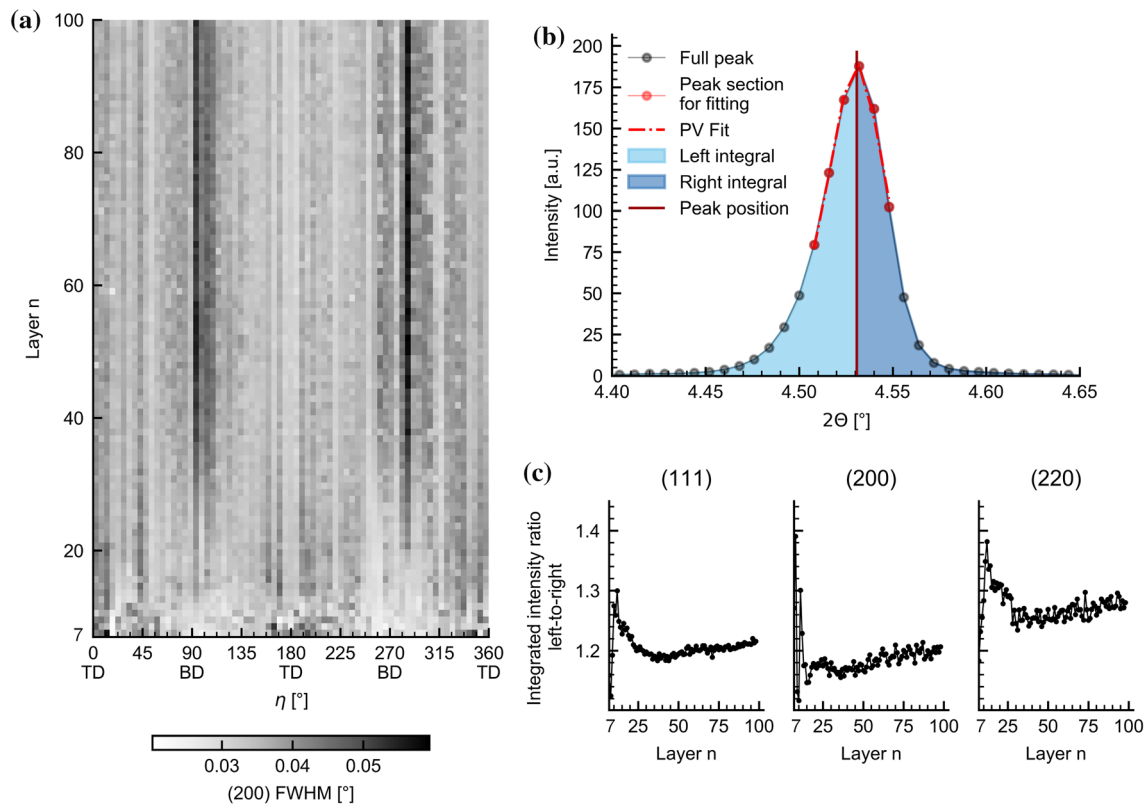


Figure 9 Sample manufactured with a laser power of $P_L = 55$ W and observed in MM2 at $\zeta_{GV} = 250$ μm : **a** Azimuthal (200) FWHM distribution at the end of each layer; **b** Peak shape analysis and fitting parameters; **c** Peak skewness parameter for first three hkl reflections.

which persist until the laser impact at $n = 9$. The (200) reflection shows changes in the intensity distribution as well. Initially, there is a slight shift of a prominent intensity at 270° to about 255° . This line persists up to $n = 15$ and further onwards. After $n = 14$, no further changes in either intensity distribution were observed, which mirrors the findings from the pole figures in Fig. 7.

Repeated laser scanning distorts peak shape

Further analysis of the peak shape was carried out to evaluate possible solid-state phenomena occurring during LPBF. Initially, the FWHM was determined as described in Sect. 2.5, as shown in Fig. 9b.

The azimuthally resolved results are shown in Fig. 9a. Each horizontal line corresponds to the azimuthal distribution of the (200) reflection's FWHM at the end of the corresponding layer. Up to layer $n = 10$, the image appears relatively undefined with changing distributions layer by layer. At this stage, the LPBF process has likely not reached a steady-state concerning the deposited and solidified layer

thickness [29]. Generally, the FWHM values appear higher for TD than for BD in this region, though.

After $n = 20$, two prominent lines emerge at around 90° and 270° , corresponding to increased peak widths in the building direction. Finally, between $n = 30$ and $n = 40$, these lines reach their maximum, with the rest of the distribution not changing anymore. This increase was further evaluated since the amount of material of about 1.25 to 1.5 mm between the gauge volume and the laser-impacted powder layer seemed significant, and the intensity distributions shown in the previous chapter stayed unchanged at these layer numbers.

The peak shape was determined to be one possible factor to distort the FWHM value. The measured peak profiles are slightly asymmetrical with a less steep left side. If this asymmetry were to increase over time, it would impact the FWHM value. The integrated intensity was divided into two sections to evaluate the asymmetry: left of the peak position and right of the peak position. As mentioned before, the peak position was determined via a PseudoVoigt fit of the top 60% of the peak, where the impact of

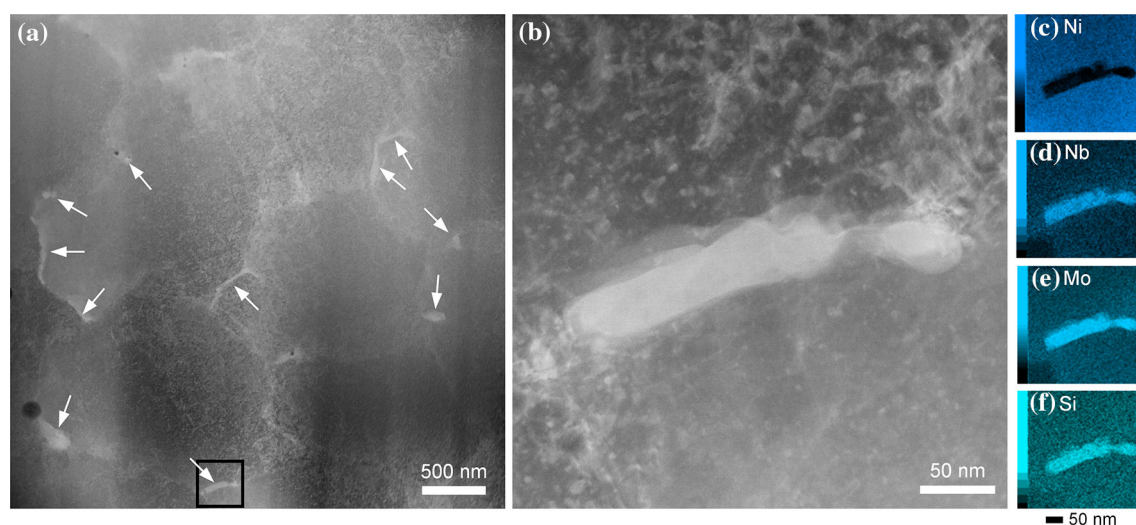


Figure 10 High-angular annular dark-field images acquired by STEM with brighter areas corresponding to higher atomic numbers: **a** Overview image where white arrows indicate Nb

and Mo-rich areas; **b** Close-up of framed area in overview image; **c–f** STEM-EDX maps for nickel, niobium, molybdenum, and silicon.

asymmetry is negligible. Therefore, the left and right-side integrals were calculated separately. The ratio of left-to-right was used as an asymmetry factor. Its evolution over time is shown in Fig. 9c for the first three hkl reflections (111), (200), and (220). The remaining two collected reflections (311) and (222) showed similar behavior.

After an initial fluctuation, the ratio reaches a local minimum between $n = 20$ and $n = 25$ depending on the reflection, after which it slowly increases linearly. Therefore, the peaks become more asymmetrical over time, all while the material stays in a solid state, and the impact of the laser on the gauge volume is expected to be reduced as the amount of material between gauge volume and top layer increases. It was therefore concluded that the asymmetry was not the deciding factor behind the FWHM increase described above.

Ex situ microstructure analysis

The influence of repeated laser scanning on the microstructure was further evaluated using high-resolution scanning transmission electron microscopy (STEM). The sample using $P_L = 55$ W observed in MM2 was investigated in the region where the synchrotron gauge volume was located. A high-angular annular dark-field image detector was used due to its high sensitivity to the atomic number and the resulting Z contrast. Atoms with a higher atomic number appear brighter in the resulting image. The

overview in Fig. 10a shows an inhomogeneous microstructure with a lot of contrast. Several bright features with a size of 100–300 nm in the interdendritic regions stand out. Energy-dispersive X-ray spectroscopy (EDX) images in Fig. 10c–f reveal that these segregations have high Nb and Mo as well as Si contents.

Discussion

Influence of energy input

As described in the introduction, the energy input is one of the deciding factors for forming preferred orientations in the material. In this study, the parameter set with the lower laser power of $P_L = 55$ W had the higher energy input with a line energy of $E_L = 1.1$ J/mm compared to a line energy of $E_L = 0.36$ J/mm for the parameter set with the higher laser power of $P_L = 275$ W. Generally, higher energy inputs result in deeper melt pools and less textured material, which was confirmed in the present study [4].

The high laser power parameter set showed a (200) fiber texture along the building direction regardless of build height and layer number, while the low laser power did not result in a significant preferred orientation. The parameter set with a line energy of $E_L = 0.36$ J/mm resulted in shallower melt pools, therefore, more parallel grain growth directions. As a

result, crystallites grow epitaxially, signified by the intensification of existing orientations and the columnar grain growth transcending the melt pool boundaries.

The parameter set with a line energy of $E_L = 1.1$ J/mm leads to deeper melt pools and a reduced preferred orientation. The changes in the intensity distribution during laser scanning imply a certain depth of the heat-affected zone that enables orientation changes. The single intensity spot visible only for a short period during laser scanning, annotated in Fig. 4, indicates the consumption of grains during grain growth.

In situ recrystallization stage

The measurements in a constant gauge volume revealed significant changes in the intensity distribution in solidified material, which coincide with a reduction in texture. The texture changes from a strong bimodal (200) fiber texture in BD and (111) fiber texture in TD to a significantly reduced preferred orientation, where only a weak impression of the (200) fiber texture remains. These changes occur between $n = 7$ and $n = 14$, with 100 μm to 450 μm of material between the gauge volume and the top layer exposed by the laser. After the total number of layers has reached $n = 14$, no more intensity changes are observed.

The focused laser beam and its highly localized energy input, together with the extremely high heating and cooling rates, lead to lattice defects such as dislocations in LPBF [30]. The high defect density and the thermal cycling, combined with the fact that the material stayed in a solid state for the whole observation period, lead to the conclusion that DRX is the cause for the observed texture changes. While recovery, which is characterized by reducing lattice defects, results in a reduction in the FWHM, DRX leads to reformation of the microstructure, which results in the changes in the pole figures observed together with the reduction in the FWHM. These findings prove that the repeated laser scanning acts as an in situ heat treatment, which could be used to manipulate and tailor the resulting microstructure of the final part.

In situ segregation stage

In Sect. 3.3, a peak shape analysis was carried out. Anisotropic changes in the FWHM were observed.

An initial reduction in the FWHM coincided with texture changes, further supporting the DRX hypothesis discussed in the previous section. The peak width is influenced by several factors: temperature, domain size, microstrains, defect density.

Temperature can be excluded as a cause since it would impact the whole diffraction pattern, i.e., the whole azimuthal range equally. Domain size is inversely proportional to the peak width, and smaller domains lead to broader peaks. A decrease in domain size is possible during recrystallization, but after the initial microstructural changes, repeated laser scans are expected to lead to grain growth and, therefore, an increased domain size, resulting in a smaller FWHM. It is unlikely that there is a grain size reduction in BD at later stages in the process.

Defect density and microstrains are correlated. Defects such as stacking faults, dislocations, and subgrain boundaries exert a stress field, which leads to microstrains. In this case, the initial reduction in FWHM corresponds to the annihilation of lattice defects due to recovery and DRX. The increase in later stages could be attributed to an increase in microstrains. Due to the increased FWHM values in BD, higher strains and defect concentrations are expected in this direction. As mentioned in the results section, the FWHM values appear to stay constant starting from $n = 40$, implying that no new defects are generated from hereon.

Additionally, the peak asymmetry was evaluated. In an earlier study [20], this asymmetry was attributed to powder material irradiated simultaneously with the solidified material. However, the changes in asymmetry observed in the present study indicate that this is not actually the case. Instead, the increase in asymmetry implies a change in the phase composition of the material.

On one hand, Inconel 625 forms coherent precipitates after heat treatment [15]. Sarkar et al. [31] reported that these precipitates show diffracted peaks overlapping to the matrix. Especially the γ'' phase leads to a peak shape also found in the present study. It is difficult to extract the exact contribution of the precipitates, which is why their presence is often analyzed via changes of the matrix peak as described by Rai et al. [32]. The γ'' phase forms a small peak that contributes to the left-sided asymmetry presented in Sect. 3.3.

On the other hand, Nb and Mo segregation is a known phenomenon for Inconel 625 processed via

LPBF [15], especially in the as-built state. Chemical inhomogeneities of any kind, including segregations, will impact the diffraction peak shape because they change the lattice spacing in the gauge volume. Nb and Mo-rich areas, found in the ex situ TEM investigations, have a different lattice spacing compared to regions with the nominal chemical composition, which will also induce an asymmetry in the diffraction peak.

Therefore, the increase in asymmetry that was observed indicates an increase in segregation concentration. The repeated laser scanning apparently promotes the growth of segregations in situ. This is an interesting and new finding since the impact of the laser on the gauge volume is expected to be reduced with an increasing number of layers. From these results, it appears that the energy input is high enough to promote the growth of segregations until the very end of the process, where there are more than 4.5 mm of material between the powder layer and the gauge volume. The TEM results clearly show Nb and Mo segregations, thereby supporting the hypothesis that the segregation growth is depicted by the in situ diffraction experiments.

Conclusions

This study shows that in situ diffraction experiments are a viable tool for texture analysis during laser powder bed fusion. Several factors impact the formation and evolution of texture. The energy input plays a significant role in the texture in the part. A combination of high laser power and scanning speed, but with a lower line energy E_L , results in a stronger preferred orientation than low laser power and scanning speed with a higher line energy E_L .

Additionally, the observation of a constant gauge volume revealed the impact of repeated laser scanning and the heat-affected zone on the microstructure. Significant texture changes were found during laser scanning up to a distance of ten layers below the working plane. The preferred orientation was strongly reduced. This texture change is attributed to recrystallization since the material stays in a solid state during this observation period. The present study is the first to experimentally observe this phenomenon in situ to the authors' knowledge. After the recrystallization stage, further microstructural changes occur. Apparently, lattice defects reappear after

an initial reduction during recrystallization with a prominent preference for the building direction. This insight was gathered from an analysis of the diffraction peak FWHM. After a total number of 40 layers, no further changes of the FWHM occurred, but the peak shape still changed. Evaluating the peak asymmetry revealed an increase in an underlying contribution to the individual hkl reflections. This underlying contribution is related to the formation and growth of segregations, which was confirmed via ex situ TEM investigations. The peak asymmetry increases up to the end of the observation period at $n = 100$ layers, which underlines the impact of the repeated laser scanning during the segregation stage.

The results presented in this study contribute to the understanding of microstructure formation in LPBF. The in situ observations of recrystallization and segregation formation emphasize the complexity of thermal management during LPBF and highlight the relevance and capabilities of high-energy synchrotron radiation diffraction experiments to advance the fundamental process understanding. Further investigations are necessary to fully understand the influence of process parameters on the microstructure and facilitate a targeted microstructure design during the process.

Acknowledgements

The authors acknowledge the Deutsche Forschungsgemeinschaft (DFG) for funding research project No. 317078200. In addition, they acknowledge Helmholtz-Zentrum Hereon for the provision of laboratory facilities and support during the in situ diffraction experiments. Sören Selve and Christian Günther from Zentraleinrichtung Elektronenmikroskopie (ZELMI) and Anton Thiel from the department of Metallic Materials, all from Technische Universität Berlin, are acknowledged for conducting the STEM investigations and necessary sample preparation. The STEM device is funded by DFG (No. 403371556).

Funding

Open Access funding enabled and organized by Projekt DEAL. This study was funded by Deutsche Forschungsgemeinschaft (project No. 317078200).

Declarations

Conflict of interest The authors declare that they have no conflict of interest.

Open Access This article is licensed under a Creative Commons Attribution 4.0 International License, which permits use, sharing, adaptation, distribution and reproduction in any medium or format, as long as you give appropriate credit to the original author(s) and the source, provide a link to the Creative Commons licence, and indicate if changes were made. The images or other third party material in this article are included in the article's Creative Commons licence, unless indicated otherwise in a credit line to the material. If material is not included in the article's Creative Commons licence and your intended use is not permitted by statutory regulation or exceeds the permitted use, you will need to obtain permission directly from the copyright holder. To view a copy of this licence, visit <http://creativecommons.org/licenses/by/4.0/>.

References

- [1] Wassermann G, Grewen J (1962) *Texturen metallischer Werkstoffe*, 2nd edn. Springer, Berlin Heidelberg
- [2] Wang Y, Yu C, Xing L, Li K, Chen J, Liu W, Ma J, Shen Z (2020) Grain structure and texture of the SLM single track. *J Mater Process Technol.* <https://doi.org/10.1016/j.jmatprotec.2020.116591>
- [3] Wei HL, Elmer JW, DebRoy T (2016) Origin of grain orientation during solidification of an aluminum alloy. *Acta Mater.* <https://doi.org/10.1016/j.actamat.2016.05.057>
- [4] Sun Z, Tan X, Tor SB, Chua CK (2018) Simultaneously enhanced strength and ductility for 3D-printed stainless steel 316L by selective laser melting. *NPG Asia Mater.* <https://doi.org/10.1038/s41427-018-0018-5>
- [5] Yin J, Peng G, Chen C, Yang J, Zhu H, Ke L, Wang Z, Wang D, Ma M, Wang G, Zeng X (2018) Thermal behavior and grain growth orientation during selective laser melting of Ti-6Al-4V alloy. *J Mater Process Technol.* <https://doi.org/10.1016/j.jmatprotec.2018.04.035>
- [6] Wang Di, Song C, Yang Y, Bai Y (2016) Investigation of crystal growth mechanism during selective laser melting and mechanical property characterization of 316L stainless steel parts. *Mater Des.* <https://doi.org/10.1016/j.matdes.2016.03.111>
- [7] Wang Z, Guan K, Gao M, Li X, Chen X, Zeng X (2012) The microstructure and mechanical properties of deposited-IN718 by selective laser melting. *J Alloy Compd.* <https://doi.org/10.1016/j.jallcom.2011.10.107>
- [8] Zhang D, Zhang P, Liu Z, Feng Z, Wang C, Guo Y (2018) Thermofluid field of molten pool and its effects during selective laser melting (SLM) of Inconel 718 alloy. *Addit Manuf.* <https://doi.org/10.1016/j.addma.2018.03.031>
- [9] Gong H, Gu H, Zeng K, Dilip J, Pal D, Stucker B, Christiansen D, Beuth J, Lewandowski JJ (2014) In: *Proceedings of the 25th Solid Freeform Fabrication Symposium*, pp 256–267
- [10] King WE, Barth HD, Castillo VM, Gallegos GF, Gibbs JW, Hahn DE, Kamath C, Rubenchik AM (2014) Observation of keyhole-mode laser melting in laser powder-bed fusion additive manufacturing. *J Mater Process Technol.* <https://doi.org/10.1016/j.jmatprotec.2014.06.005>
- [11] Yap CY, Chua CK, Dong ZL, Liu ZH, Zhang DQ, Loh LE, Sing SL (2015) Review of selective laser melting: materials and applications. *Appl Phys Rev.* <https://doi.org/10.1063/1.4935926>
- [12] Roehling TT, Shi R, Khairallah SA, Roehling JD, Guss GM, McKeown JT, Matthews MJ (2020) Controlling grain nucleation and morphology by laser beam shaping in metal additive manufacturing. *Mater Des.* <https://doi.org/10.1016/j.matdes.2020.109071>
- [13] Dehoff RR, Kirka MM, Sames WJ, Bilheux H, Tremsin AS, Lowe LE, Babu SS (2015) Site specific control of crystallographic grain orientation through electron beam additive manufacturing. *Mater Sci Technol.* <https://doi.org/10.1179/1743284714Y.0000000734>
- [14] Sames WJ, List FA, Pannala S, Dehoff RR, Babu SS (2016) The metallurgy and processing science of metal additive manufacturing. *Int Mater Rev.* <https://doi.org/10.1080/09506608.2015.1116649>
- [15] Marchese G, Lorusso M, Parizia S, Bassini E, Lee J-W, Calignano F, Manfredi D, Terner M, Hong H-U, Ugues D, Lombardi M, Biamino S (2018) Influence of heat treatments on microstructure evolution and mechanical properties of Inconel 625 processed by laser powder bed fusion. *Mater Sci Eng A.* <https://doi.org/10.1016/j.msea.2018.05.044>
- [16] Sabzi HE, Aboulkhair NT, Liang X, Li X-H, Simonelli M, Fu H, Rivera-Díaz-del-Castillo PE (2020) Grain refinement in laser powder bed fusion: The influence of dynamic recrystallization and recovery. *Mater Des.* <https://doi.org/10.1016/j.matdes.2020.109181>
- [17] Hocine S, van Swygenhoven H, van Petegem S, Chang CST, Maimaitiyili T, Tinti G, Ferreira Sanchez D, Grolimund D, Casati N (2020) Operando X-ray diffraction during laser 3D printing. *Mater Today.* <https://doi.org/10.1016/j.mattod.2019.10.001>

- [18] Zhao C, Fezzaa K, Cunningham RW, Wen H, de Carlo F, Chen L, Rollett AD, Sun T (2017) Real-time monitoring of laser powder bed fusion process using high-speed X-ray imaging and diffraction. *Sci Rep*. <https://doi.org/10.1038/s41598-017-03761-2>
- [19] Calta NP, Thampy V, Lee DR, Martin AA, Ganeriwala R, Wang J, Depond PJ, Roehling TT, Fong AY, Kiss AM, Tassone CJ, Stone KH, Nelson Weker J, Toney MF, van Buuren AW, Matthews MJ (2020) Cooling dynamics of two titanium alloys during laser powder bed fusion probed with in situ X-ray imaging and diffraction. *Mater Des*. <https://doi.org/10.1016/j.matdes.2020.108987>
- [20] Schmeiser F, Krohmer E, Schell N, Uhlmann E, Reimers W (2020) Experimental observation of stress formation during selective laser melting using in situ X-ray diffraction. *Addit Manuf*. <https://doi.org/10.1016/j.addma.2019.101028>
- [21] Schmeiser F, Krohmer E, Schell N, Uhlmann E, Reimers W (2021) Internal Stress evolution and subsurface phase transformation in titanium parts manufactured by laser powder bed fusion – an in situ x-ray diffraction study. *Adv Eng Mater*. <https://doi.org/10.1002/adem.202001502>
- [22] Wahlmann B, Krohmer E, Breuning C, Schell N, Staron P, Uhlmann E, Körner C (2021) In situ observation of γ' phase transformation dynamics during selective laser melting of CMSX-4. *Adv Eng Mater*. <https://doi.org/10.1002/adem.202100112>
- [23] Uhlmann E, Krohmer E, Schmeiser F, Schell N, Reimers W (2020) A laser powder bed fusion system for in situ x-ray diffraction with high-energy synchrotron radiation. *Rev Sci Instrum*. <https://doi.org/10.1063/1.5143766>
- [24] Schell N, King A, Beckmann F, Fischer T, Müller M, Schreyer A (2013) The high energy materials science beamline (HEMS) at PETRA III. *MSF*. <https://doi.org/10.4028/www.scientific.net/MSF.772.57>
- [25] Ashiotis G, Deschildre A, Nawaz Z, Wright JP, Karkoulis D, Picca FE, Kieffer J (2015) The fast azimuthal integration Python library: pyFAI. *J Appl Crystallogr*. <https://doi.org/10.1107/S1600576715004306>
- [26] Bachmann F, Hielscher R, Schaeben H (2010) Texture analysis with MTEX – free and open source software toolbox. *SSP*. <https://doi.org/10.4028/www.scientific.net/SSP.160.63>
- [27] Newville M, Stensitzki T, Allen DB, Ingargiola A (2014) LMFIT: Non-Linear Least-Square Minimization and Curve-Fitting for Python. Zenodo
- [28] Wenk H-R, Grigull S (2003) Synchrotron texture analysis with area detectors. *J Appl Crystallogr*. <https://doi.org/10.1107/S0021889803010136>
- [29] Bidare P, Maier R, Beck RJ, Shephard JD, Moore AJ (2017) An open-architecture metal powder bed fusion system for in-situ process measurements. *Addit Manuf*. <https://doi.org/10.1016/j.addma.2017.06.007>
- [30] Small KA, Clayburn Z, DeMott R, Primig S, Fullwood D, Taheri ML (2020) Interplay of dislocation substructure and elastic strain evolution in additively manufactured Inconel 625. *Mater Sci Eng A*. <https://doi.org/10.1016/j.msea.2020.139380>
- [31] Sarkar A, Mukherjee P, Barat P, Jayakumar T, Mahadevan S, Rai SK (2008) Lattice misfit measurement in Inconel 625 by X-ray diffraction technique. *Int J Mod Phys B*:3977–3985. <https://doi.org/10.1142/s0217979208048772>
- [32] Rai SK, Kumar A, Shankar V, Jayakumar T, Bhanu Sankara Rao K, Raj B (2004) Characterization of microstructures in Inconel 625 using X-ray diffraction peak broadening and lattice parameter measurements. *Scr Mater*. <https://doi.org/10.1016/j.scriptamat.2004.03.017>

Publisher's Note Springer Nature remains neutral with regard to jurisdictional claims in published maps and institutional affiliations.

P1.8 Evolution of preferred orientations at the edge of a sample

Information

The following section was not published as part of the article. Nonetheless, the additional results acquired since the original submission add to the already published insights and underline the complexities of the LPBF process.

rosine: linke seite keine texturänderung underlines the complexity of the phenomena occurring during LPBF which has to be considered when developing numerical models as well.

In section P1.3.2, the influence of repeated laser scanning on the texture was evaluated for a gauge volume located in the center of the sample's fifth layer. It was found that the texture changes and decreases in intensity as the material in the gauge volume is scanned multiple times. After a total of 14 layers were exposed, no more changes in the intensity distribution were found, see figure P1.8.

The same measurement was used for the observation of a gauge volume located at the left edge of a sample processed with the same parameter set as presented in section P1.3.2, namely a laser power of $P_L = 55$ W, scanning speed of $v_L = 50$ mm s⁻¹ and L-scanning. The left edge is where the laser exposure is started.

In figure P1.11, the processing plots analogous to figure P1.8 are shown for this gauge volume. The same range of layers as in the other figure is shown. Since the exposure starts right above the gauge volume at the left edge of the sample. The laser impact is visible directly after the start, making the intensity changes in a single layer slightly harder to spot. However, since the gauge volume stays fixed relative to the sample, the end state of the previous layer can be used as a reference. This comparison reveals some initial changes from $n = 7$ to $n = 8$. The vertical position of some of the horizontal intensity lines change slightly. Furthermore, the contrast, which reflects the intensity of anisotropy, is reduced, which continues through the next layers. It has to be noted that the colormap is scaled logarithmically. Therefore, small changes are emphasized. After $n = 8$, no further intensity distribution changes are observed.

Referring back to the original figure, figure P1.8, intensity changes were observed up to $n = 13$, which reflected significant changes in texture visible from the pole figures in figure P1.7. At the left edge of the sample, this texture change does not seem to occur. This difference is caused by the thermal state of the material. As mentioned above, laser scanning starts right above the left edge. At the start of laser exposure, the sample has had time to cool down during the recoating procedure after the previous exposure. It is essentially at room temperature. Therefore, as the laser exposure starts, all of the material surrounding the gauge volume is cold, resulting in large thermal gradients and fast heat conduction away from the gauge volume. In the original article, the intensity changes were attributed to *in situ* recrystallization due to the repeated scanning. Recrystallization requires both temperature and time. In the case of the left edge gauge volume, the fast heat conduction away from the gauge volume might prevent

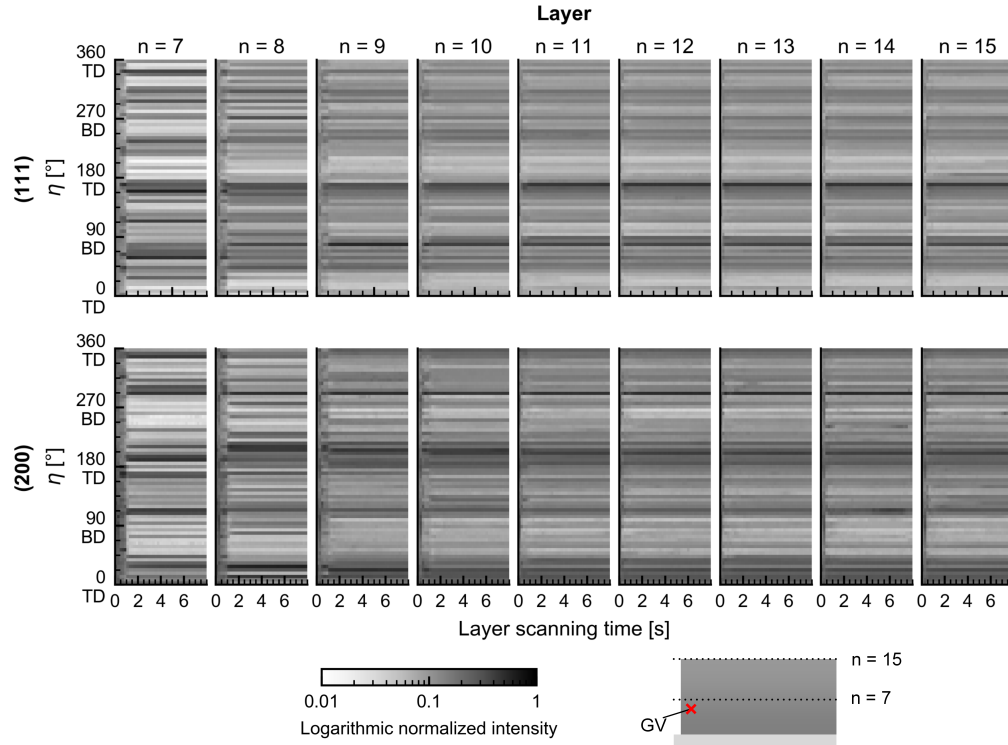


Figure P1.11: Sample manufactured with a laser power of $P_L = 55 \text{ W}$ and $v_L = 50 \text{ mm s}^{-1}$ observed in MM2 at $\zeta_{GV} = 200 \mu\text{m}$: Processing plots for (111) and (200) reflections. Gauge volume located at left edge of sample.

recrystallization from occurring. At the center of the gauge volume, heat accumulation occurs, which increases duration the material is at an increased temperature. Heat accumulation will be discussed in-depth in the second article, chapter P2. The additional results presented in this section underline the complexity of the thermal state in a sample and highlight the necessity of spatially resolved measurements. Tracking a single gauge volume does not necessarily reflect the material's response in the whole part.

Experimental observation of stress formation during selective laser melting using in situ X-ray diffraction

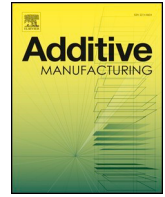
In the following study, the direct observation of stress-related phenomena was reported for the first time. Full diffraction rings were acquired with a good temporal resolution with the custom experimental setup, which yielded directional lattice strain progressions. The mechanisms of stress formation and evolution in LPBF were identified using simplified scanning patterns and comparatively slow scanning speeds. In addition to confirming and expanding upon the models of Mercelis and Kruth, a model for the stress fields surrounding the heat-affected zone is presented.

Furthermore, the impact depth of the energy input is discussed as the stress state in a fixed gauge volume is observed to change continuously throughout the whole manufacturing process. After the original article and supplementary information, the insights presented therein are complemented by additional experimental results. By combining all of the stress-related phenomena observed *in situ*, a part-scale mechanism for the formation of the final stress distribution is proposed, section P2.8. Subsequently, the reader will find a discussion of a recently published article that questioned the stress evaluation procedure presented in the article, section P2.9.

Bibliographic data	
Title	Experimental observation of stress formation during selective laser melting using in situ X-ray diffraction
Authors	<i>Felix Schmeiser</i> , Erwin Krohmer, Norbert Schell, Eckart Uhlmann, Walter Reimers
Journal	Additive Manufacturing
Publisher	Elsevier
Publication Date	31st December 2019
Reference	Additive Manufacturing 32 (2020): 101028
DOI	10.1016/j.addma.2019.101028
My contribution	Planning, executing, and evaluating the <i>in situ</i> LPBF and d_0 diffraction experiments at PETRA III; Data analysis, interpretation, visualization; Writing the manuscript

The manuscript is inserted in the following pages.

Reprinted from Additive Manufacturing, **32** (2020), Felix Schmeiser, Erwin Krohmer, Norbert Schell, Eckart Uhlmann, Walter Reimers, *Experimental observation of stress formation during selective laser melting using in situ X-ray diffraction*, 101028, Copyright (2020), with permission from Elsevier.



Full Length Article

Experimental observation of stress formation during selective laser melting using in situ X-ray diffraction

Felix Schmeiser^{a,*}, Erwin Krohmer^b, Norbert Schell^c, Eckart Uhlmann^b, Walter Reimers^a^a Institute for Materials Science and Technology, Metallic Materials, Technische Universität Berlin, Ernst-Reuter-Platz 1, 10587 Berlin, Germany^b Institute for Machine Tools and Factory Management, Technische Universität Berlin, Pascalstraße 8-9, 10587 Berlin, Germany^c Helmholtz-Zentrum Geesthacht, Max-Planck-Str. 1, 21502 Geesthacht, Germany

ARTICLE INFO

Keywords:

Selective laser melting

In situ

High energy synchrotron radiation diffraction

Stress formation

Inconel 625

ABSTRACT

Despite the ongoing success of metal additive manufacturing and especially the selective laser melting (SLM) technology, process-related defects, distortions and residual stresses impede its usability for fracture-critical applications. In this paper, results of in situ X-ray diffraction experiments are presented that offer insights into the strain and stress formation during the manufacturing of multi-layer thin walls made from Inconel 625. Using different measuring modes and laser scanning parameters, several experimental observations are discussed to validate and extend theoretical models and simulations from the literature. As a sample is built-up layer by layer, the stress state changes continuously up until the last exposure. The localized energy input leads to a complex stress field around the heat source that involves alternating tensile and compressive stresses. The correlation of temperature and yield strength results in a stress maximum at a certain distance to the top layer. The present study demonstrates the potential of high-energy synchrotron radiation diffraction for in situ SLM research.

1. Introduction

Selective laser melting (SLM), also known as laser powder bed fusion (LPBF), is a powder bed based additive manufacturing technique with the capability to produce parts with complex geometry while maintaining good mechanical properties. Though the market of SLM systems has been growing rapidly in the last years [1], process-inherent variations in part quality and mechanical properties inhibit the use of SLM-produced parts in fracture-critical applications [2]. This is particularly due to residual stresses [3,4] and crack-inducing defects [4] in the produced parts, which have a negative effect on fatigue strength. In order to solve process-related quality variations, a profound understanding of the formation of defects and residual stresses is necessary.

During the manufacturing process, a thin layer of metal powder is melted locally by a focused laser beam, then solidifies and bonds with the already solidified layers beneath. After the spreading of a new powder layer, the laser beam scans again and the cycle is iterated until the part is completed. The SLM process leads to a complex thermal regime in the part as the temperature distribution varies rapidly with time and location during manufacturing [5]. As a layer is exposed, the laser energy is focused on a very small spot size, with a typical laser spot diameter of $d_L = 50 \mu\text{m}$ to $200 \mu\text{m}$ [6], which leads to a rapid heating of the exposed area. The metal powder is molten, then solidifies

rapidly while the heat is dissipated into the surrounding volume. At the same time, the laser scan continues and heats the adjacent area so that a track is formed, which again necessitates the dissipation of heat energy.

The numerous repetitions of this procedure on continuously changing positions result in steep temperature gradients. Previously exposed layers are also affected by this and experience cyclic heating and cooling, all of which affects the microstructure of the part, its mechanical properties and the stress state during and after production. During production, as the part is built up layer by layer, heat accumulates in certain areas of the part caused by the increasing distance to the substrate plate and the poor heat conduction in the surrounding metal powder [7]. This adds another thermal boundary condition to be considered.

The phenomena described here, the highly focused heat source, the cyclic heating and cooling as well as the heat accumulation lead to a complex stress development in the part, which was described by Mercelis and Kruth [8]. During the formation of the current topmost layer, its contraction upon cooling is hindered by the underlying material, which leads to tensile stresses in the top layer. As more and more layers are built on top of it, these tensile stresses turn into compressive stresses that balance the tensile stresses of the above layers. The temperature gradient mechanism (TGM) describes the phenomenon of the development of compressive stresses surrounding the laser spot due to

* Corresponding author.

E-mail address: felix.schmeiser@tu-berlin.de (F. Schmeiser).<https://doi.org/10.1016/j.addma.2019.101028>

Received 29 July 2019; Received in revised form 10 December 2019; Accepted 30 December 2019

Available online 31 December 2019

2214-8604/© 2020 Elsevier B.V. All rights reserved.

high temperature gradients. The residual stresses generated during the SLM process can reach the yield strength of the material [8] and generally lead to undesired behavior such as distortion, cracking and early onset fatigue [9–11]. Controlling the stress state by optimizing the process parameters necessitates knowledge of the fundamental physical mechanisms.

Stress measurements have been performed with several methods on different geometries and process parameters. Researchers have used neutron diffraction [12–14], X-ray diffraction [14–16] and synchrotron radiation diffraction [14,17] experiments or mechanical testing [18–20] to determine the residual stress state of parts created via SLM. However, the temporal history of the temperature distribution has a crucial role in the generation of residual stresses [21] and cannot be investigated by ex situ measurements. Controlling the thermal regime during the process is the key to improve the properties of the part. Some modern SLM systems feature melt-pool monitoring and thermal imaging systems to detect hot spots and potential defects during the process [22]. These techniques deliver valuable data about the surface of the part. To gather information about the inner conditions of the part, simulations are a useful tool. Due to the complex heat distribution, simulating the moving heat source and its impact on the underlying material is associated with some uncertainties. Therefore, the simulations have to be validated experimentally.

In situ measurements on bulk properties in general have been scarce, with X-ray imaging techniques emerging only recently. Several research groups have performed X-ray imaging experiments observing melt pool dynamics, pore formation and powder scattering [23–34] in the SLM process. Other experiments provided insights in powder recoating dynamics [35,36] and surface smoothing by laser remelting [37]. Furthermore, the feasibility of in situ X-ray diffraction during SLM was demonstrated [33,34]. However, a comprehensive study of the stress buildup in SLM parts via in situ diffraction is yet to be presented in the literature. The metrological prerequisites to capture the SLM process with good temporal resolution have emerged only in recent years. The latest improvements in synchrotron radiation sources generate highly brilliant radiation and new, fast detectors enable quick image acquisition and high spatial resolutions simultaneously.

To perform such in situ experiments, a custom-built SLM machine is necessary, preferably close to an industrial standard system. Up until now, all presented in situ studies were focused on single track or single layer measurements. For the experiments presented here, a custom-built process chamber based on an industrial standard SLM system is utilized [38]. It allows for in situ X-ray transmission experiments featuring an automated powder recoating system with adjustable layer thickness, a moveable building platform and part geometries up to $70 \times 3 \times 10 \text{ mm}^3$. This machine is capable of fabricating multi-layer samples automatically while simultaneously the synchrotron radiation beam is irradiating a specific, desired gauge volume anywhere in the sample before, during and after laser exposure. Using this machine, Wide Angle X-ray Scattering (WAXS) experiments were performed at the HEMS-beamline P07 at PETRA-III (DESY, Hamburg, Germany) and 2D diffraction patterns were analyzed to gather unprecedented experimental insights on the buildup of strains and stresses in samples made of the nickel base alloy Inconel 625.

2. Materials and methods

2.1. Modified selective laser melting system

The SLM system used in the experiments is a modified AconityMINI from Aconity3D GmbH (Herzogenrath, Germany) with a custom-built process chamber developed and built at Technische Universität Berlin. The laser system consists of a continuous wave ytterbium fiber laser YLR-400-AC from IPG Laser GmbH (Burbach, Germany), which emits radiation at a wavelength of $\lambda = 1070 \text{ nm}$ with a nominal power output of 400 W. The laser fiber is connected to a 3-axis deflection unit Axialscan-

30 from Raylase GmbH (Wessling, Germany) via a collimator. Through the deflection unit, the laser beam with a focus diameter of about $60 \mu\text{m}$ in a working distance of 445 mm is directed onto a powder bed with a size of $70 \times 3 \times 10 \text{ mm}$ (length \times width \times height). The powder bed is limited by a replaceable S355J2 steel substrate on the bottom and two glassy carbon plates, supplied by HTW Hochtemperatur-Werkstoffe GmbH (Thierhaupten, Germany), with a thickness of 1 mm in X-ray transmission direction each. The funnel-based fully automatic powder recoating mechanism and an adjustable layer thickness enable the buildup of samples with a maximum height of 10 mm.

Before each experiment, a new steel substrate was mounted on the sample holder and sandwiched between the glassy carbon plates. Then, the first powder layer was deposited as thinly as possible and checked visually to assure bonding of the melted layer on the substrate. The process chamber was sealed and purged with argon gas until an oxygen level below 2000 ppm was reached. Throughout every experiment, the oxygen content at powder bed level was monitored. In addition, the argon gas atmosphere was circulated by the installed circulation pump and filtered continuously in order to remove welding fumes from the laser beam path. The sample holder was positioned in transverse direction depending on the desired position of the X-ray gauge volume. Inlet and outlet windows of the process chamber for synchrotron radiation are made of Kapton foils (DuPont, Wilmington USA), with a thickness of $50 \mu\text{m}$. Consequently, the synchrotron radiation beam passes through ambient air, Kapton foils, argon and glassy carbon, besides the desired Inconel 625 sample, with overall negligible noise.

In order to keep the boundary conditions concerning the heat flow close to the industrial process, the samples were produced with a maximum thickness of 2.5 mm in transmission direction. Hence, between sample and glassy carbon, a powder barrier with a thickness of about 0.25 mm on both sides was established. Since the thermal conductivity of solidified Inconel 625 is at least one order of magnitude higher than thermal conductivity of Inconel 625 powder [39,40], heat conduction occurs primarily through the solidified parts of the sample. Taking into account simulative results on heat transfer in the formation of melt tracks with steel powder [41], it is derived that the powder barrier in the experiments adequately mimics heat transfer conditions of the conventional SLM process.

2.2. Materials

The samples were built using an Inconel 625 (UNS N06625/W.Nr. 2.4856) metal powder supplied by m4p materials solutions GmbH (Magdeburg, Germany). The particle size ranged from 20 to $63 \mu\text{m}$ according to the manufacturer. The metal powder has a nominal chemical composition of 20.7 wt% Cr, 8.4 wt% Mo, 0.6 wt% Si, 0.4 wt% Mn, 3.5 wt% Nb and 0.5 wt% Fe.

2.3. Experimental procedure

The SLM process in general is adjusted and optimized via a large range of parameters [42] with estimations of more than 130 parameters affecting part quality [43]. In the experiments presented here, the number of variables was reduced to both simplify the manufacturing process as much as possible and to highlight the basic mechanisms at work. Furthermore, a simple geometry was chosen for the samples. Thin walls with dimensions of $20 \times 5 \times 2.5 \text{ mm}^3$ were manufactured using different sets of parameters, see Fig. 1b.

The laser scanning pattern was identified as one of the drivers of thermal management and therefore stress generation [44]. Industrial SLM systems employ various scanning strategies in one part to ensure a good surface finish as well as little to no porosity. To create a smooth finish, the contour of a part is scanned with a different set of laser parameters than the ‘filling’. For the diffraction experiments in transmission mode, this would result in irradiating a gauge volume made up of scanned tracks in different directions and with different scanning

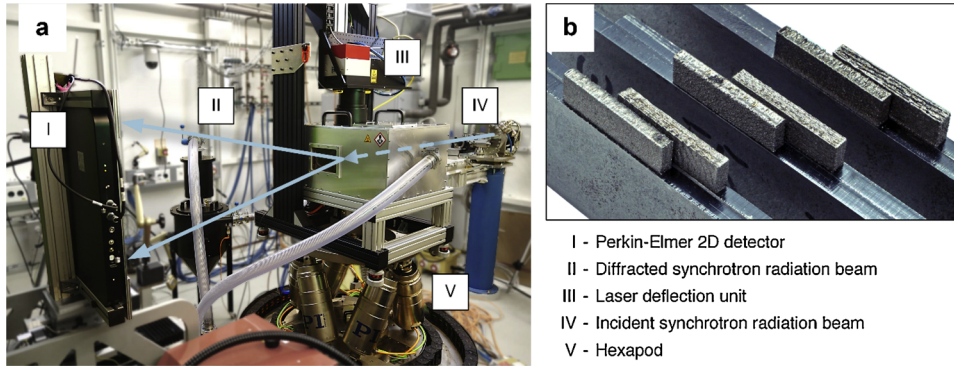


Fig. 1. a) Experimental Setup at PETRA-III P07 EH3 (DESY, Hamburg, Germany) and b) Example parts that were built using the custom SLM system. From left to right: $P_L = 275$ W, L-scan and T-scan. $P_L = 165$ W, L-scan and T-scan. $P_L = 55$ W, L-scan and T-scan. Part geometry $20 \times 5 \times 2.5$ mm³. Parts are built upon steel substrates.

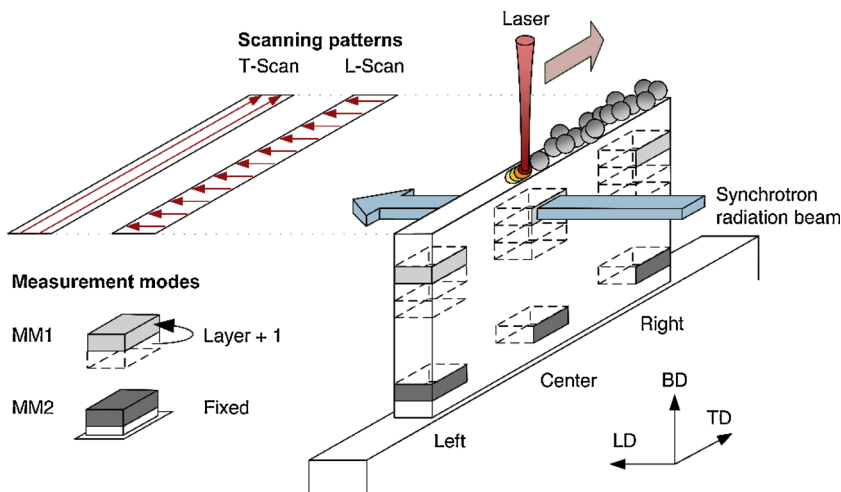


Fig. 2. Experimental Procedure. Measurement Mode 1 (MM1) - Gauge volume in fixed distance to top layer. Measurement Mode 2 (MM2) - Gauge volume in fixed height. Schematic representations of scanning patterns evaluated. For the T-scan, the hatching direction is oriented along LD, while for the L-scan, the hatching direction is oriented along TD.

parameters. This impedes interpretation and complicates the attribution of phenomena to a specific set of parameters. Therefore, no contour scans were employed in the manufacturing of the samples presented here. Furthermore, only unidirectional scanning patterns without meandering were used. Two resulting scanning patterns were investigated and consequently named 'longitudinal scanning' (L-scan) and 'transversal scanning' (T-scan) following the orientation of the scanning vectors in relation to the incident synchrotron radiation beam, see Fig. 2.

The second parameter that was varied is the energy input, i.e. laser power P_L and scanning speed v_L . Three sets of scanning parameters were used and are shown in Table 1. A laser power of $P_L = 275$ W and the corresponding scanning speed of $v_L = 760$ mm/s (set 1) represents an industrial standard parameter set that ensures high density parts. Set 3 features the lowest acceptable laser power that still leads to $\sim 99.5\%$ relative density, as was found in preliminary tests. The low scanning speed of $v_L = 50$ mm/s in turn led to good temporal resolution and a favorable data-to-noise ratio. Set 2 was chosen as an intermediary energy input between the two extremes.

In combination with the two scanning strategies, a total of six sets of parameters were investigated. The other manufacturing parameters were kept constant. Major ones are also presented in Table 1.

In Fig. 2, the experimental procedure concerning the measuring positions is illustrated. For each set, three samples with varying measuring positions were built. Furthermore, two measurement modes were employed. Most of the samples were observed using measurement mode 1 (MM1). In this

configuration, the gauge volume changes from layer to layer and stays in a fixed distance of $150 \mu\text{m}$ to the top layer. On the other hand, the gauge volume in measurement mode 2 (MM2) stays in a fixed position during the whole process. Furthermore, the three major axes are illustrated in Fig. 2. The longitudinal direction (LD) and the transversal direction (TD) span the working plane of the laser on the powder bed, with the longitudinal

Table 1

Sample parameters. a) Laser parameter sets b) Scanning patterns c) Process parameters that were kept constant for all samples.

a)	Laser power P_L [W]	Scanning speed v_L [mm/s]
Set 1	275	760
Set 2	165	456
Set 3	55	50
b)	Hatch length [mm]	No. of hatches
L-Scan	2.28	168
T-Scan	19.8	20
c)	Constant process parameters	
Layer thickness Δz	50	μm
No. of layers	100	
Hatch distance h	120	μm
Laser spot diameter d_L	~ 60	μm
Jump speed v_j	1000	mm/s
Sample geometry	$20 \times 5 \times 2.5$	
		mm ³

direction referring to the beam direction of the incident synchrotron radiation beam. The building direction (BD) is perpendicular to the working plane and refers to the sample height direction.

2.4. In situ high energy synchrotron X-ray diffraction

The in situ diffraction experiments were performed at the HEMS P07 beamline at DESY (Hamburg, Germany) [45] using an energy of $E = 98.02$ keV ($\lambda = 0.12649$ Å). An X-ray beam size of $750 \times 70 \mu\text{m}^2$

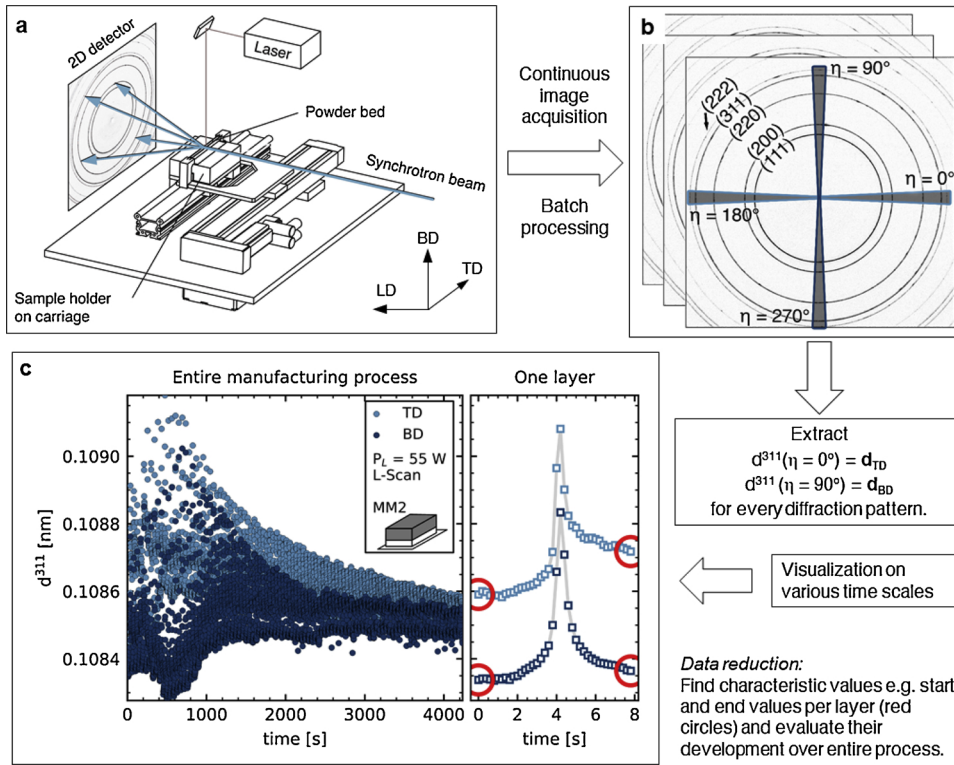


Fig. 3. Schematic data generation and evaluation process: a) Experimental setup with relevant direction denotations, b) Example diffraction pattern and analyzed directions and c) Illustrative data visualizations of a sample manufactured using a laser power of $P_L = 55$ W and L-scan in MM2 with the gauge volume in the center of the 5th layer of the sample. The red circles mark the data points that have been extracted for all layers and subsequently plotted to generate Fig. 4. (For interpretation of the references to colour in this figure legend, the reader is referred to the web version of this article.)

was chosen. This enabled good spatial resolution in build direction. The width of the beam was set accordingly to ensure enough grains being irradiated so that full diffraction patterns could be collected. A schematic setup of both the experiment and the data analysis is shown in Fig. 3.

The modified process chamber was set up on the heavy-duty hexapod provided by Helmholtz-Zentrum Geesthacht. In Fig. 1a, the setup in the experimental hutch at the beamline is shown. The distance between sample and detector was 1521.147 mm to capture full Debye-Scherrer rings of the first five (hkl) reflections. Lanthanum hexaboride (LaB_6) was used to determine the sample-to-detector distance, see supplementary section 2. The Perkin-Elmer XRD1621 detector was used with an exposure time of $t = 0.1$ s and a frame rate of $f = 10$ Hz. Maximum intensity ranged from 100 to 300 counts depending on the reflection chosen. In supplementary Fig. 11, a comparison of a powder sample diffraction pattern and an in situ measurement of solidified material is shown.

The diffraction patterns were segmented into cake pieces and integrated using Fit2D [46] to gather 1D-2 θ -profiles from the 2D diffraction patterns. The 1D profiles were batch-processed using custom Python scripts that featured the 'lmfit' package [47]. A Voigt function was used to fit the experimental data and determine the peak position, full-width half maximum (FWHM) and integrated intensity of the (311) reflection. As mentioned in section 2.1, there was a powder barrier between the glassy carbon plates and the sample, which was irradiated as well. As the powder barrier is thin compared to the solidified material, contributing to $\sim 13\%$ of irradiated mass, its diffracted intensity is much lower than the bulk material. Unlike the bulk material, the powder does not experience mechanical stresses that induce peak shifts in the diffraction patterns. The superposition of unstressed powder with low diffracted intensity and stressed bulk material with a high diffracted intensity produces asymmetric peaks, which reduce the accuracy of the fitting function. To account for the powder layer, thus only the top 60% of the peak data was used for the peak fitting. This way, the diffracted intensity of the powder barrier and the resulting asymmetry was filtered out and did not distort the subsequent analysis.

2.5. Strain free lattice parameter

The strain free lattice parameter is dependent of the chemical composition and crystallographic structure of the material. Wang et al. showed that the chemical composition of Inconel 625 processed via SLM can actually change as the part is being built up [48]. This in turn alters the strain free lattice parameter. To verify if this was the case in our samples as well, wavelength-dispersive X-ray spectroscopy (WDX) measurements were performed on the TD-BD plane of the specimen at ZELMI, Technische Universität Berlin. One sample per set of parameters, six in total, was investigated.

Seven alloy elements were analyzed: Ni, Cr, Mo, Nb, Fe, Si and Mn and a circular spot size of $d = 20$ μm was used. To investigate potential concentration gradients in both TD and BD, line scans with a step size of 500 μm , ranging from the lower edge of the part to the top edge were performed in three locations, i.e. left edge, center and right edge. The substrate was cut off for this investigation.

Contrary to Wang et al., our samples showed no concentration gradients of the alloy elements – neither over the height (BD) of the sample nor its length (TD). While there was a standard deviation of 0.25 to 0.29 wt% of chromium, the most volatile alloy element, for each line scan, the changes in concentration over the sample height and width were stochastic and did not follow any monotonous trends.

Comparing the gauge volume of WDX, 20 μm in diameter, to the one used for the in situ WAXS measurements, $750 \times 70 \times 2500$ μm^3 , the diffraction measurements average over a much larger volume. Therefore, the strain free lattice parameter is insusceptible to the slight local differences in composition shown by WDX. As no compositional gradients emerged from our measurements, a single d_0 is proposed to be sufficient to characterize the whole sample.

To determine d_0 , small cuboids with an edge length of 700 μm were cut out of the parts using micro electrical discharge machining (EDM) for subsequent diffraction experiments. Opening the aperture to 1×1 mm^2 , this sample size enabled 'bathing' the cuboids in the synchrotron radiation beam so that all cuboid surfaces were irradiated. By irradiating the whole volume of the specimen, a stress-free state can be

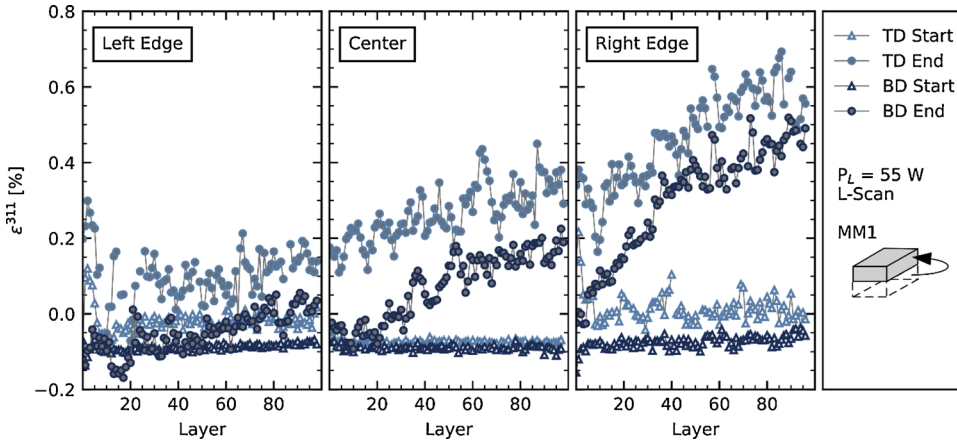


Fig. 4. Strain progression for TD (light blue) and BD (dark blue). Triangular markers show the first strain value measured in the gauge volume for that layer after the laser was turned on, circle markers show last strain value of that layer before the laser was turned off. (For interpretation of the references to colour in this figure legend, the reader is referred to the web version of this article.)

assumed considering the force and moment equilibrium. The strain free lattice parameter can therefore be calculated from the peak position.

Additionally, the d_0 -measurements were performed in a DHS1100 furnace from Anton Paar GmbH (Graz, Austria) to assess the temperature dependence of d_0 for temperatures up to $T = 800^\circ\text{C}$, which was found to be linear for all of the samples investigated, see supplementary Fig. 14.

2.6. Strain and stress analysis

Using the d_0 measurements, the lattice spacings were converted into strains following

$$\varepsilon^{311} = \frac{d^{311} - d_0^{311}}{d_0^{311}}. \quad (1)$$

This was done for the two assumed principal directions of stress, TD and BD, see analogous procedures for the calculation of asymmetric strains in high pressure research [49]. To prevent a beam center error, the lattice spacings extracted from two opposing cake pieces were averaged as illustrated in Fig. 3. Hence, d_{TD} is calculated by averaging the lattice parameter at $\eta = 0^\circ$ and $\eta = 180^\circ$, the lattice parameter in building direction d_{BD} by averaging $\eta = 90^\circ$ and $\eta = 270^\circ$. The strains calculated this way are the sum of the elastic and the thermal component, though. Without knowledge of the exact temperature, the purely elastic component cannot be determined. Since d_0 itself is temperature-dependent, the calculation of absolute strains is not possible. Therefore, the absolute strain values given in the plots are not discussed further, as they are arbitrarily based on a constant, temperature-independent d_0 . Nevertheless, the visualization of the directional strains is a valuable tool to detect differences in trends between TD and BD.

On the other hand, the strain difference between TD and BD is calculated as

$$\varepsilon_{TD-BD}^{311} = \frac{d_{TD}^{311} - d_{BD}^{311}}{d_0^{311}}. \quad (2)$$

Because both lattice parameters are calculated from the same diffraction pattern and gauge volume, any difference between the two cannot be due to a difference in temperature and is therefore purely elastic. Furthermore, the temperature-dependence of d_0 has a negligible effect on the strain difference. From the strain difference ε_{TD-BD} , the stress difference can be calculated with Eq. (3),

$$\sigma_{TD} - \sigma_{BD} = \frac{E^{311}}{(1 + \nu^{311})(1 - 2\nu^{311})} [(1 - \nu^{311})(\varepsilon_{TD} - \varepsilon_{BD}) + \nu^{311}(\varepsilon_{BD} - \varepsilon_{TD})] \quad (3)$$

which was derived from Hauk et al. [50]. The temperature-dependence of the elastic constants was extrapolated from the single crystal constants presented by Wang et al. [51]. In supplementary section 4 the

relevant data is presented. The coefficient of thermal expansion was calculated from the experimental data described in the section 2.5. It is shown in supplementary Fig. 14. In this way, the stress difference was determined for a number of different temperatures. Temperature gradients in the gauge volume cannot be resolved. Due to the gauge volume's geometry, the temperature gradients are more pronounced in TD than in BD, therefore leading to a higher uncertainty of the stress values in TD.

However, the lattice spacings for TD and BD are extracted from the same diffraction pattern from the same gauge volume. They are therefore affected by the temperature gradients in the same magnitude. Thus, the uncertainty of the lattice spacings in TD and BD is the same and mostly dependent on the fitting uncertainty of the raw data, which was negligible in our case.

3. Results

3.1. Influence of heat input on strains

One of the key origins of stresses during SLM are the thermal gradients inherent to the process [8]. During the manufacturing process, the heat distribution changes continuously. To demonstrate this, it is suitable to investigate the development of certain strain values over the course of production.

One example is shown in Fig. 4. The data is derived from three samples, which were built using the same set of parameters, i.e. L-scan and a laser power of $P_L = 55\text{ W}$, while respectively observing the three measuring positions, i.e. left edge, center and right edge, of the sample. The experiments were performed in MM1. In Fig. 4, the data points represent the strain values at the start and at the end of each layer for all layers over the course of manufacturing, whereby 'layer' means during exposure and laser-metal-interaction, see Fig. 3.

The first strain value for each layer delivers information about the strain state after recoating and subsequent cooling of the sample. Then, during the production of one layer, the laser passes over the gauge volume and leads to a sharp increase in the strains. After the laser passage, the gauge volume cools again, but the strains stay elevated, which is mirrored by the last strain value for each layer. For each of the measuring positions, the start values stay relatively constant for all layers, but there are distinct trends in the progression of the end values over the course of the manufacturing process.

The constant values at the start of each layer can be explained with the inter-layer dwell time due to recoating. After the previous layer has been fully exposed, the sample is coated again with a new powder layer. The recoating process takes about 15 s. During this time interval, the whole sample and therefore the gauge volume cools down. Therefore, the temperature and the strain state are constant at the beginning of each layer. At the end of one layer, the gauge volume is obviously

hotter than in the beginning, which explains the difference between start and end values in one layer. As more layers are built, the top surface of the sample and accordingly the gauge volume increases its distance from the substrate, which serves as a heatsink. As the distance rises, the heat transfer away from the heat source and the gauge volume is hindered by heat accumulation. Therefore, the end strain values increase with an increasing number of layers.

The L-scan utilized for these samples illuminates another effect, which is heat accumulation in lateral direction from left to right, which is in accordance with simulative results from Parry et al. [52]. The graphs for the end values get much steeper from left to right. The gauge volume in the left measuring position is exposed right at the start of each new layer when the sample in total has cooled due to the coating procedure. This allows for a fast heat transfer away from the gauge volume and results in moderately constant end values for each layer. The gauge volume on the right side of the sample is exposed in the end of each layer. At the point that the laser passes over the gauge volume, about 95% of the sample has already been exposed and therefore heated significantly. This inhibits the heat transport away from the gauge volume and leads to a sort of lingering heat, which in turn results in a steep increase in the end strain values.

While Fig. 4 shows the values for a moving gauge volume (MM1) and thus delivers information about the upper region of the sample, Fig. 5 demonstrates the impact of the laser in the lower region of the sample. The figure shows the strain progression in a fixed gauge volume (MM2) placed in the 5th layer of the sample. Each subplot shows the strains at a point where a specific number of layers has been processed, yet the gauge volume stays in the 5th layer.

A number of observations can be supported by this figure. Each laser passage over the gauge volume influences the strain state, regardless of the gauge volume's distance to the heat source. This figure illustrates that the laser has an impact on the strain state of the first layers until the very end of the manufacturing process, despite there being about 4.5 mm of material above the gauge volume. While the strains in TD and BD converge over time, the laser passage still leads to a visible peak in the strains. At the same time, the laser does not have the same effect on both directions. The strains in TD are affected more, resulting in a higher peak there.

The occurrence of a peak is expected as a result of the heat flow from the top layer during exposure, which in turn leads to thermal expansion throughout the sample. On the other hand, the difference in peak height is surprising and cannot be attributed to temperature. Instead, it is proposed that tensile stresses are induced in TD. The lower peak in BD is a reaction to the tensile stresses in TD and a result of transverse contraction due to the constant volume boundary condition. As the laser scans the top layer, the thermal expansion in BD is uninhibited due to the free surface at the top. In TD on the other hand, the surrounding material acts as a fixation, so that the thermal expansion of the top portion of the sample induces tensile stresses in the gauge volume, which leads to the peak visible in the figure. After the laser has passed, the strains in TD and BD converge again at a higher strain point

than at the beginning of the layer. This demonstrates that the strain state in the observed gauge volume is altered by the laser up to the last layer.

The transverse contraction hypothesis is also supported by the T-scan experiments. In Fig. 6, the strain progression for nine consecutive layers in a T-scan sample is shown. The strains in TD form a steep slope in each layer. This is caused by the uniform heating of the gauge volume via the T-scan. In contrast to the L-scan, here the laser passes over the gauge volume about 20 times in total during the exposure of a single layer. Therefore, the gauge volume heats more uniformly than in the L-scan, where a visible peak is formed as seen in Fig. 5. The increase in temperature leads to a rise of the lattice strains, as visible in TD. In BD on the other hand, the slope is minimal and for some of the layers displayed in the figure, e.g. for layer 10 and 14, the values even stay constant at $\epsilon^{311} = 0\%$. Therefore, the increase in lattice strain due to thermal expansion has to be counteracted and compensated by a different mechanism. As discussed earlier, tensile stresses are induced in the gauge volume in TD due to hindered contraction. These lead to a further increase in lattice strains in TD. As a result of these tensile stresses, a transverse contraction is induced in BD. The transverse contraction offsets the thermal expansion so that the net lattice strain is close to zero percent.

3.2. In-plane stresses and out-of-plane stresses

So far, results referring to the influence of temperature and heat distribution on the strain state have been described using the in situ measurements. The next step is the validation of existing models for stress formation during the SLM process.

As mentioned in section 2.3, BD is the direction perpendicular to the working plane and therefore characterizes out-of-plane stresses. The working plane is defined by LD and TD. Therefore, in-plane stresses are characterized by TD as the experimental data delivers no information in LD.

In all of the experiments using MM1, the lattice spacings in TD were larger than in BD. This is demonstrated in Fig. 7, which shows the median lattice spacings for all sets of parameters. This effect is a result of the cooling of the top layer. The solidified material shrinks as it cools. The underlying, colder material inhibits the contraction, which induces compressive stresses in TD in the top layer and tensile stresses in TD in the underlying material. In response, the tensile stresses cause a transverse contraction in BD. These two mechanisms lead to the difference in the median lattice spacings, shown in Fig. 7. Because the temperature in the gauge volume and therefore for TD and BD is the same, the difference has to be explained as a stress effect.

In the literature, divergent results have been presented. Bass et al. found that the stresses in build direction were larger than the in-plane stresses on the outside of their cylindrical parts, but smaller closer to the center of the part [53]. Nadammal et al. on the other hand reported stress distributions that were similar in TD and BD in both the middle of their part as well as the edge [54]. Our experiments show that during

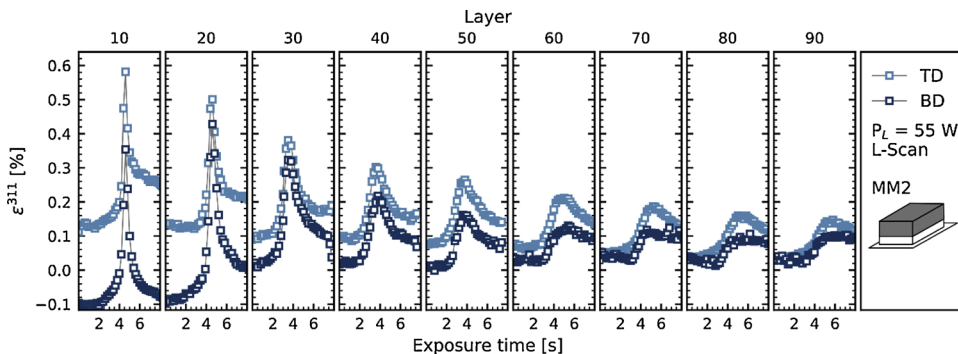


Fig. 5. Strain progression in MM2, measuring position in the center of the sample. Each subplot shows the progression for one layer. The gauge volume was placed in the 5th layer, so the first subplot shows the strain progression with 5 additional layers above the gauge volume; in the second subplot, 15 layers are above the gauge volume and so on. The data points marked in light blue show the strains in TD, dark blue ones show BD. (For interpretation of the references to colour in this figure legend, the reader is referred to the web version of this article.)

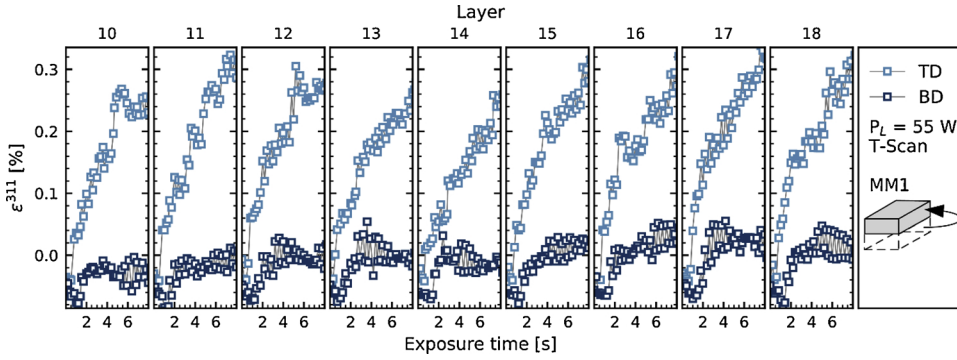


Fig. 6. Strain Progression in MM1, measuring position in the center of the sample. Each subplot shows progression for one layer. The data points marked in light blue show the strains in TD, dark blue ones show BD. (For interpretation of the references to colour in this figure legend, the reader is referred to the web version of this article.)

the manufacturing process, the stresses are higher in TD than BD in all of the examined measuring positions. In layers with increased distance to the top, the findings might be different and are subject to further investigations.

3.3. Thermal gradient mechanism

In 2006, Mercelis and Kruth proposed the thermal gradient mechanism (TGM) as one of the driving factors in the generation of residual stresses during SLM [8]. They argue that the rapid heating by the laser beam leads to steep temperature gradients. As the material's strength drops due to the increase in temperature, it expands for the same reason. The expansion is hindered by the colder material below and thus, compressive stresses are induced in the hot material. These compressive stresses caused by the laser can be observed in the experiments presented here.

Fig. 8 shows the strain progression in a section of nine layers for a sample that was scanned longitudinally with a laser power of $P_L = 165$ W. This sample showed local minimal strain values in TD right before the strain peak in 76 out of 100 layers. The minimal values are marked with red circles. The drop occurs as the laser approaches the gauge volume. Therefore, the gauge volume is heated up, which should result in an increase in strains due to thermal expansion. Right before the laser passes the gauge volume, the compressive stress field induced by the laser and described by Mercelis and Kruth counteracts the thermal expansion to a degree that shows up as an actual drop in strains. Mercelis and Kruth do not distinguish between in-plane and out-of-plane stresses in their model, though. Following their argument, the drop in strains should be visible in both directions, which it is not. This might be caused by the proximity of the gauge volume to the top layer. Perhaps a strain decrease in BD would be visible in a gauge volume further below the top layer. If both the mechanical and thermal boundaries of our experimental setup are incorporated into the model by Mercelis and Kruth, an additional stress-inducing mechanism is

possibly present here.

The gauge volume is fixed in the center of the sample. During the L-scan, the laser scan is headed from left to right. Right before the laser passes over the gauge volume, the part of the sample that is left of the gauge volume is very hot while the rest of the sample is at a low temperature, see supplementary Fig. 12 for reference. There is a temperature gradient in both TD and BD, though. The material's response in BD can be imagined as that of a cantilever beam in this scenario, because there is a free surface that permits uninhibited thermal expansion while the substrate acts as the fixed end. TD on the other hand can be pictured as a beam that is fixed on both sides due to the material bonding to the substrate. The fixed beam is heated on one side. Before any heat flow can occur, the heated part expands due to thermal expansion. Because the beam is fixed on both ends, the other side, where the gauge volume is located, has to be compressed. This difference between BD, free end, and TD, fixed on both ends, causes the drop in lattice spacing to occur only in TD.

3.4. Thermally induced stress maximum

The magnitude of thermally induced stresses varies during the process depending on the distance of the observed volume to the heat source. To illustrate this, the median stress difference for each layer is calculated and shown in Fig. 9. At this point, the utilized custom-built SLM system does not feature a temperature measuring device. Since the mechanical properties and the strain-free lattice parameter change with temperature, the stress progression is shown for a range of temperatures from room temperature up to $T = 1200$ °C. Regardless of the exact temperature of the gauge volume, there is a noticeable trend in the stress progression.

Up until layer 11, the median stress difference is increasing in every layer. Since the stress difference between TD and BD is analyzed instead of absolute stresses in either direction, it is not possible to distinguish between tensile and compressive stresses in the individual directions.

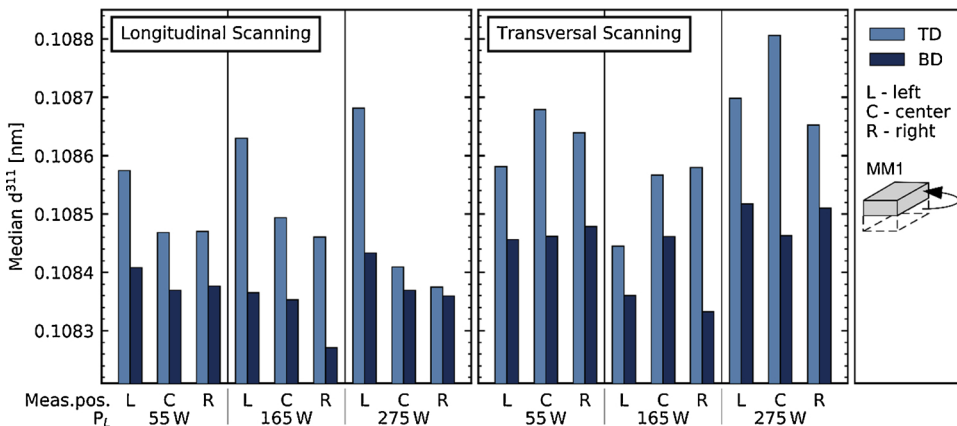


Fig. 7. Median d^{311} values over the whole process sorted by process parameters. Light blue bars represent the median lattice spacing in TD and dark blue bars in BD. For all sets of process parameters, the median lattice spacing in TD is larger than in BD. (For interpretation of the references to colour in this figure legend, the reader is referred to the web version of this article.)

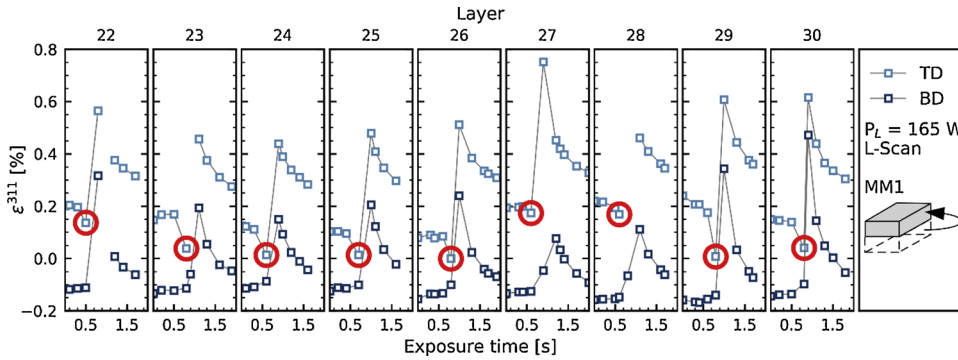


Fig. 8. Strain progression MM1, measuring position at left edge of the sample. The data points marked in light blue show the strains in TD, dark blue ones show BD. Red circles mark the minimum strain value in TD for each layer. Low data density and missing values are caused by the high laser scanning velocity of $v_L = 456$ mm/s and an unfavorable data-to-noise ratio. (For interpretation of the references to colour in this figure legend, the reader is referred to the web version of this article.)

Nevertheless, in conjunction with the results described earlier, it seems plausible that a combination of a maximum in tensile stresses in TD and a resulting maximum transverse contraction in BD lead to the observed maximum in stress difference. The data shows that the stress difference reaches a maximum about 300 μ m below the top layer and the heat source. After that, the stress differences decrease and converge to almost zero. This does not mean that the directional stresses are equal to zero, but the stress anisotropy is greatly reduced.

In the first data points in Fig. 9, the gauge volume is located directly below the top layer. Here, the temperature of the gauge volume is very high, therefore leading to a significant reduction in the material's yield strength σ_y . Due to the reduced strength of the material, the magnitude of stresses resulting from the hindered contraction described earlier is limited. As more layers are built, the gauge volume's temperature decreases, which in turn results in an increase in yield strength σ_y . The material, now being colder and having higher strength, can endure higher elastic stresses, which leads to the maximum in stress difference visible in the plot. After reaching the maximum, the impact of the hindered contraction in the top layer on the gauge volume diminishes, leading to a reduction of the stress difference until it eventually converges to zero. The repeated laser scans with each layer act as a stress-relieving heat treatment, thereby further reducing the stress anisotropy.

For subsequent investigations, MM2 will be used at varying layer counts to investigate whether the appearance of the maximum stress difference changes over the course of production or whether it is constantly to be found about 300 μ m below the top surface.

3.5. Stress fields in the heat affected zone

The results presented in the previous sections illustrate the generation of stresses during the SLM process in various ways. By combining these results, a schematic depiction of the heat affected zone (HAZ) surrounding the laser spot was developed. The HAZ encompasses varying stress fields caused by the heating and cooling of the material, which were observed in the various experiments discussed here. In

Fig. 10, a qualitative illustration of the HAZ is shown. Furthermore, the strain progression for a single layer representative of all of the following effects is given to show the corresponding data points.

The HAZ consists of the melt pool, a plasticized zone around the melt pool, the cooling zone trailing the laser spot and a compressive zone, which was first described in the present study.

During the exposure of a single layer, the strain progression in a fixed gauge volume can be segmented into four distinct zones. In both zone 1 (cold zone) and zone 4 (cooling zone) the TGM causes the strain difference. During the exposure of the previous layer, the material in zone 1 was exposed and plasticized. Due to the high temperature, the associated low strength and the hindered expansion, the material was compressed plastically. Then, after being exposed by the laser, the material cooled down. At this point, the shrinkage was hindered by the underlying material. The hindered contraction has a much higher impact in-plane of the layer (TD) than out-of-plane (BD). Therefore, the tensile stresses described by the TGM are induced in TD. Subsequently, BD is compressed due to transverse contraction, thusly explaining that the strains in TD are generally higher than in BD.

The analogous process happens in zone 4. After the exposure by the laser at $t = 1.0$ s, the material cools down and experiences the same stress inversion as zone 1 in the previous layer, resulting in high strains in TD due to tensile stresses and lower strains in BD as a result of transverse contraction. As shown in section 3.4, the magnitude of this effect changes with the vertical distance between the laser spot and the gauge volume.

In zone 2 (compression zone) a new effect not previously observed is at play. The thermal conduction is slower than the reaction of the material to heat. Therefore, the HAZ expands rapidly while zone 2 is still cold and therefore, with respect to Fig. 10, compressed by the incoming hot material on the left.

The position of the gauge volume relative to the heat-affected zone (HAZ) around the laser is of great importance. Due to the extremely high heating and cooling rates of up to 10^6 K/s during cooling as investigated by Bertoli et al. [55], some of the effects are only observable in very specific locations.

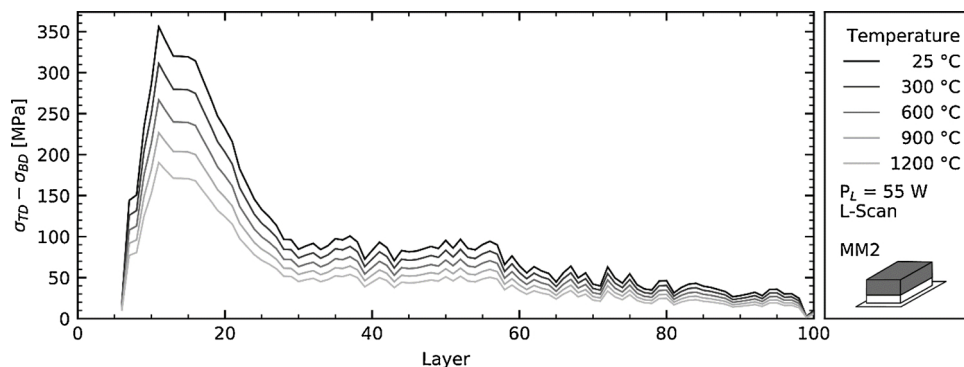


Fig. 9. Layer-wise median stress difference $\sigma_{TD} - \sigma_{BD}$ for complete manufacturing process in MM2 with the gauge volume placed in the center of the 5th layer of the sample. Different shades of grey correspond to different temperatures. The median stress difference was calculated from the median strain difference per layer.

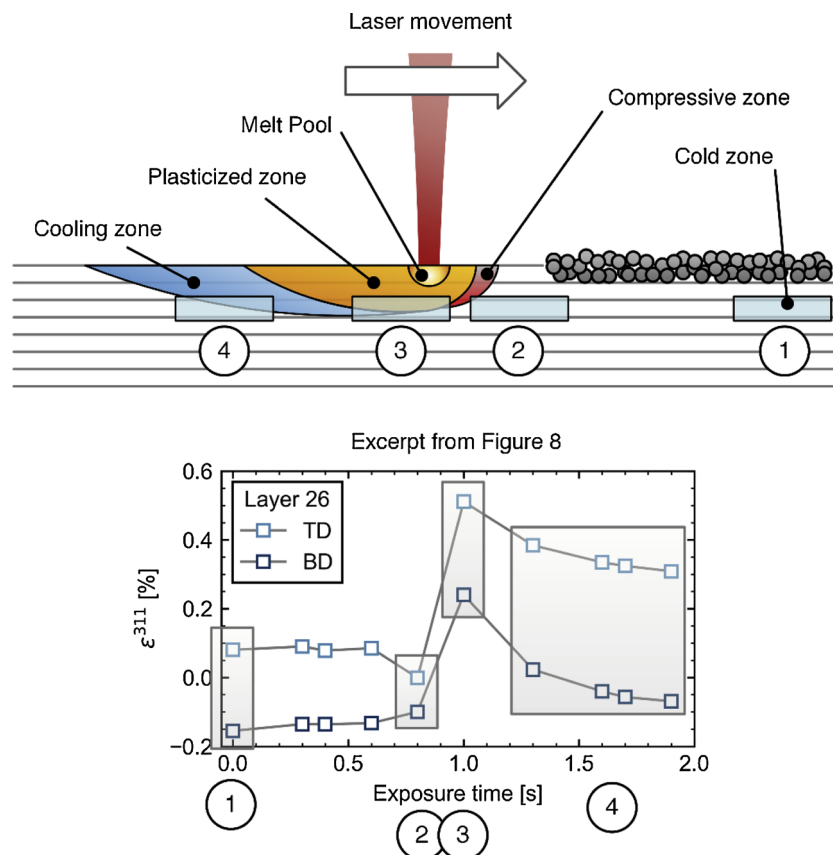


Fig. 10. Model of the HAZ, its stress fields and the corresponding data points observed during the in situ measurements. Top: Schematic representation of the HAZ. Bottom: Strain progression during a single layer, excerpt from Fig. 8.

4. Conclusions

Utilizing a custom-built SLM system, the first comprehensive in situ diffraction experiments were performed for this emerging manufacturing process at the P07 HEMS beamline at DESY. Different measurement modes were employed that allowed both tracking a single, fixed gauge volume in the sample and fixing the gauge volume relative to the top surface. Several thermal phenomena during the SLM process were shown experimentally, including lateral heat accumulation in a single layer as well as vertical heat accumulation in build direction. Furthermore, the results provide insights in a number of stress-related phenomena during laser-metal interaction. In-plane strains were found to be generally higher than out-of-plane strains, with tensile stresses in TD resulting in a transverse contraction in BD. The localized heat input induces a complex stress field that involves an outer halo of compressive stresses, which was experimentally detected in TD. Furthermore, the TGM model was confirmed and a mechanism that clarifies directional differences in the emerging stress field was introduced. During the SLM process, the stress state of the sample is altered by the laser up to the very last layer. A maximum stress difference between in-plane and out-of-plane stresses was found about 300 μm below the top layer when using the L-scan, a laser power of $P_L = 55 \text{ W}$ and a scanning speed of $v_L = 50 \text{ mm/s}$.

For the first time, the strain and stress development during the manufacturing of SLM parts was investigated using in situ X-ray diffraction. The presented results prove the feasibility of in situ diffraction experiments for multi-layer samples in SLM based on a custom-built process chamber for an industrial scale machine. In situ diffraction experiments offer remarkable and promising insights into the strain and stress development as presented in this study. Furthermore, in future, the 2D diffraction data will yield significant findings regarding texture

development and, when using different materials, phase transformations during the process.

CRediT authorship contribution statement

Felix Schmeiser: Conceptualization, Formal analysis, Data Curation, Investigation, Writing - original draft, Visualization. **Erwin Krohmer:** Methodology, Conceptualization, Investigation, Writing - original draft, Visualization. **Norbert Schell:** Investigation, Writing - review & editing. **Eckart Uhlmann:** Supervision, Writing - review & editing, Funding acquisition. **Walter Reimers:** Supervision, Writing - review & editing, Funding acquisition. "does not match the list of acceptable roles. Please choose a role from the below list for this author: Conceptualization; Data curation; Formal analysis; Funding acquisition; Investigation; Methodology; Project administration; Resources; Software; Supervision; Validation; Visualization; Writing - original draft; Writing - review & editing."

Acknowledgements

This research is based on the project DFG RE 688/73-1, UH 100/207-1 respectively, which is kindly supported by the Deutsche Forschungsgemeinschaft (DFG). The authors acknowledge Helmholtz-Zentrum-Geesthacht for the provision of laboratory facilities, various SLM system accessories and experimental support. The authors acknowledge Helmholtz-Zentrum-Berlin for the provision of laboratory equipment and ZELMI at Technische Universität Berlin for the WDX measurements. Finally, the authors thank Alexander Poeche, Amadeus Pauer, Bettina Camin, Emad Mawaad, Francisca Cemerika, Henry Angerstein, Jan Rosigkeit, Jonas Schmidt, Mateus Dobecki, Matthias Schelhorn, Thomas Braun and Wilhelm Schulze for their support

- dimensional detector software: from real detector to idealised image or two-theta scan, *High Press. Res.* 14 (1996) 235–248, <https://doi.org/10.1080/08957959608201408>.
- [47] M. Newville, T. Stensitzki, D.B. Allen, A. Ingargiola, LMFT: Non-Linear Least-Square Minimization and Curve-Fitting for Python, Zenodo, 2014.
- [48] Z. Wang, E. Denlinger, P. Michaleris, A.D. Stoica, D. Ma, A.M. Beese, Residual stress mapping in Inconel 625 fabricated through additive manufacturing: method for neutron diffraction measurements to validate thermomechanical model predictions, *Mater. Des.* 113 (2017) 169–177, <https://doi.org/10.1016/j.matdes.2016.10.003>.
- [49] A.K. Singh, The lattice strains in a specimen (cubic system) compressed non-hydrostatically in an opposed anvil device, *J. Appl. Phys.* 73 (1993) 4278–4286, <https://doi.org/10.1063/1.352809>.
- [50] V. Hauk, *Structural and Residual Stress Analysis by Nondestructive Methods*, Elsevier, 1997.
- [51] Z. Wang, A.D. Stoica, D. Ma, A.M. Beese, Diffraction and single-crystal elastic constants of Inconel 625 at room and elevated temperatures determined by neutron diffraction, *Mater. Sci. Eng. A* 674 (2016) 406–412, <https://doi.org/10.1016/j.msea.2016.08.010>.
- [52] L. Parry, I.A. Ashcroft, R.D. Wildman, Understanding the effect of laser scan strategy on residual stress in selective laser melting through thermo-mechanical simulation, *Addit. Manuf.* 12 (2016) 1–15, <https://doi.org/10.1016/j.addma.2016.05.014>.
- [53] L. Bass, J. Milner, T. Gnäupel-Herold, S. Moylan, Residual stress in additive manufactured nickel alloy 625 parts, *J. Manuf. Sci. Eng.* 140 (2018) 61004, <https://doi.org/10.1115/1.4039063>.
- [54] N. Nadammal, S. Cabeza, T. Mishurova, T. Thiede, A. Kromm, C. Seyfert, L. Farahbod, C. Haberland, J.A. Schneider, P.D. Portella, G. Bruno, Effect of hatch length on the development of microstructure, texture and residual stresses in selective laser melted superalloy Inconel 718, *Mater. Des.* 134 (2017) 139–150, <https://doi.org/10.1016/j.matdes.2017.08.049>.
- [55] U. Scipioni Bertoli, G. Guss, S. Wu, M.J. Matthews, J.M. Schoenung, In-situ characterization of laser-powder interaction and cooling rates through high-speed imaging of powder bed fusion additive manufacturing, *Mater. Des.* 135 (2017) 385–396, <https://doi.org/10.1016/j.matdes.2017.09.044>.

P2.7 Supplementary Information

P2.7.1 Supplementary Figures

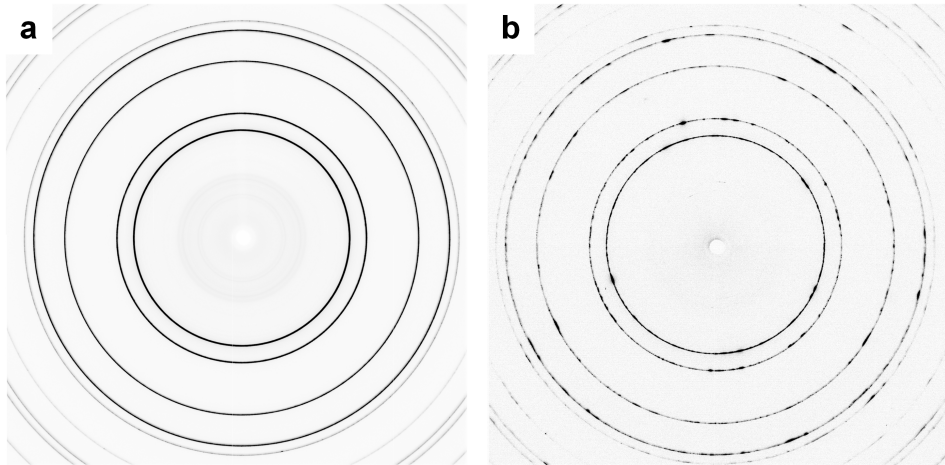


Figure P2.11: Example diffraction patterns of a) Inconel 625 powder measured ex situ and b) bulk Inconel 625 processed by SLM measured in situ. The powder diffraction pattern shows a uniform intensity distribution and perfectly circular rings, while the in situ measurement of solidified material shows an uneven intensity distribution, which indicates the growth of coarser grains and preferred orientations.

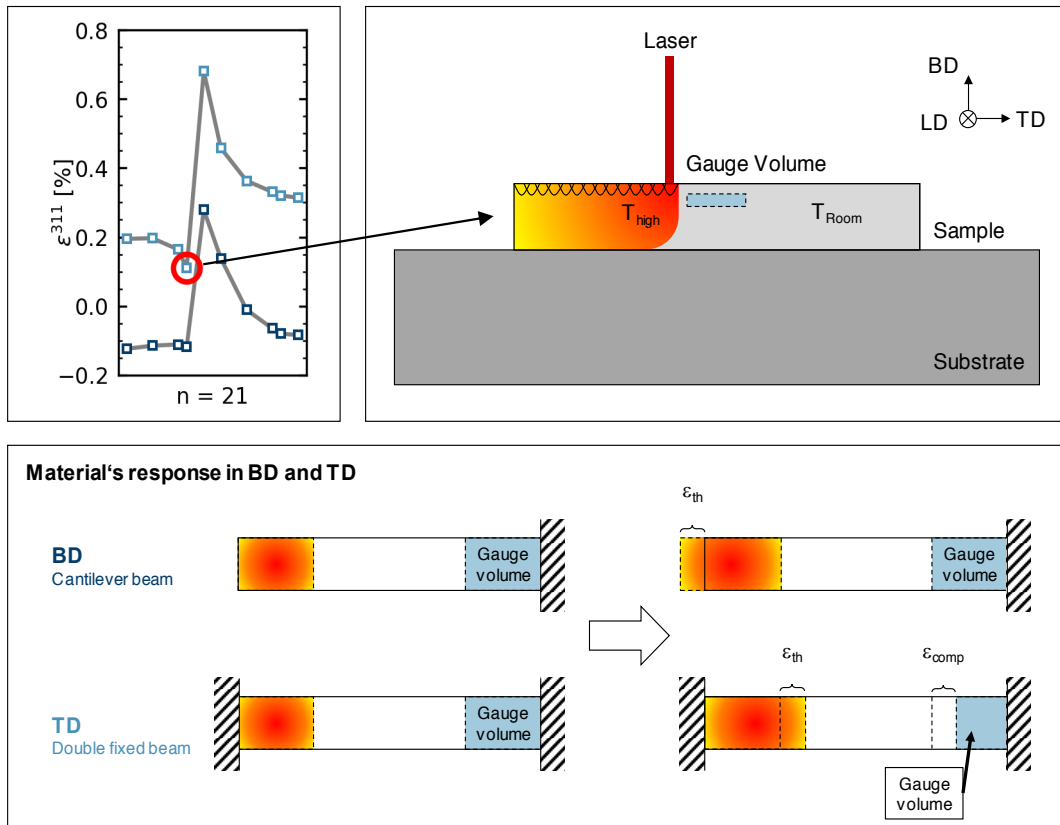


Figure P2.12: Model representation of material's response to approaching heated zone.

P2.7.2 Calibration using LaB_6

LaB_6 powder is commonly used in diffraction experiments to calculate the sample-to-detector distance and the detector tilt. To perform the calibration, the powder sample was fixated between the glassy carbon plates in the process chamber in place of a sample. Diffraction patterns were acquired with the same exposure parameters as during the in situ measurements. As a powder, LaB_6 is stress-free and therefore shows perfectly circular diffraction rings.

Since the lattice spacings of LaB_6 have been determined very precisely in the past, the software Fit2D, which was used for the subsequent image analysis, can determine the experimental parameters sample-to-detector distance and detector tilt by fitting a number of Debye-Scherrer rings. In figure P2.13a, an example diffraction pattern of LaB_6 is shown. After calibration and full azimuthal integration over 360° , the result is figure P2.13b, where the vertical axis corresponds to the azimuthal angle and the horizontal axis corresponds to the diffraction angle. There, it is clear to see that the diffraction rings, projected as lines, are vertical and parallel, therefore the calibration was successful and the subsequent image analysis of Inconel 625 diffraction patterns was correct.

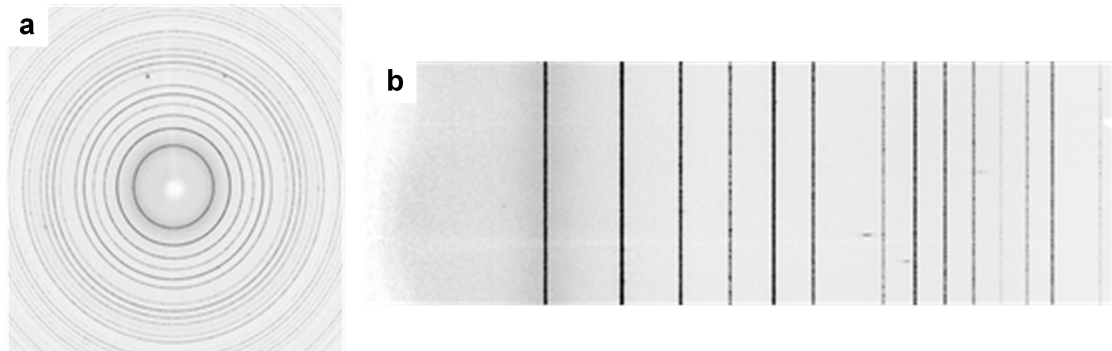


Figure P2.13: LaB_6 powder diffraction pattern a) before calibration and b) after calibration and full azimuthal integration.

P2.7.3 Strain-free lattice parameter

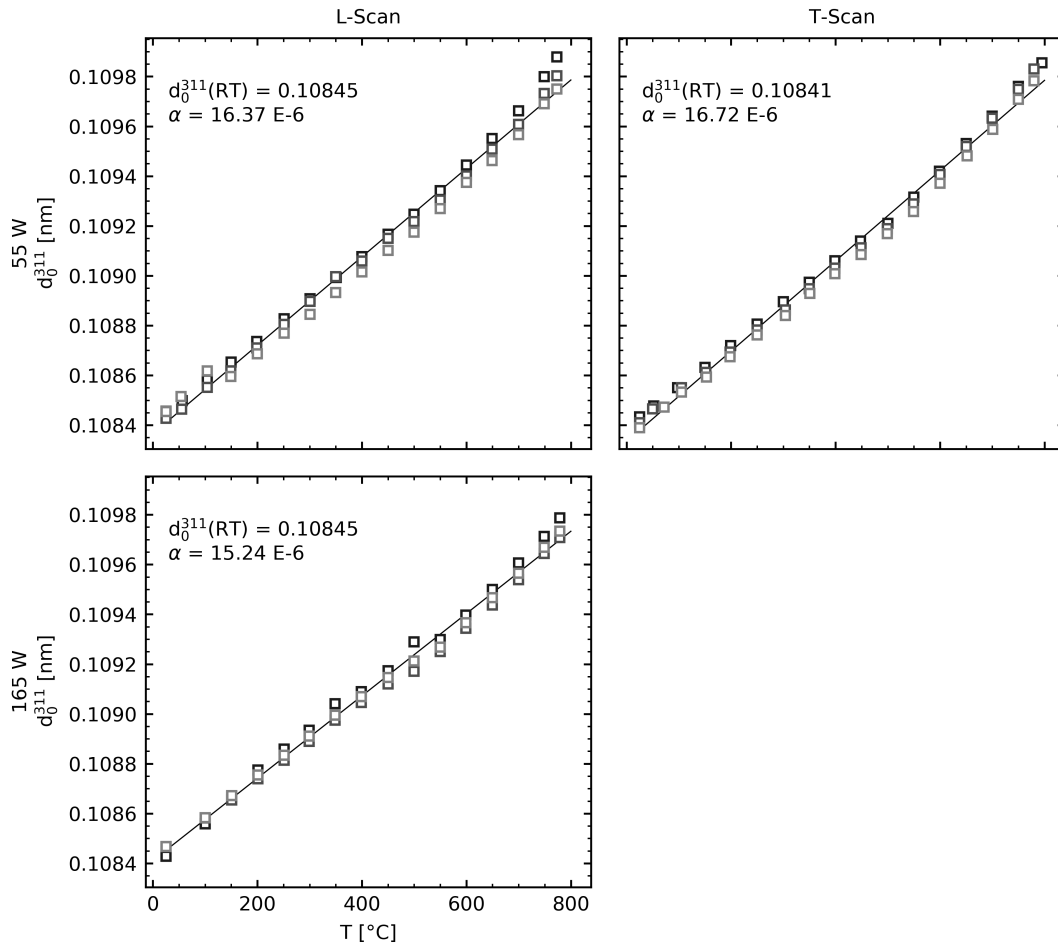


Figure P2.14: Results of temperature-dependent d_0 measurements.

P2.7.4 Temperature-dependent X-ray Elastic Constants

From Wang et al. the single crystal constants c_{11} , c_{12} and c_{44} for room temperature, 600 °C and 700 °C were used to calculate the corresponding Young's modulus and Poisson ratio via the Kröner model. Afterwards, those values were used for a linear regression to extrapolate to higher temperatures as shown in figure P2.15.

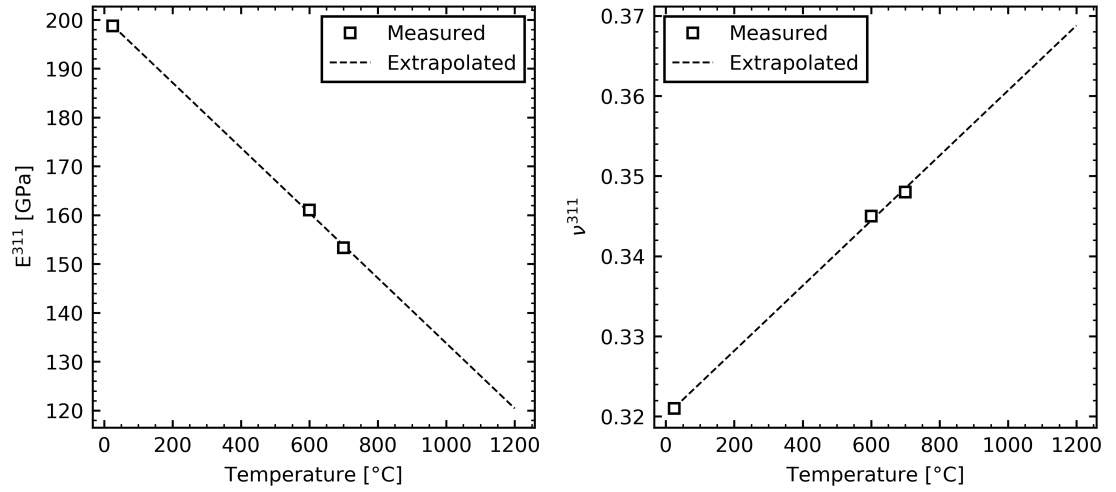


Figure P2.15: Calculated Young's modulus and Poisson ratio based on the single crystal constants determined by Wang et al. [48]. Extrapolation using a linear regression.

Table P2.2: Numerical values of elastic constants used for calculation of stresses in figure P2.9.

Temperature	Wang et al. [48]			Kröner	
	c_{11} [GPa]	c_{12} [GPa]	c_{44} [GPa]	E_{311} [GPa]	ν_{311}
25 °C	243.3	156.7	117.8	198.7	0.321
600 °C	214.8	153.1	101.1	161.0	0.345
700 °C	205.2	149.3	99.3	153.3	0.348

Extrapolation for Figure 9		
Temperature	E_{311} [GPa]	ν_{311}
300 °C	180.5	0.332
900 °C	140.4	0.357
1200 °C	120.4	0.369

P2.8 Using *in situ* experiments to understand the part-scale stress formation and distribution

Information

The following section was not published as part of the original article or its supplementary information.

The original article discussed the emergence of a stress maximum below the surface, found in the fifth layer in the center of the sample. After the initial increase to reach this maximum, the stresses dropped rapidly and approached zero. Since the original article was published, a second experiment with the same measurement mode was performed. Findings from that experiment regarding the texture evolution were already discussed in section P1.8. In the following section, the strains and stresses will be discussed.

As mentioned in section P1.8, the gauge volume was placed in the fifth layer, close to the left edge of the sample, where the laser exposure starts each layer. It was kept at the same position respective to the sample for the whole manufacturing process. Therefore, the material above the gauge volume is exposed by the laser directly at the beginning of each layer. In figure P2.16, the strain evolution in the transverse direction TD and the building direction BD in the gauge volume is shown similarly to the diagram in figure P2.5.

The first noticeable difference to the original figure is the time of the laser impact. It occurs right at the beginning of the exposure time and results in a steep increase of the lattice strains, which quickly drop again as the material cools down. Similar to figure P2.5 in the original article, the peak height is reduced with an increasing number of total layers due to the increased amount of material between the heat source and the gauge volume. Examination of the varying differences between TD and BD reveals a new phenomenon. While strains in TD are significantly higher than in BD at $n = 10$ layers, the difference between the two reaches has crossed zero at $n = 20$, where strains in BD are now higher than in TD. Starting from there, strains in TD continue to decrease, while strains in BD increase, resulting in an inversion of the strain difference that grows with more added layers.

Furthermore, the general progression of the strains changes with more added layers. While the strains in TD show a known evolution with a reduced but still discernible peak, there is no clear apex in BD after $n = 60$. Instead, the strains stay almost constant for the duration of laser exposure. This behavior is significantly different from the center of the sample, which is further reflected in the median stress difference, shown in figure P2.17. For this calculation of the stress difference, room-temperature d_0 and diffraction elastic constants were used. The remaining data evaluation was performed as described in the original article. Similarly to the centered gauge volume, figure P2.9, the maximum stress difference occurs early in the process and then decreases. While stresses in the center approach zero, at the edge gauge volume, zero is crossed at $n = 18$, and the stresses continue to decrease after. Indeed, the stress difference becomes more compressive with each added layer in an almost linear fashion, reaching about -250 MPa at the end of the manufacturing process.

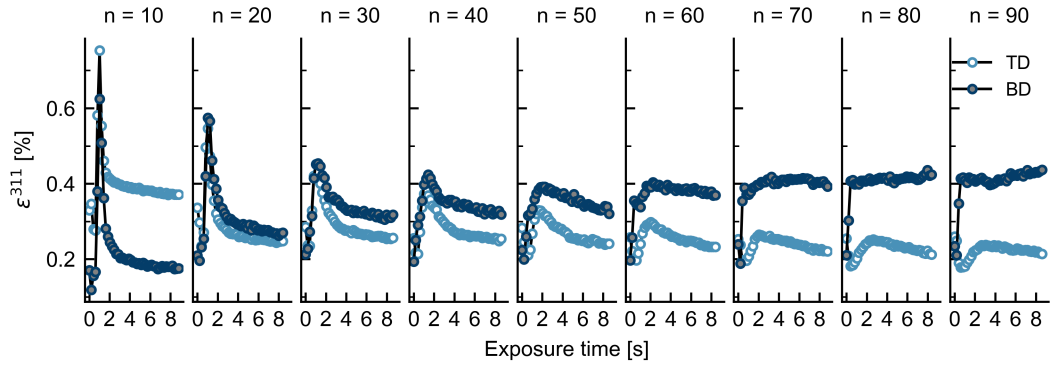


Figure P2.16: Strain progression with measuring position at the left edge of the sample. Each subplot shows the progression for one layer. The gauge volume was placed in the fifth layer, so the first subplot shows the strain progression with five additional layers above the gauge volume; in the second subplot, 15 layers are above the gauge volume and so on.

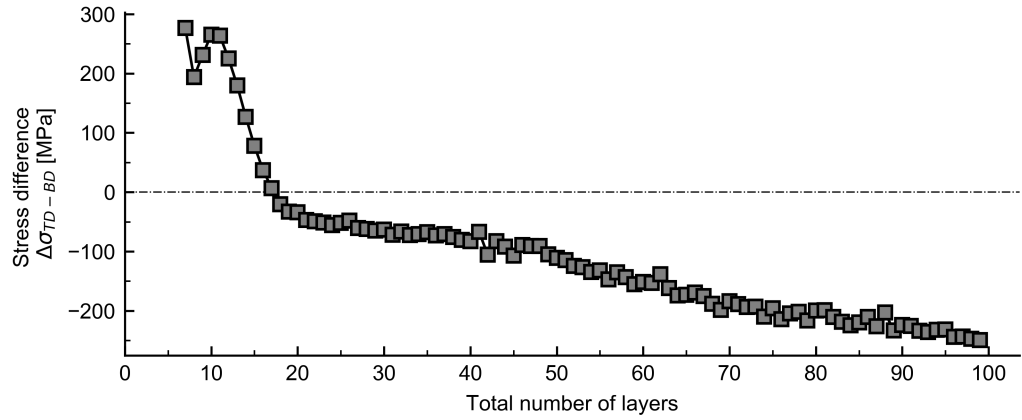


Figure P2.17: Layer-wise median stress difference σ_{TD-BD} for complete manufacturing process with the gauge volume placed at the left edge of the fifth layer of the sample.

In order to obtain an explanation for this behavior, multiple findings from the original article have to be combined. As a general boundary condition, the part as a whole needs to be in mechanical equilibrium. From the *in situ* experiments presented in the original article and the current section, we expect tensile stresses in the top layers of the part both at the edge and in the center. The analytical TGM model by Mercelis and Kruth also predicts this behavior. These tensile stresses need to be balanced by compressive stresses elsewhere to fulfill the mechanical equilibrium condition. The current section shows that these compressive stresses occur at the edge of the part with increasing distance to the top layer. As explained via figure P2.9, the center of the part close to the substrate experiences very low stresses at the end of the manufacturing process. The schematic drawing in figure P2.18 considers all of these three points to clarify the underlying mechanism for this mechanical response to adding multiple layers on a part-scale level. If the part were a free-floating beam, tensile stresses induced at the

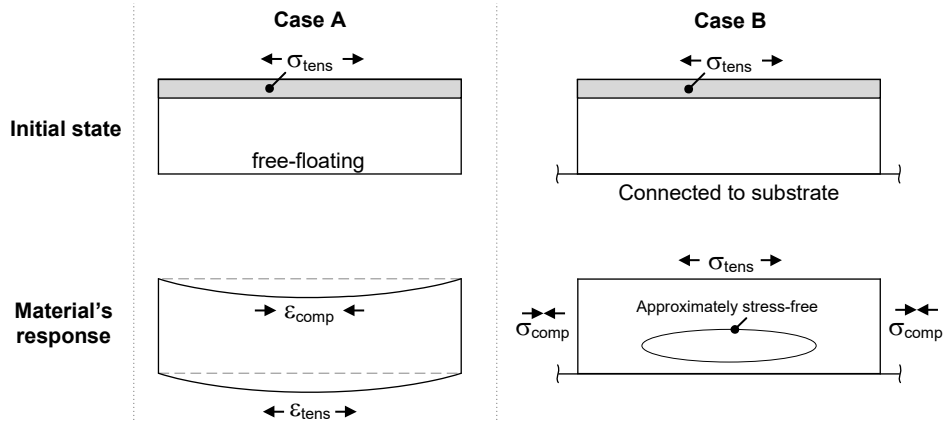


Figure P2.18: Schematic of part-scale stress response to tensile stresses in top layer.

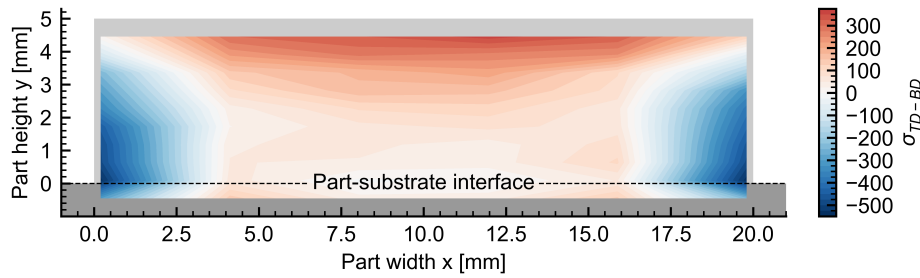


Figure P2.19: Stress distribution if a sample manufactured with a laser power of $P_L = 55 \text{ W}$, scanning speed of $v_L = 50 \text{ mm s}^{-1}$ and L-scanning.

top would result in a compressive strain, pulling the top together and resulting in an upwards curvature of the edges. Since the part is connected to the substrate, this curvature can not occur, which leads to the observed compressive stresses at the edges. As the top is in tension and the sides are in compression, the lower central part is close to stress-free. These interconnected mechanisms culminate in the final stress distribution shown in the lower right schematic in figure P2.18.

This mechanistic explanation was experimentally validated by measuring the two-dimensional stress distribution in the whole part *ex situ*. Via irradiation of 72 measuring locations in the final part, arranged in a 6×12 grid, with high-energy synchrotron radiation, the stress distribution shown in figure P2.19 was attained. This stress mapping was gathered from a sample manufactured with the same process parameters as the two experiments described in figures P2.9 and P2.17.

Figure P2.19 shows that the highest stresses occur close to the top surface, reaching more than 300 MPa for the given parameter set. At the sides of the sample, compressive stresses occur. The highest values of more than -500 MPa are reached at the interface to the substrate, close to the gauge volume position in figure P2.17. In the part's lower center, the fi-

nal stress difference is low, which is in agreement with the results presented in figure P2.9. Therefore, the *ex situ* stress distribution confirms the mechanistic approach described in this section.

In conclusion, a mechanistic description of the macroscopic stress formation in a cuboid part was derived from *in situ* diffraction experiments and strongly agreed with the measured *ex situ* stress distribution. These mechanisms, namely the stress inversion at the edge and a stress maximum below the top surface, occur for both materials under investigation in this thesis, further discussed in the next chapter.

P2.9 Implications and discussion of the alternative data evaluation approach reported by Aminforoughi et al.

Information

The following section was not published as part of the original article or its supplementary information. However, due to the thematic proximity of the original article to the paper under discussion, establishing the analysis here is deemed appropriate.

In 2021, Aminforoughi et al. published their article “A Novel Approach to Robustly Determine Residual Stress in Additively Manufactured Microstructures Using Synchrotron Radiation”, which deals with the difficulties of residual stress determination in LPBF-manufactured parts due to their unique microstructure and texture [Ami21].

According to the authors, „[t]he effect of local microstructural characteristics (such as texture, grain size, and morphology) on the experimentally determined strains seems to lead to miscalculations of the residual stresses using standardized approaches, such as Hooke’s approach“, which is the approach used in the present study. Therefore, they present a residual stress evaluation approach for analyzing 2D diffraction data acquired in transmission mode based on the $\sin^2 \psi$ method commonly used for laboratory X-ray diffraction experiments in reflection mode.

It is proposed to divide the full Debye-Scherrer ring into quarters and perform sector integration to determine azimuthally resolved lattice spacings, which are then converted into lattice strains. Subsequently, the ε_{hkl} values are plotted over $\sin^2 \alpha$ with α corresponding to the azimuthal angle called η in the present study. Linear regression is then performed for all quarters, yielding the gradient m of the curve, which they relate to the stresses following equation P2.1.

$$m_{\{hkl\}} = \frac{\partial \varepsilon_{\alpha}^{\{hkl\}}}{\partial \sin^2 \alpha} = \frac{1}{2} s_2^{\{hkl\}} \sigma_{22-33}^{\{hkl\}} = -\frac{1}{2} s_2^{\{hkl\}} \sigma_{33-22}^{\{hkl\}} \quad (\text{P2.1})$$

By using a large number of data points for the regression analysis, the authors improve the statistics and robustness of the residual stress analysis compared to only using two data points in what they refer to as Hooke’s approach in their publication, where simply the strains in the horizontal and vertical plane of the diffraction pattern are used for the stress analysis. Since the authors’ conclusion concerning the reliability of Hooke’s approach directly challenges this study’s findings, the present study’s data was reevaluated to compare both procedures.

Initially, a single diffraction pattern was analyzed as shown in figure P2.20a. As described in the manuscript, Hooke’s approach is based on determining the lattice spacings in transverse direction TD and building direction BD, taking into account both opposite sectors of the diffraction

pattern. The difference of both averages is calculated and converted into a stress value following equation P2.2¹. Hooke's approach resulted in a stress difference of $\Delta\sigma = 338 \pm 10$ MPa for this diffraction pattern.

$$\Delta\sigma_{TD-BD} = \frac{1}{2}s_2 \left(\frac{d_{TD} - d_{BD}}{d_0} \right) \quad (\text{P2.2})$$

The $\sin^2 \alpha$ approach was executed as prescribed by the authors except for using 5° sectors instead of 2° sectors. For each sector, the (311) reflection lattice spacing was determined to calculate the corresponding lattice strain using a room-temperature $d_0 = 0.10845$ nm for the sake of simplicity. Then, the lattice strains were plotted over $\sin^2 \alpha$ with a slight variation to the definition of α . While Aminforoughi et al. defined $\alpha = 0^\circ$ in the direction of $d_{BD,1}$ in this study with a positive rotation in clockwise direction, here, it is defined as corresponding to the direction of $d_{TD,1}$ with the positive sense of rotation being counter-clockwise. This redefinition was used to comply with the present study's terminology and does not impact the interpretation.

For each quarter and the diffraction pattern altogether, a simple linear regression was performed as described in the article, figure P2.20b. From the gradient of the linear function, the stress could then be calculated following equation P2.1. This approach resulted in a stress of $\Delta\sigma = 331 \pm 20$ MPa, only a 2 % difference to Hooke's approach.

However, a single diffraction pattern has limited meaningfulness for comparing the reliability and robustness of the two approaches. Therefore, the dataset used for figure 9, section P2.3.4 in the present study was analyzed again using the procedure described above. The result is shown in figure P2.21. It has to be noted that for the sake of simplicity, the temperature dependence of the stress values was neglected for this figure since it would impact both approaches the same way. Therefore, room-temperature data was used for the elastic constants and d_0 .

First, both data evaluation approaches produce the same general progression of the stress difference. Both show a steep initial increase in the stresses, a maximum at 11-13 layers followed by a steep decrease that tapers off after about 30 layers. The curve for the $\sin^2 \alpha$ approach looks much smoother than the other one, which is interesting since both curves have been statistically smoothed as they represent the median stress for each layer. The bottom plot shows the deviation between the two curves in absolute stress values. These deviations range from -40 MPa to 30 MPa with the Hooke's approach producing higher stress values initially and then dropping below the other curve after the steep decline.

To conclude, the two approaches do result in partially different stress values. The $\sin^2 \alpha$ approach produces a smoother curve, which reaches its maximum at 13 layers compared to 11 layers for Hooke's approach. However, the general trends and progression are the same, and

¹This form of the equation is equivalent to the slightly more convoluted version in the manuscript, equation 3 in section P2.2.6

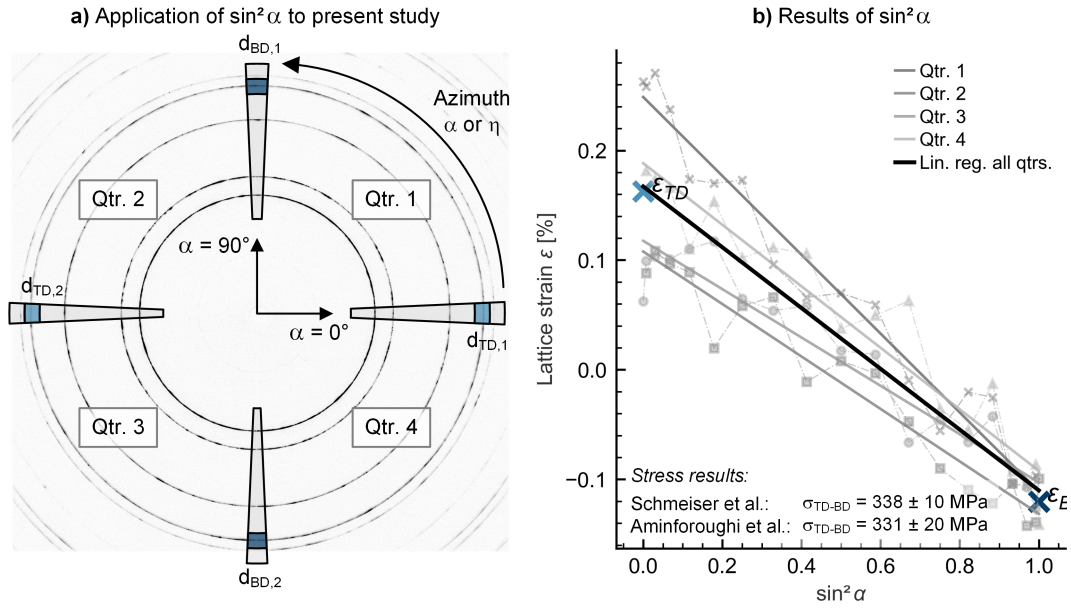


Figure P2.20: Application of $\sin^2 \alpha$ approach to a single diffraction pattern. a) Schematic of diffraction pattern and evaluated sectors. b) Results of linear regression following $\sin^2 \alpha$ approach and of Hooke's approach

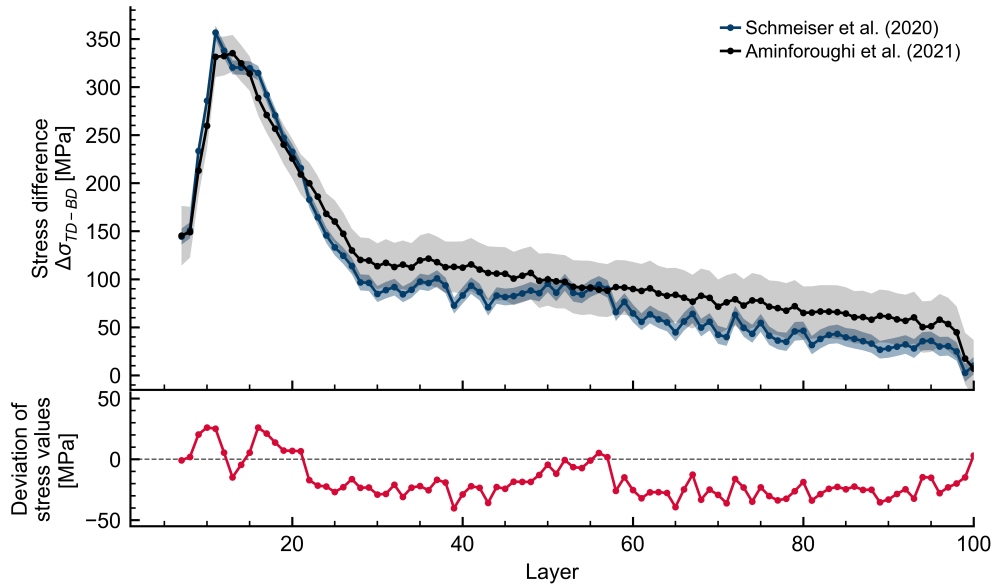


Figure P2.21: Progression of stress difference and associated error in a constant gauge volume corresponding to section P2.3.4 using both $\sin^2 \alpha$ and Hooke's approach. Bottom plot shows deviation between the two curves.

the conclusions presented in section P2.3.4 remain unchanged. While the highest possible precision of the absolute stress values is, of course, desirable, it is not given top priority in the case of the *in situ* diffraction experiments presented in this thesis. Here, the basic phenomena and mechanisms of the formation and evolution of stresses in LPBF are of interest, and the choice of data evaluation approach does not seem to impact these findings, based on what has been presented in this section. Additionally, further factors complicate the calculation of stresses that have not been discussed so far, especially the temperature of the material in the gauge volume, which will be tackled in the following chapter and is likened to have a more noticeable impact on the absolute stress values than the data evaluation approach.

Aminforoughi et al. do raise several essential points regarding the stress evaluation for LPBF-manufactured samples, though, especially concerning the LPBF-specific microstructure. In the sample that has been discussed here, however, these concerns can be alleviated. Due to the chosen laser parameters, the material exhibited only a weak crystallographic texture, see chapter P1, and presented with a fine-grained microstructure in *ex situ* metallographic investigations not shown here. As mentioned by the authors, these are two of the main causes for inaccuracies in residual stress determination.

Internal Stress Evolution and Subsurface Phase Transformation in Titanium Parts Manufactured by Laser Powder Bed Fusion — An In Situ X-Ray Diffraction Study

Unlike the first two publications, the third study used commercially-pure titanium grade 1 as a powder feedstock material. As discussed in section 2.1.5.2, commercially-pure titanium grade 1 experiences a phase transformation at elevated temperatures. The impact depth of the laser impact on subsurface phase transformations is examined in the following article. Additionally, stress-related spatial phenomena will be discussed based on stress differences similarly to chapter P2.

The article presents one significant innovation: The *in situ* determination of absolute stress values during LPBF. Next to precise knowledge of d_0 , the temperature of the gauge volume is a vital factor for accurate stress calculations. Therefore, an approach to approximate these temperatures was devised considering the interplay of increased temperatures and reduced strength. The phase transformation temperature was used as an internal validation tool for the approximations.

Due to the feedstock powder's purity, the extensive experimental d_0 determination carried out for Inconel 625 can be avoided, and the temperature approximations are used to calculate temperature-dependent d_0 values based on the thermal lattice expansion based on a powder d_0 . These considerations enable calculating absolute *in situ* stress values for the first time in LPBF research.

Bibliographic data	
Title	Internal Stress Evolution and Subsurface Phase Transformation in Titanium Parts Manufactured by Laser Powder Bed Fusion — An In Situ X-Ray Diffraction Study
Authors	<i>Felix Schmeiser</i> , Erwin Krohmer, Norbert Schell, Eckart Uhlmann, Walter Reimers
Journal	Advanced Engineering Materials
Publisher	Wiley VCH
Publication Date	26th May 2021
Reference	Advanced Engineering Materials 23 (2021): 2001502
DOI	10.1002/adem.202001502
My contribution	Planning, executing, and evaluating the <i>in situ</i> LPBF diffraction experiments at PETRA III; Data analysis, interpretation, visualization; Writing the manuscript

The manuscript is inserted in the following pages. The article is reprinted under the open access CC BY license (<https://creativecommons.org/licenses/by/4.0/>)

Internal Stress Evolution and Subsurface Phase Transformation in Titanium Parts Manufactured by Laser Powder Bed Fusion—An In Situ X-Ray Diffraction Study

Felix Schmeiser,* Erwin Krohmer, Norbert Schell, Eckart Uhlmann, and Walter Reimers

Laser powder bed fusion (LPBF) is a metal additive manufacturing technology, which enables the manufacturing of complex geometries for various metals and alloys. Herein, parts made from commercially pure titanium are studied using in situ synchrotron radiation diffraction experiments. Both the phase transformation and the internal stress buildup are evaluated depending on the processing parameters. For this purpose, evaluation approaches for both temperature and internal stresses from in situ diffraction patterns are presented. Four different parameter sets with varying energy inputs and laser scanning strategies are investigated. A combination of a low laser power and scanning speed leads to a more homogeneous stress distribution in the observed gauge volumes. The results show that the phase transformation is triggered during the primary melting and solidification of the powder and subsurface layers. Furthermore, the stress buildup as a function of the part height during the manufacturing process is clarified. A stress maximum is formed below the part surface, extending into deeper layers with increasing laser power. A temperature evaluation approach for absolute internal stresses shows that directional stresses decrease sharply during laser impact and reach their previous magnitude again during cooling.

1. Introduction

Additive manufacturing technologies offer vast possibilities for lightweight design, which appeal to medical and aerospace engineering fields, among other industry branches. In the case of metal part production, laser powder bed fusion (LPBF), which is also referred to as selective laser melting (SLM), is one of the most widely used additive manufacturing technologies due to the geometrical freedom in design while benefiting from relatively good mechanical properties in comparison with conventionally manufactured parts.


While industrial sectors such as medical technology and aviation may greatly benefit from the geometric freedom of design, they also impose high quality and safety standards that, to date, often cannot be met by additive manufacturing technologies. A lack of process knowledge and control over LPBF is expressed in the formation of defects and residual stresses that harm the components' mechanical behavior.^[1,2] In LPBF, a thin layer of metal powder of typically 30–50 µm is deposited on a solid substrate plate and locally melted by a focused laser beam according to the part's cross-sectional model. Subsequently, a new powder layer is deposited and melted, such that a bond is formed with the solidified layers beneath. This procedure is repeated layer by layer until completion of the part. A complex heat flux with steep temperature gradients is generated for every layer, varying with the material, laser scanning parameters,^[3] built height,^[4] part geometry,^[5] and due to heat accumulation within a single layer.^[6] In turn, a complex stress development occurs with several overlapping, stress-inducing mechanisms introduced by Mercelis and Kruth.^[7] The thermal gradient mechanism (TGM) describes how the exposed material is rapidly heated and plasticized during laser–matter interaction. Colder material below inhibits the thermal expansion of the heated material, resulting in compressive stresses. After laser exposure, the material cools down, and the surrounding material hinders its thermal shrinkage. Schmeiser et al.^[8] experimentally showed that the hindered thermal shrinkage has a much stronger influence on in-plane stresses than out-of-plane stresses. Furthermore, they showed that tensile stresses, as described by Mercelis and Kruth,^[7] are formed in the working plane, whereas in the out-of-plane, those tensile stresses result in a transverse contraction.

F. Schmeiser, Prof. W. Reimers
Institute for Materials Science and Technology
Metallic Materials
Technische Universität Berlin
Ernst-Reuter-Platz 1, 10587 Berlin, Germany
E-mail: felix.schmeiser@tu-berlin.de

E. Krohmer, Prof. E. Uhlmann
Institute for Machine Tools and Factory Management (IWF)
Technische Universität Berlin
Pascalstraße 8-9, 10587 Berlin, Germany

Dr. N. Schell
Institute of Materials Physics
Helmholtz-Zentrum Hereon
Max-Planck-Str. 1, 21502 Geesthacht, Germany

Prof. E. Uhlmann
Fraunhofer Institute for Production Systems and Design Technology (IPK)
Pascalstraße 8-9, 10587 Berlin, Germany

 The ORCID identification number(s) for the author(s) of this article can be found under <https://doi.org/10.1002/adem.202001502>.

© 2021 The Authors. Advanced Engineering Materials published by Wiley-VCH GmbH. This is an open access article under the terms of the Creative Commons Attribution License, which permits use, distribution and reproduction in any medium, provided the original work is properly cited.

DOI: 10.1002/adem.202001502

Numerous studies on the influence of laser scanning parameters on residual stress development can be found in the literature and are summarized in the current review articles on residual stresses in LPBF.^[9,10] While researchers agree that the laser scanning parameters significantly influence the residual stresses, different results can be found regarding the degree of impact of the individual parameters.^[11] Mukherjee et al.^[12] deduced from their thermal simulations that low heat input is favorable for reducing thermal strain in the part. Therefore, the laser power should be chosen as low as possible and the scanning speed as high as possible while maintaining good interlayer bonding of the material, which is in line with a study from Ali et al.^[13] They showed that considering a constant energy density level, combinations of lower laser power and higher exposure time result in lower residual stresses for Ti-6Al-4V specimens. However, other research results seemingly showed contradictory findings that residual stresses decrease with increasing laser power.^[14,15]

Further experimental results on additively manufactured 316L parts using neutron diffraction revealed that deflection induced by residual stresses could be reduced using higher ratios of laser power to scanning speed.^[16] The impact of laser scanning parameters on residual stresses also involves the length and sequence of individual scan lines that form the melt track. Studies have shown that shortening the scan vector length reduces residual stresses for simple unidirectional or alternating scan strategies.^[3,17] Moreover, the highest residual stresses occur parallel to the scan vectors.^[3,18–20] However, for more complex scan strategies, such as island scanning again, contradictory results can be found in the literature, concerning the effect of reducing the scan vector length.^[18,21] Xiao et al.^[11] conclude that the complex relationship between laser scanning parameters and residual stress could be the reason for the contradictory parametric effects reported in the literature. Hence, for a profound process understanding, in situ measurement techniques are needed to extend the knowledge about the impact of process parameters on internal stress evolution during the manufacturing process.

Additively manufactured titanium and its alloys are of particular interest to aerospace technology^[22] as well as medical technology^[23] or even for musical instruments.^[24] Titanium goes through a phase transformation at $T = 882^\circ\text{C}$, where the lattice changes from a hexagonally close-packed (hcp) to a body-centered cubic (bcc) lattice. This transformation entails a slight volume contraction.^[25] The two lattices share a lattice plane, the (200) for the α hcp phase, and the (110) for the β bcc phase.

In LPBF, the powder material goes through the phase transformation during laser exposure, as it is melted and solidified as a melting track. Gu et al.^[26] observed the correlation of phase transformation with the scanning speed on commercially pure titanium grade 2. They observed the formation of martensitic α' phase for scanning speeds $v_L \geq 200\text{ mm s}^{-1}$ and a laser power of $P_L = 90\text{ W}$, and the formation of α phase for a scanning speed $v_L = 100\text{ mm s}^{-1}$. These observations are consistent with the studies by Attar et al.^[27] Essentially, the choice of the laser parameters can alter the cooling and solidification rate and, therefore, the resulting microstructure^[28] and phase composition^[26] depending on the processed material.

Phase transformations have been captured by in situ X-ray diffraction experiments by several research groups^[29–31] with

the constraint of observing the top layer of the part, powder bed, or the substrate only. Dye et al.^[32] used neutron diffraction to observe phase transformations and evaluate absolute stresses during the welding of mild steel. An in situ study under LPBF conditions investigating subsurface phase transformations and stress evolution in multilayer parts is missing to date.

In this study, comprehensive in situ X-ray diffraction experiments with synchrotron radiation were carried out to elucidate the phase transformation dynamics and internal stress development in commercially pure titanium grade 1 (cp-Ti) in subsurface layers using a variety of process and laser scanning parameters. A temperature evaluation approach is introduced to present absolute in situ stress values during LPBF for the first time.

2. Results and Discussion

For the experiments' conduction at the P07 beamline^[33] at Deutsches Elektronen-Synchrotron (DESY), Hamburg, Germany, a custom-made LPBF system was used. This system was designed by Uhlmann et al.^[34] to enable the examination of LPBF parts, as they are being built layer by layer using high-energy synchrotron radiation. Thin cuboid parts were produced from 120 equally processed cp-Ti powder layers, resulting in the final part dimensions of about 21 mm in length, 2.5 mm in width, and 6 mm in height. The parts were built on titanium grade 2 substrate plates.

During the processing of the sample layer by layer, 2D diffractograms were recorded, as the sample was irradiated by the monochromatic synchrotron radiation beam in transmission mode; see **Figure 1a**. Different locations in the sample were observed to gain temporal and spatial insights into the dynamics of the thermally induced stresses and phase transformations in the bulk material. The gauge volume (GV) was positioned either at the left edge or in the center in the lateral sample direction. In the buildup direction, GV distances z_{GV} from 0 to 1 mm in the steps of 0.2 mm were observed. The GV distance z_{GV} is denoted as the distance from the GV to the working plane in which the current layer is processed; see **Figure 1b**.

For every layer, the powder bed surface was scanned by the laser with a spot size of $\approx 60\text{ }\mu\text{m}$ either longitudinally (L-Scan) or transversely (TI-Scan) regarding the incident synchrotron radiation beam; see **Figure 2**. After processing a layer, a new powder layer was deposited by an automatic powder coating mechanism. This recoating mechanism is designed to maintain a constant working distance from the laser to the powder bed.

Different parameter sets of laser power P_L and scanning speed v_L were used to study their impact on subsurface phase transformation and stress formation during the LPBF process. The transmission or longitudinal direction of the synchrotron radiation beam is denoted by LD; the layer buildup direction is denoted by BD, and the remaining axis is denoted by TD.

2.1. Evaluation of Diffraction Patterns

One of this study's main objectives is determining internal stresses during the manufacturing process utilizing high-energy X-ray diffraction. The diffraction results deliver, among other things, information regarding the lattice spacing of the

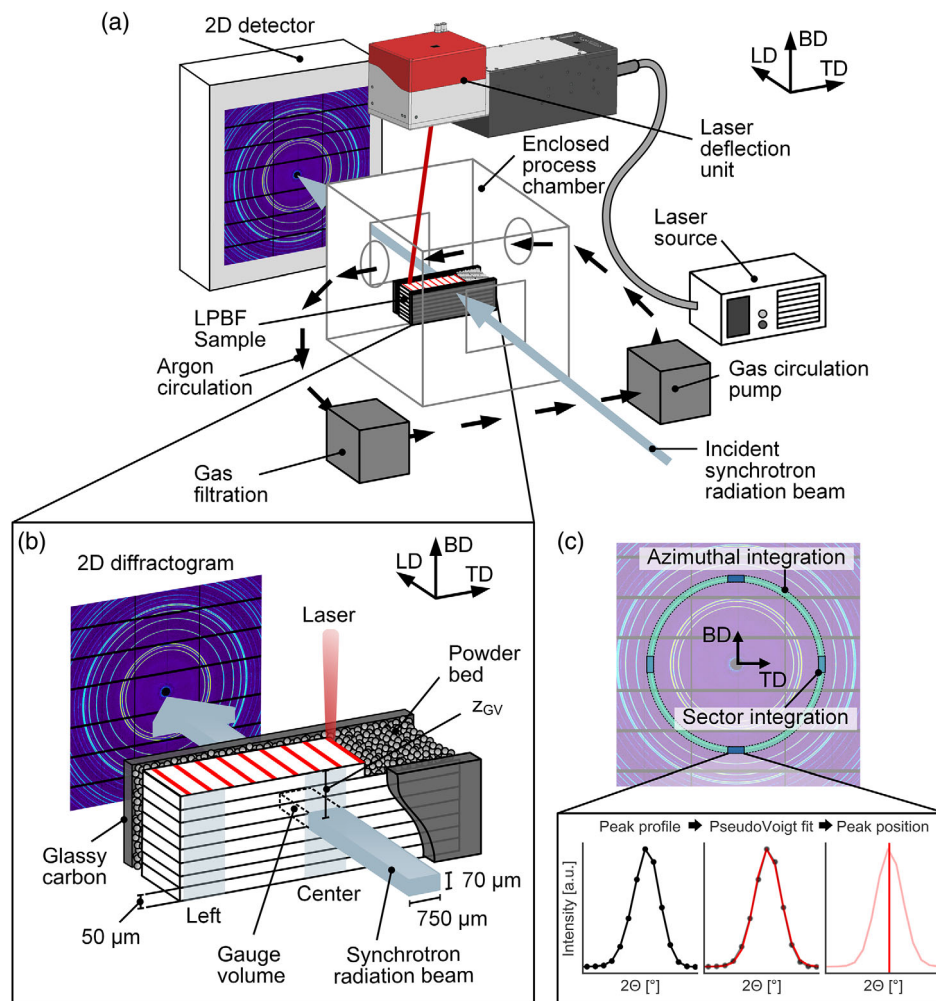


Figure 1. Schematic of the experiment: a) Experimental setup. b) Sample environment and measurement locations. c) Data evaluation.

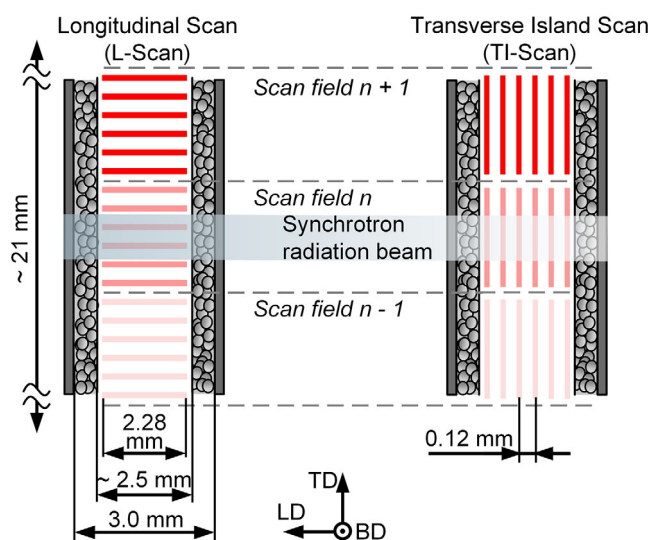


Figure 2. Scanning patterns used to fabricate samples.

crystalline material; see Figure 1c. In situ experiments using monochromatic synchrotron radiation offer several benefits: fast acquisition rates, high photon flux, and high penetration depths. A significant drawback is the lack of data in beam direction LD, which means that both strains and stresses in beam direction cannot be determined. As the stress in beam direction influences the strains in the two other normal directions, TD and BD, suitable assumptions regarding the stress state must be formulated to calculate stress values. For the given experimental setup, the parts produced had their smallest dimension in beam direction with a thickness of about 2.5 mm, whereas the width of the parts was about 21 mm, and the height was about 6 mm. Residual stresses are generally the lowest in the smallest part dimension, which is supported by simulative results by Chen et al.^[35] In addition, the substrate has about the same thickness as the parts, 3 mm, whereas its width is about 70 mm. It follows that the substrate inhibits strains in TD but not in LD, allowing the material to relax in LD. Consequently, Chen et al. found little to no deformation in thickness direction.^[35] For these reasons, a biaxial stress state is assumed where the stress in beam direction is approximated as $\sigma_{LD} = 0$ MPa. Following this boundary condition, the elastic

strains measured in the plane normal to the incident beam direction are solely the result of stresses in the same plane.

2.1.1. Stress-Free Lattice Spacing d_0

Another central prerequisite for absolute stress determination is the precise knowledge of the stress-free lattice spacing d_0 . The stress calculation is extremely sensitive to this value, and the determination of d_0 poses a challenge of its own, especially for LPBF materials.^[36,37] In this study, accurate d_0 values were gathered by collecting diffraction patterns of the primary powder material inside the process chamber under an inert gas atmosphere as part of the regular experimental procedure. The same beam apertures and exposure parameters were used to ensure consistency in the diffraction patterns.

Changes in elemental composition due to vaporization during laser-matter interaction, which would impact the stress-free lattice spacing, do not occur in cp-Ti due to the lack of alloying elements. By azimuthal integration and subsequent fitting, a room temperature stress-free lattice spacing $d_{0,\text{powd}} = 1.726280 \pm 0.000033 \text{ \AA}$ was found. Also, the room temperature lattice parameters a and c were determined by analyzing additional peaks.

2.1.2. Temperature Evaluation

The lattice spacing is influenced by both the temperature and internal stresses of the material. Decoupling these two factors is central to determine accurate internal stress values. In LPBF, the focused heat input results in steep thermal gradients and a rapidly, continuously changing temperature distribution. With the given experimental setup, temperature gradients in the GV cannot be determined. For a single diffraction pattern, a single temperature, representing the average temperature in the GV, is, therefore, used for the stress calculation.

The lattice spacings corresponding to the two principal stress directions of interest, TD and BD, are affected by the thermal strain of equal magnitude. During the laser exposure of a single

layer, the lattice spacings show a characteristic progression with a steep increase, as the laser reaches and scans over the GV, followed by a sharp decline that tapers off; see Figure 3a. This progression shows a maximum when the laser has reached the GV, indicating that this strain maximum coincides with the maximum temperature.

A temperature increase coincides with a reduction of the mechanical properties, especially strength. At 600 °C, pure titanium's ultimate tensile strength is only 10% of its room temperature magnitude.^[38] Similarly, the yield stress decreases drastically with increasing temperature.^[39] A combination of lowered strength and high internal stress leads to plastic deformation and stress relief.

Therefore, the lattice strain at the peak d_{max} is regarded as purely thermal and allows the temperature calculation, Equation (2), via the thermal expansion, Equation (1). The observation of β reflections at the peak supports that assumption and indicates that at least parts of the GV have reached temperatures even above 882 °C.

$$\varepsilon_{\text{th}} = \frac{d_{\text{max}} - d_{0,\text{powd}}}{d_{0,\text{powd}}} = \alpha \times \Delta T \quad (1)$$

$$T = 25 \text{ °C} + \frac{1}{\alpha} \times \frac{d_{\text{max}} - d_{0,\text{powd}}}{d_{0,\text{powd}}} \quad (2)$$

The (102) lattice plane-specific coefficient of thermal expansion (CTE) was derived from the lattice parameter-dependent expansion equations reported by Medoff and Cadoff^[40] (Equation (3) and (4)).

$$a(T) = a_{\text{RT}} \times [1 + 9.928 \times (T - 25) \times 10^{-6} - 0.626 (T - 25)^2 \times 10^{-10}] \quad (3)$$

$$c(T) = c_{\text{RT}} \times [1 + 11.079 \times (T - 25) \times 10^{-6} - 9.698 (T - 25)^2 \times 10^{-10}] \quad (4)$$

As the quadratic term is four orders of magnitude smaller than the linear term, a linear approximation for the (102) CTE was used

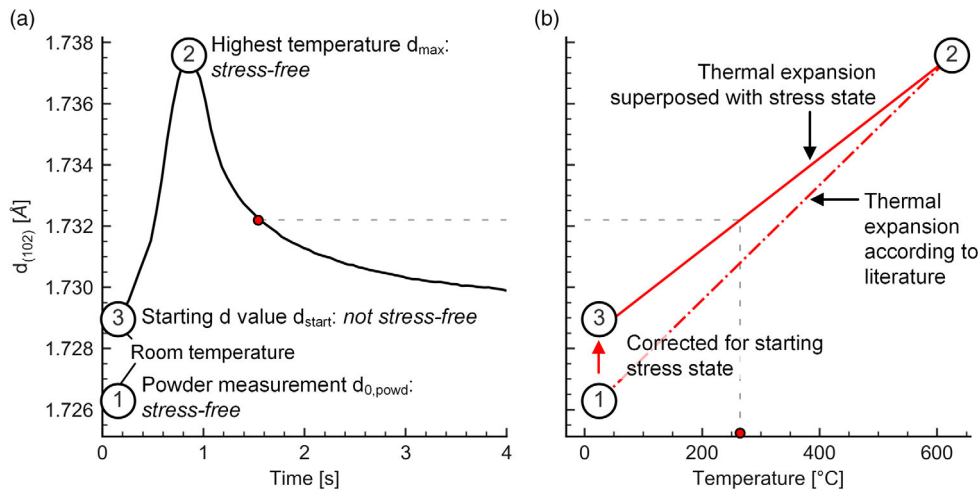


Figure 3. Temperature evaluation procedure: a) Lattice spacing progression during laser exposure. b) Temperature calculation based on characteristic lattice spacings.

and found to be equal to $\alpha(102) = 10.89 \times 10^{-6} \text{ K}^{-1}$. Using this CTE, the powder d_0 as a room temperature reference, and the peak d_{max} value in a layer, the maximum temperature for the corresponding layer was calculated based on the assumption that the material is stress-free at the peak; see Figure 3b. It was observed that the starting azimuthal d values were higher than d_0 , demonstrating tensile stresses at room temperature in the GV. Therefore, the temperature calculation was adjusted for the starting stress state by interpolating temperatures between the $d_{\text{start}}(T = 25^\circ\text{C})$ and $d_{\text{max}}(T = T_{\text{max}})$. This correction reflects the relaxation of stresses at higher temperatures. Considering this correction, the GV's temperature progression was calculated for every diffraction pattern in the sequence based on the azimuthal d values.

2.1.3. Internal Stress Calculation

The obtained temperatures were then used to calculate the stress-free lattice spacing $d_0(T)$ and the X-ray elastic constants (XECs) for each temperature. XECs are elastic constants for a specific lattice plane. They reflect the crystal anisotropy but, just like the macroscopic Young's modulus and Poisson ratio, are temperature-dependent. The temperature-dependence was derived from the single crystal moduli reported by Fisher and Renken^[41] using an Eshelby–Kröner model and linear regression.

For every diffraction pattern, a sector integration in the two assumed principal stress directions TD and BD was performed; see Figure 1c. Subsequently, stress values were calculated in two ways: stress differences between TD and BD and absolute stress values.

The stress difference is robust against uncertainties in d_0 and temperature. Also, potential stresses in LD do not affect the stress difference $\sigma_{\text{TD}} - \sigma_{\text{BD}}$. The stress difference was calculated by the following equation.

$$\sigma_{\text{TD}} - \sigma_{\text{BD}} = \frac{1}{\frac{1}{2}s_2(T)} \left[\frac{d_{\text{TD}} - d_{\text{BD}}}{d_0(T)} \right] \quad (5)$$

For calculating absolute stresses, first, the lattice strains ϵ_{TD} and ϵ_{BD} were calculated by the following equations.

$$\epsilon_{\text{TD}} = \frac{d_{\text{TD}} - d_0(T)}{d_0(T)} \quad (6)$$

$$\epsilon_{\text{BD}} = \frac{d_{\text{BD}} - d_0(T)}{d_0(T)} \quad (7)$$

Subsequently, the lattice strain ϵ_{LD} was derived from the generalized Hooke's law,^[42] Equation (8), following the premise $\sigma_{\text{LD}} = 0 \text{ MPa}$.

$$\sigma_{\text{LD}} = 0 \text{ MPa} = \frac{1}{\frac{1}{2}s_2(T)} [\epsilon_{\text{LD}} - C \times (\epsilon_{\text{LD}} + \epsilon_{\text{TD}} + \epsilon_{\text{BD}})] \quad \text{with} \quad (8)$$

$$C = \frac{s_1(T)}{\frac{1}{2}s_2(T) + 3s_1(T)}$$

$$\epsilon_{\text{LD}} = \frac{C}{1 - C} (\epsilon_{\text{TD}} + \epsilon_{\text{BD}}) \quad (9)$$

Absolute stress values σ_{TD} and σ_{BD} were then determined by the following equations.

$$\sigma_{\text{TD}} = \frac{1}{\frac{1}{2}s_2(T)} [\epsilon_{\text{TD}} - C \times (\epsilon_{\text{TD}} + \epsilon_{\text{BD}} + \epsilon_{\text{LD}})] \quad (10)$$

$$\sigma_{\text{BD}} = \frac{1}{\frac{1}{2}s_2(T)} [\epsilon_{\text{BD}} - C \times (\epsilon_{\text{TD}} + \epsilon_{\text{BD}} + \epsilon_{\text{LD}})] \quad (11)$$

Uncertainty evaluations are based on the standard deviation of the center parameter of the PseudoVoigt fitting function for both azimuthal and sector integrations.

2.2. Direct Observation of High-Temperature β Phase

While a quantitative analysis of the phase transformation requires azimuthal integration and peak fitting, a look at the raw diffraction patterns provides considerable insight into some of the dynamics during the transformation. In Figure 4, a time sequence of diffraction pattern excerpts is given for a sample manufactured with a laser power of $P_L = 55 \text{ W}$ and longitudinal scanning. All the patterns show the same section of the full diffraction pattern. For each pattern, the elapsed time Δt is given, measured from the start of laser exposure. Below the diffraction pattern, a top view visualization of the sample and the laser progression is shown together with the synchrotron GV. The individual scan tracks and their relation to both the synchrotron GV in combination with the above-mentioned temperature values give an impression of the sample's thermal management.

In LPBF, the rapid laser–matter interaction results in the high cooling rates up to $10^7 \text{ }^\circ\text{C s}^{-1}$.^[43] Therefore, the phase transformation of cp-Ti is highly dynamic and occurs on short timescales but is still captured by our measurements. The first image shows the start of the layer. Only α phase reflections are visible, and the temperature is $T_{\text{GV}} = 25^\circ\text{C}$. At $\Delta t = 0.48 \text{ s}$, a weak $\beta(200)$ reflection emerges, as the calculated temperature has reached $T_{\text{GV}} = 354^\circ\text{C}$, much lower than the phase transformation temperature of 882°C . This discrepancy is caused by significant thermal gradients in the GV. While the material surrounding the laser spot, which has barely reached the synchrotron GV, is heated above the transformation temperature, the rest of the volume remains at a much lower temperature, resulting in the given calculated temperature.

The $\beta(200)$ reflection becomes more prominent in the following images and disappears again at $\Delta t = 0.86 \text{ s}$. At the same time, splitting at the $\alpha(002)/\beta(110)$ reflection is visible. These reflections have very close peak positions, because it is a shared lattice plane the phase transformation occurs at. The splitting is most prominent at $\Delta t = 0.81 \text{ s}$.

Furthermore, the emergence of a prominent β spot is visible once the GV temperature reaches $T_{\text{GV}} = 613^\circ\text{C}$ at $\Delta t = 0.70 \text{ s}$. The spot's orientation and intensity slightly change, as the laser moves over the GV. The temperature threshold for the β spot to disappear was $T_{\text{GV}} = 382^\circ\text{C}$ at $\Delta t = 1.08 \text{ s}$. Therefore, this large β spot was stable for about 0.4 s , implying that at least part of the GV had a temperature above the phase transformation temperature of 882°C for that time. The difference in temperatures between the spot's appearance and vanishing shows the delay of heat conduction inside the synchrotron GV. While the

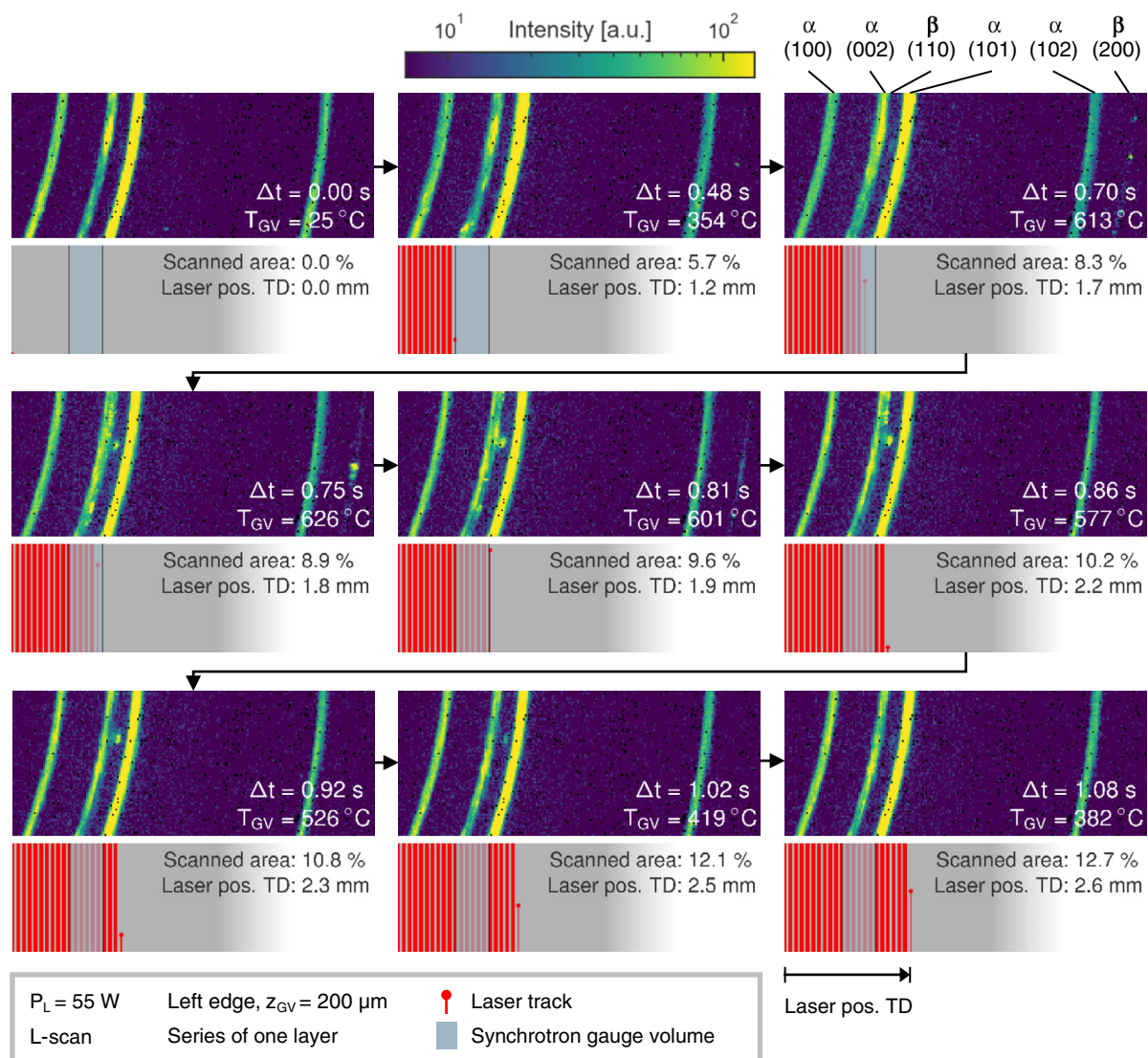


Figure 4. Phase transformation of titanium during LPBF observed in a time series of diffraction pattern excerpts. For each timestamp, the corresponding position of the laser beam and the calculated GV temperature are given.

calculated temperature reached its maximum at $\Delta t = 0.70$ s, the spot's maximum intensity occurred at $\Delta t = 0.81$ s, where the temperature had already decreased slightly to $T = 601$ °C. The duration of the large β spot's appearance corresponded to the laser exposing less than nine hatches, creating an exposed area about 0.9 mm in width.

It is important to note that the GV for Figure 4 is positioned $200 \mu\text{m}$ below the surface of the powder bed to observe previously solidified layers. Therefore, this figure is a visual example that, during LPBF, it is not only the powder layer that experiences the phase transformation during melting and cooling. Even three layers below the surface, in this case, the material reaches the transformation temperature. However, the data do not show that all of the GV reaches the transformation temperature simultaneously or has a constant temperature. The diffraction patterns represent an integrated result over all the grains in the GV. Temperature gradients in the GV cannot be depicted directly.

2.3. Phase Transformation Penetration Depth

Figure 5 compares the effect of the two different scanning patterns on the peak shift for a laser power $P_L = 55$ W. For each scanning pattern, different GV positions z_{GV} with increasing distance to the powder bed's top surface are shown. For the distance $z_{GV} = 0 \mu\text{m}$, the GV was located in the currently processed powder layer, whereas a distance $z_{GV} = 200 \mu\text{m}$ equals three layers beneath the currently processed powder layer. While raw diffraction data were analyzed in the previous section, diffraction patterns were fully azimuthally integrated to show the diffracted peaks' progression during the laser exposure of a single layer here.

Figure 5a shows the phase transformation most clearly. As the laser scans over the GV, a peak shift to lower diffraction angles is visible first before the α peaks vanish completely, and only β peaks remain. The peak shift represents a lattice expansion

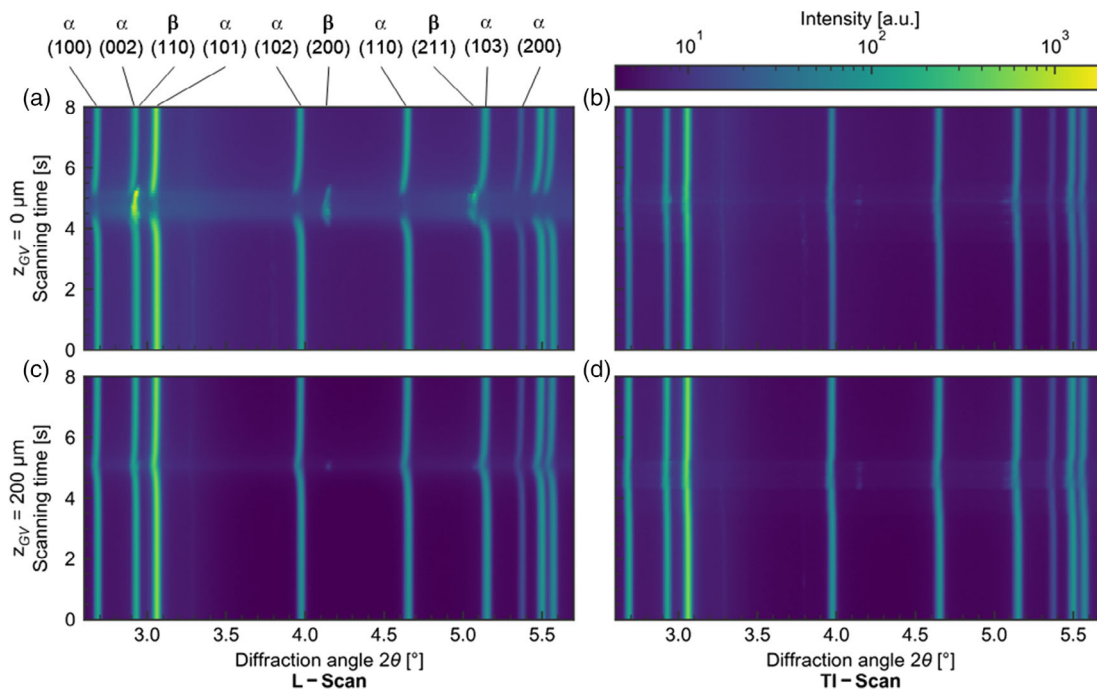


Figure 5. Peak shift during laser exposure for two scanning strategies, both exposed with $P_L = 55$ W and synchrotron GV placed in the center of the sample. a,c) L-Scan samples with increasing depth of the GV, starting in the powder layer down to 200 μm below. b,d) The corresponding TI-Scan samples.

due to increasing temperature. The β peaks also show a lattice expansion and subsequently decrease, as they shift to the left and then back right before vanishing. For the L-Scan, β peaks were observed in the solidified material for $z_{GV} = 200$ μm below the top surface. Intensity counts for the β phase are a lot lower, and their presence is also much shorter. Furthermore, both α and β coincide in the solidified material, as not all the material in the measured volume is transformed, i.e., reaches the phase transformation temperature of 882 $^{\circ}\text{C}$.

For the TI-Scan, the β peaks were a lot less pronounced than for the L-Scan, which is likely caused by the geometrical relation between scanning vectors and synchrotron GV. The GV has a width of 700 μm and a depth of 3 mm. In TI scanning, the GV is traversed 19 times by the laser, each pass only lasting for about 0.014 s for $v_L = 50$ mm s^{-1} . This scanning pattern results in significantly lower β intensities than L scanning, where the GV's full depth is traversed by a single laser hatch, thus showing β reflections for a comparatively longer duration.

In a distance of $z_{GV} = 200$ μm to the top surface, the β peaks were visible but weak for the TI-Scan. They appeared for a longer duration than for the L-Scan, though, which results from the scanning pattern. In all four plots, diffuse scattering during the laser scan is present but most pronounced in the top left plot. It may indicate the presence of a liquid phase, which is expected for the top layer but not necessarily for the layers below.

While the single layers chosen to be presented in Figure 5 are considered representative, a quantitative analysis of the whole process is carried out. Each GV was observed for a total of 20 layers. For those 20 layers, the occurrence of β peaks was

counted. All samples showed β reflections up to a depth of $z_{GV} = 200$ μm . For TI-scanned samples, β reflections occurred up to a distance to the powder layer of $z_{GV} = 400$ μm , but only in 10% of the observed layers for $P_L = 55$ W and 15% of the layers for $P_L = 275$ W. Below 400 μm , no β reflections were visible for either sample. Hence, it can be deduced that phase transformations during the processing of titanium appear up to seven layers beneath the currently processed powder layer for the given process parameters.

2.4. Parameter-Dependent Residual Stress Buildup

Further analysis of the diffraction patterns was performed to determine stresses during manufacturing. The diffraction patterns were segmented into sectors to determine directional lattice spacings in TD and BD that were subsequently converted into lattice strains. The strain difference between TD and BD was used to calculate the respective stress difference described in Section 2.1.3.

For the $\alpha(102)$ reflection, the median stress difference $\Delta\sigma = \sigma_{TD} - \sigma_{BD}$ was calculated, depending on the GV's lateral and vertical position as well as the process parameters used to fabricate the sample; see Figure 6. Each data point in the figure represents the median stress difference for all the diffraction patterns collected over 20 layers in the respective GV.

Schmeiser et al. showed the formation of a subsurface stress maximum during LPBF for Inconel 625 and a single sample.^[8] In the center of the sample and about 350 μm below the top surface, the maximum stress difference $\Delta\sigma$ was found. The results presented in Figure 6 expand upon the results from Schmeiser

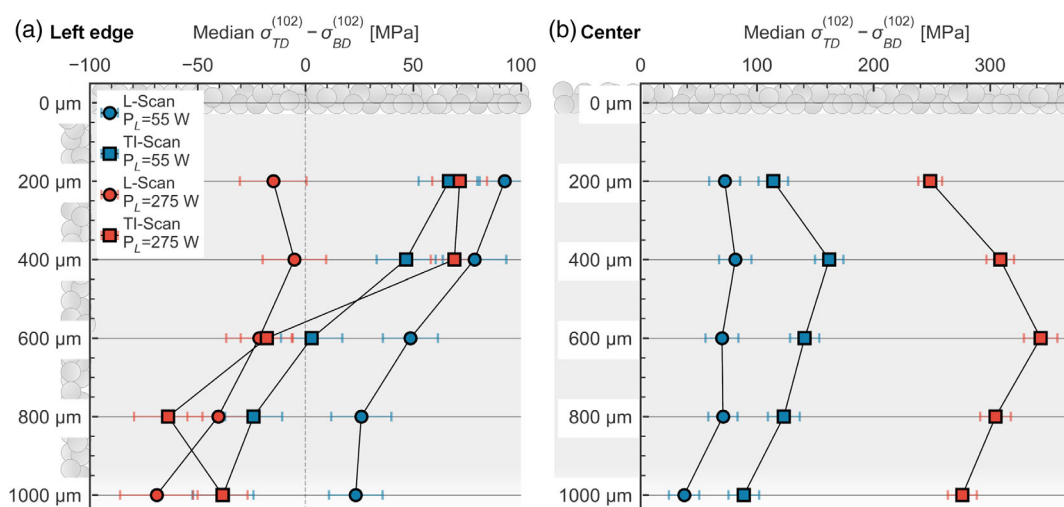


Figure 6. Median stress difference $\sigma_{TD} - \sigma_{BD}$ for a) left edge and b) center GV positions and different sets of process parameters.

et al. They show a maximum stress difference in the center of the sample as well. The magnitude and position of this maximum vary with the process parameters. A higher laser power P_L leads to a shift into deeper layers away from the sample surface, caused by the heat-affected zone's (HAZ) higher penetration depth.

Furthermore, the impact of the scanning strategy is apparent. The stress values for TI-scanned samples are higher than those processed by L-Scan. Both the highest stress difference of about 340 MPa and the deepest maximum position at $z_{GV} = 600 \mu\text{m}$ were found for the TI-scanned sample with a laser power of $P_L = 275 \text{ W}$.

At the left edge of the sample, where the laser exposure begins each layer, all parameters show a similar gradient with increasing depth. Except for the L-scanned sample with $P_L = 275 \text{ W}$, all parameter sets started with a positive stress difference. Here, the solidified material's hindered contraction through the temperature gradient mechanism (TGM) is the stress-inducing mechanism. Another effect can be seen with increasing distance to the surface, as the stress difference is inverted into compression for three out of four parameter sets.

This inversion indicates that with greater distance to the surface, BD stresses are greater than in TD. Phan et al.^[44] performed ex situ measurements on additively manufactured components with comparable geometry to this study's parts. They found a similar inversion at the edge of this sample, where the absolute directional strains changed from tensile to compressive in TD and the opposite for BD. Following these results, the inversion of the stress difference found in this study could also indicate that tensile stresses occur in BD and compressive stresses in TD in deeper layers.

This stress inversion compensates for the reversed stress state in the center of the sample, where tensile stresses in TD and compressive stresses in BD are expected. It has to be noted that due to the experimental procedure, the lower z_{GV} values were investigated first for every sample. Hence, stresses for the lower z_{GV} values experience a more substantial influence by the substrate, such as its stress state and the first layer's bonding to the substrate.

The discrepancies between the sample's left edge and the center vary depending on the scanning strategy and laser power. For samples produced with L-Scan and low laser power, both measurement locations' progressions were very similar. That implies that a homogeneous stress state can be generated with these manufacturing parameters. On the other hand, the stress progressions in the two measuring locations varied distinctly for TI-scanned samples. The discrepancy between the sample edge and the center is highest for samples produced using TI scanning with high laser power.

2.5. Subsurface Stress Progression in a Single Layer

Figure 7a shows the stress progression corresponding to the diffraction patterns in Figure 4 and the estimated average temperature in the GV. As the laser scans over the left edge GV, the GV's maximum temperature is reached. With the given data analysis, a peak temperature of $T_{GV} = 625^\circ\text{C}$ was estimated. In Figure 4, the beta phase occurrence indicated that at least part of the GV had to have reached the phase transformation temperature of 882°C , which is higher than the peak temperature estimated here. The difference is accounted for by the size of the irradiated volume. The larger the analyzed volume, the lower the average temperature. The beta phase only occurs directly around the laser spot, which has a diameter of just $\approx 60 \mu\text{m}$. The volume used for the temperature calculation is more extensive than the part surrounding the laser spot and, therefore, averages large thermal gradients, resulting in a lower peak temperature. Despite the apparent temperature gradients in the GV, an average temperature is a valuable measure to calculate absolute stress values in the whole GV. Determining individual grains' temperatures and stresses from a single diffraction pattern is not feasible with the given experimental setup.

In addition, Figure 7b shows the temperature and stress progression for the same process parameters with the GV located in the sample center. Here, a higher peak temperature of about $T_{GV} = 665^\circ\text{C}$ is reached.

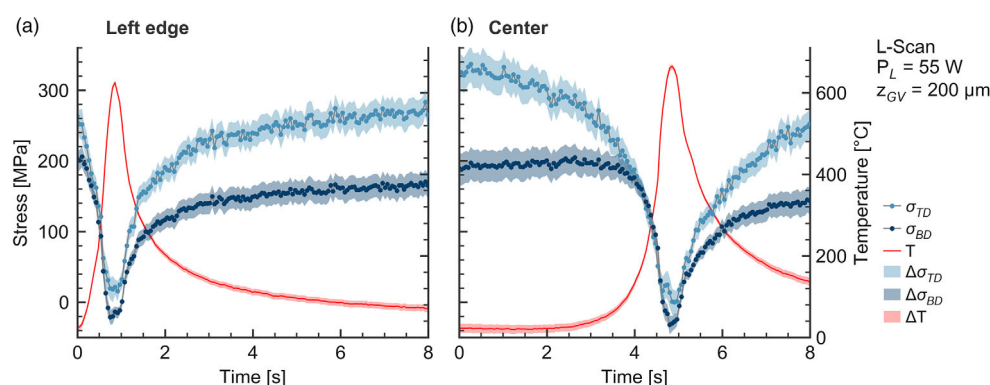


Figure 7. Absolute stress estimation for a single subsurface layer while the laser passes over the GV with a laser power of $P_L = 55$ W, L-Scan pattern, and $z_{GV} = 200$ μm: a) GV located at the left edge of the sample and b) GV in the center of the sample.

Before the laser reaches the GV and the temperature increases sharply, tensile stresses in TD and BD were found, with $\sigma_{TD} = 265$ MPa being about 60 MPa higher than $\sigma_{BD} = 205$ MPa in the left edge GV and about 140 MPa higher in the center GV with $\sigma_{TD} = 320$ MPa and $\sigma_{BD} = 180$ MPa. This stress difference supports the TGM model by Mercelis and Kruth^[7] and transverse contraction elaboration by Schmeiser et al.^[8] As the temperature increases, the stresses drop due to a reduction of the material's stiffness. The material's yield strength has decreased significantly at the temperature peak, leading to plastic deformation and reducing stresses to almost zero.

After the peak temperature is reached, the stresses increase, as the material cools down and its stiffness increases. Simultaneously, the laser has scanned the powder above the GV, and as the molten powder solidifies, it shrinks. The material below, including the GV, impedes that contraction, which induces tensile stresses in the GV. Eventually, the TD stresses reach similar levels as before the peak temperature in Figure 7a with $\sigma_{TD} = 260$ MPa, whereas BD stresses reach $\sigma_{BD} = 160$ MPa, about 40 MPa less than before the laser impact, which is an indication of transverse contraction. In Figure 7b, the stresses appear to be lower after the temperature peak with $\sigma_{TD} = 250$ MPa and $\sigma_{BD} = 140$ MPa. It should be noted that this might be caused by the experimental procedure, as the material has not cooled to the same degree as in Figure 7a during the observation period, implying that further stress increase could happen.

3. Conclusion

A comprehensive study to investigate the subsurface phase transformation and formation of internal stresses in additively manufactured commercially pure titanium grade 1 was carried out at the P07 high energy materials science (HEMS) beamline at the synchrotron facility PETRA III. A custom LPBF machine was used to conduct the experiments. It was shown that the α - β phase transformation occurs in subsurface layers and during initial melting and solidifying. Depending on the process parameters, β titanium reflections were found to a depth of 400 μm or seven layers below the surface. Furthermore, the previously reported formation of a stress difference maximum below the surface was confirmed and elaborated. The results show that

higher laser powers lead to a shift of the stress difference maximum into deeper layers. At the samples' left edge, a stress inversion was found with increasing distance to the top surface. A lower laser power leads to more homogeneous stress distribution in the sample. For the first time in LPBF, absolute in situ stress values are calculated, considering temperature and stress state. During laser impact, the stress values decrease rapidly due to a reduction in stiffness. During cooling, they reach their previous magnitude.

4. Experimental Section

Modified LPBF System: The experimental LPBF system used in this study was described in the previous work.^[34] It was equipped with a 400 W ytterbium fiber laser YLR-400-AC from IPG Laser GmbH, Burbach, Germany. The collimated laser beam with a wavelength of 1070 nm was directed and focused onto the powder bed via a three-axis deflection unit Axialscan-30 from Raylase GmbH, Wessling, Germany, with a laser focus diameter of ≈ 60 μm ($1/e^2$). The powder bed was enclosed in a gas-tight process chamber, with a size that allows for parts of up to 3 mm × 70 mm × 10 mm. The powder bed limitations were made from glassy carbon and acted as X-ray transmissive windows. Also, the process chamber housing contained polyimide windows guaranteeing X-ray transmission through the process chamber. Before the experiments, the chamber was purged with argon to prevent oxidation during the processing. The inert gas atmosphere was continuously circulated and filtered to ensure that the welding fumes do not lead to a loss of laser radiation intensity. An installed recoating mechanism allowed for automatic powder recoating and, therefore, the manufacturing of multilayer parts.

Materials: The titanium powder used in this study was supplied by Advanced Powders & Coatings, Quebec, Canada. It conformed to ASTM B348 grade 1 in terms of its composition. The particles were spherical, and the particle size distribution was between 20 and 63 μm with a 90th percentile $D_{90} = 54$ μm. The substrates were manufactured from commercially pure titanium grade 2.

LPBF Process Parameters and Measurement Modes: The LPBF process parameters used in this study are listed in Table 1. A laser power of $P_L = 55$ W yielded acceptable density results with a relative density of $\rho_r > 99.0\%$ compared with conventionally produced titanium with a density of $\rho = 4.5$ g cm⁻³. Parameter sets 1 and 3 offered high temporal resolution for the diffraction experiments, whereas sets 2 and 4 contained the laser power value $P_L = 275$ W of an industrially used parameter set for dense parts with a compromise in temporal resolution. Two different scanning patterns were investigated. For the longitudinal scanning (L-Scan), only unidirectional scanning vectors, without meandering, parallel to

Table 1. Process parameters.

Parameter	Unit	Set 1	Set 2	Set 3	Set 4
Laser power, P_L	W	55	275	55	275
Scanning speed, v_L	mm s^{-1}	50	760	50	760
Scanning pattern		L	L	TI	TI
Laser spot diameter, d_L	μm		≈ 60		
Hatch distance, h_L	μm		120		
Layer thickness, Δz	μm		50		

the primary synchrotron radiation beam were utilized. For the transverse island scanning (TI-Scan), the scanning vectors were transverse to the synchrotron radiation beam with vector lengths of the same magnitude as for the L-Scan vectors. Hence, several vector fields or islands were formed over the scan layer; see Figure 1a.

Measurements were conducted in measurement mode 1 (MM1).^[34] In MM1, the GV was in a defined distance z_{GV} to the topmost layer, the working plane. After processing of a layer, the sample was moved in negative BD by the amount of the layer thickness Δz , whereas the glassy carbon plates and the working plane stayed on a constant BD level. Then, a new powder layer was deposited, and the procedure was repeated. Accordingly, relative to the sample, the GV's vertical position along BD changed layer by layer, whereas the lateral position, along TD, was fixed throughout the buildup of one sample.

In any individual sample, the GV distance to the top surface z_{GV} , Figure 1b, was kept constant for 20 layers. Afterward, the distance z_{GV} was increased by 200 μm , and the process was repeated for another 20 layers. In total, six values for z_{GV} were investigated for each sample from 0 to 1000 μm . For each parameter set, two lateral GV locations were observed: the left edge of the sample and the center of the sample.

In Situ Diffraction Experiments: In situ high energy synchrotron radiation diffraction experiments were carried out at the HEMS beamline P07 at PETRA III at DESY, Hamburg, Germany.^[33] A beam energy of $E = 103.43 \text{ keV}$ ($\lambda = 0.1199 \text{ \AA}$) was used. The X-ray beam size was set to $700 \times 100 \mu\text{m}$ to reach a satisfactory spatial resolution in the build direction. The width of the GV was adjusted to irradiate enough grains to collect full diffraction patterns.

Diffraction patterns were collected using a Dectris PILATUS3 2M detector using a sampling rate of $f = 20 \text{ Hz}$ for measurements in solidified material and $f = 10 \text{ Hz}$ when measuring in the powder layer. The distance between sample and detector was 1110.237 mm to collect the first 13 hkl reflections. Lanthanum hexaboride (LaB_6) was used to determine the sample-to-detector distance. Subsequently, the diffraction patterns were azimuthally integrated using the python library pyFAI.^[45] For the phase transformation results, full integration was performed, whereas a sector integration was used for stress results. For the sector integration, the diffraction rings were divided into 72 equal-angle sectors.

The integration produced 1D line spectra, where the (102) reflection was approximated employing a PseudoVoigt function using the python library lmfit.^[46] The (102) reflection was chosen for stress analysis due to several advantages: its distance to neighboring peaks, absence of overlap with β peaks, and preferable location on the Pilatus detector's tiles.

Sector integration yielded the lattice spacings in TD and BD, where d_{TD} corresponded to the averaged peak position gathered from the sectors with azimuths $\eta = 0^\circ$ and $\eta = 180^\circ$, whereas d_{BD} was related to the peak positions from sectors parallel to BD, azimuths $\eta = 90^\circ$ and $\eta = 0^\circ$.

Acknowledgements

This article was based on the results obtained in project No. 317078200 supported by the Deutsche Forschungsgemeinschaft (DFG). Furthermore, the authors acknowledge Helmholtz-Zentrum Hereon (HZH) for the

support and the provision of experimental facilities at PETRA III. They also thank the three anonymous reviewers for their thorough and extensive comments, thereby improving this manuscript substantially.

Open access funding enabled and organized by Projekt DEAL.

Conflict of Interest

The authors declare no conflict of interest.

Data Availability Statement

The data that support the findings of this study are available from the corresponding author upon reasonable request.

Keywords

commercially pure titanium, in situ synchrotron radiation diffraction, internal stress, laser powder bed fusion, phase transformation, subsurface

Received: December 18, 2020

Revised: March 16, 2021

Published online:

- [1] M. Seifi, A. Salem, J. Beuth, O. Harrysson, J. J. Lewandowski, *JOM* **2016**, 68, 747.
- [2] L.-C. Zhang, H. Attar, M. Calin, J. Eckert, *Mater. Technol.* **2016**, 31, 66.
- [3] L. Parry, I. A. Ashcroft, R. D. Wildman, *Addit. Manuf.* **2016**, 12, 1.
- [4] G. Mohr, S. J. Altenburg, K. Hilgenberg, *Addit. Manuf.* **2020**, 32, 101080.
- [5] G. Mohr, N. Scheuschner, K. Hilgenberg, *Procedia CIRP* **2020**, 94, 155.
- [6] Y. Li, D. Gu, *Addit. Manuf.* **2014**, 1–4, 99.
- [7] P. Mercelis, J.-P. Kruth, *Rapid Prototyp. J.* **2006**, 12, 254.
- [8] F. Schmeiser, E. Krohmer, N. Schell, E. Uhlmann, W. Reimers, *Addit. Manuf.* **2020**, 32, 101028.
- [9] J. L. Bartlett, X. Li, *Addit. Manuf.* **2019**, 27, 131.
- [10] Z.-C. Fang, Z.-L. Wu, C.-G. Huang, C.-W. Wu, *Opt. Laser Technol.* **2020**, 129, 106283.
- [11] Z. Xiao, C. Chen, H. Zhu, Z. Hu, B. Nagarajan, L. Guo, X. Zeng, *Mater. Des.* **2020**, 193, 108846.
- [12] T. Mukherjee, V. Manvatkar, A. De, T. DebRoy, *Scr. Mater.* **2017**, 127, 79.
- [13] H. Ali, H. Ghadbeigi, K. Mumtaz, *J. Mater. Eng. Perform.* **2018**, 27, 4059.
- [14] N. C. Levkulich, S. L. Semiatin, J. E. Gockel, J. R. Middendorf, A. T. DeWald, N. W. Klingbeil, *Addit. Manuf.* **2019**, 28, 475.
- [15] F. R. Kaschel, M. Celikin, D. P. Dowling, *J. Mater. Process. Technol.* **2020**, 278, 116539.
- [16] A. S. Wu, D. W. Brown, M. Kumar, G. F. Gallegos, W. E. King, *Metall. Mater. Trans. A* **2014**, 45, 6260.
- [17] Y. Liu, Y. Yang, Di Wang, *Int. J. Adv. Manuf. Technol.* **2016**, 87, 647.
- [18] J. Robinson, I. Ashton, P. Fox, E. Jones, C. Sutcliffe, *Addit. Manuf.* **2018**, 23, 13.
- [19] J.-P. Kruth, J. Deckers, E. Yasa, R. Wauthlé, *Proc. Inst. Mech. Eng. B* **2012**, 226, 980.
- [20] I. Yadroitsava, S. Grewar, D. Hattingh, I. Yadroitsev, *Mater. Sci. Forum* **2015**, 828–829, 305.
- [21] H. Ali, H. Ghadbeigi, K. Mumtaz, *Mater. Sci. Eng., A* **2018**, 712, 175.
- [22] J. C. Williams, R. R. Boyer, *Metals* **2020**, 10, 705.

- [23] P. Bartolo, J.-P. Kruth, J. Silva, G. Levy, A. Malshe, K. Rajurkar, M. Mitsuishi, J. Ciurana, M. Leu, *CIRP Ann.* **2012**, 61, 635.
- [24] A. Kolomiets, Y. J. Grobman, V. V. Popov, E. Strokin, G. Senchikhin, E. Tarazi, *J. New Music Res.* **2020**, 760, 1.
- [25] U. Zwickler, *Titan und Titanlegierungen*, Springer, Berlin, Heidelberg **1974**.
- [26] D. Gu, Y.-C. Hagedorn, W. Meiners, G. Meng, R. J. S. Batista, K. Wissenbach, R. Poprawe, *Acta Mater.* **2012**, 60, 3849.
- [27] H. Attar, M. Calin, L. C. Zhang, S. Scudino, J. Eckert, *Mater. Sci. Eng., A* **2014**, 593, 170.
- [28] B. Attard, S. Cruchley, C. Beetz, M. Megahed, Y. L. Chiu, M. M. Attallah, *Addit. Manuf.* **2020**, 36, 101432.
- [29] N. P. Calt, V. Thampy, D. R. Lee, A. A. Martin, R. Ganeriwala, J. Wang, P. J. Depond, T. T. Roehling, A. Y. Fong, A. M. Kiss, C. J. Tassone, K. H. Stone, J. Nelson Weker, M. F. Toney, A. W. van Buuren, M. J. Matthews, *Mater. Des.* **2020**, 195, 108987.
- [30] S. Hocine, H. van Swygenhoven, S. van Petegem, C. S. T. Chang, T. Maimaitiyili, G. Tinti, D. Ferreira Sanchez, D. Grolmund, N. Casati, *Mater. Today* **2020**, 34, 30.
- [31] C. Zhao, K. Fezzaa, R. W. Cunningham, H. Wen, F. de Carlo, L. Chen, A. D. Rollett, T. Sun, *Sci. Rep.* **2017**, 7, 3602.
- [32] D. Dye, H. J. Stone, M. Watson, R. B. Rogge, *Metall. Mater. Trans. A* **2014**, 45, 2038.
- [33] N. Schell, A. King, F. Beckmann, T. Fischer, M. Müller, A. Schreyer, *Mater. Sci. Forum* **2013**, 772, 57.
- [34] E. Uhlmann, E. Krohmer, F. Schmeiser, N. Schell, W. Reimers, *Rev. Sci. Instrum.* **2020**, 91, 75104.
- [35] C. Chen, Z. Xiao, H. Zhu, X. Zeng, *Int. J. Adv. Manuf. Technol.* **2020**, 110, 3467.
- [36] Z. Wang, E. Denlinger, P. Michaleris, A. D. Stoica, D. Ma, A. M. Beese, *Mater. Des.* **2017**, 113, 169.
- [37] T. Mishurova, I. Serrano-Muñoz, T. Fritsch, A. Ulbricht, M. Sprengel, A. Evans, A. Kromm, M. Madia, G. Bruno, in *Structural Integrity of Additive Manufactured Materials & Parts* (Eds.: N. Shamsaei, M. Seifi), ASTM International, West Conshohocken, PA **2020**, p. 122.
- [38] J. W. Suiter, *J. Inst. Met.* **1954/55**, 6, 460.
- [39] S. Nemat-Nasser, W. G. Guo, J. Y. Cheng, *Acta Mater.* **1999**, 47, 3705.
- [40] J. I. Medoff, I. Cadoff, *J. Met.* **1959**, 11, 581.
- [41] E. S. Fisher, C. J. Renken, *Phys. Rev.* **1964**, 135, 482.
- [42] V. Hauk, H. Behnken, *Structural and Residual Stress Analysis by Nondestructive Methods: Evaluation – Application – Assessment*, Elsevier, Amsterdam **1997**.
- [43] U. Scipioni Bertoli, G. Guss, S. Wu, M. J. Matthews, J. M. Schoenung, *Mater. Des.* **2017**, 135, 385.
- [44] T. Q. Phan, M. Strantz, M. R. Hill, T. H. Gnaupel-Herold, J. Heigel, C. R. D'Elia, A. T. DeWald, B. Clausen, D. C. Pagan, J. Y. Peter Ko, D. W. Brown, L. E. Levine, *Integr. Mater. Manuf. Innov.* **2019**, 8, 318.
- [45] G. Ashiotis, A. Deschildre, Z. Nawaz, J. P. Wright, D. Karkoulis, F. E. Picca, J. Kieffer, *J. Appl. Crystallogr.* **2015**, 48, 510.
- [46] M. Newville, T. Stensitzki, D. B. Allen, A. Ingargiola, *LMFIT: Non-Linear Least-Square Minimization and Curve-Fitting for Python*, Zenodo.

Part III

Summary and outlook

The present thesis examined the LPBF process using comprehensive *in situ* X-ray diffraction experiments at the HEMS beamline at the PETRA III storage ring at DESY. A custom LPBF device was used for these experiments to depict the industrial LPBF process accurately. The machine features an automated powder recoating mechanism and the ability to produce multi-layer components with up to 120 layers. Various measurement modes were employed to track a fixed or moving gauge volume in the material as the part is being manufactured.

By virtue of the high photon flux at the HEMS beamline, temporally resolved changes in the stress state, phase composition, and microstructure of two different materials, Inconel 625 and commercially-pure titanium grade 1, were evaluated to reveal the underlying mechanisms that cause the properties specific to LPBF parts. The objectives outlined in chapter 3 are discussed and summarized in the following paragraphs.

First goal – Microstructural responses to laser processing In the present work, the $\alpha \rightarrow \beta$ phase transformation of commercially-pure titanium grade 1 was evaluated in chapter P3. It was found that the phase transformation is triggered numerous times after the initial melting and solidification of the powder.

Furthermore, the texture evolution was evaluated in chapter P1. The texture of the component is heavily influenced by the laser parameters, where a strong preferred orientation was found for a high laser power and scanning speed compared to a weak texture when using a low laser power and slow scanning speed. Furthermore, the measurement of a constant gauge volume demonstrated the effect of repetitive laser scanning on the microstructure. Substantial texture changes were discovered during laser scanning up to ten layers below the working plane. Concurrently, the preferred orientation was lowered significantly. Because the material remains solid during this time, this texture reduction is attributed to recrystallization. The original article in chapter P1 is the first to report this material response *in situ* during LPBF.

Further microstructural changes occur following the recrystallization step, including recurring lattice defects after the initial reduction during recrystallization, which were detected via analysis of the peak width. While the actual peak width does not change after a certain amount of layers, changes in the peak shape were observed up to the last layer. An analysis of the peak asymmetry over time revealed a steady increase related to chemical segregation processes that cause lattice spacing gradients in the gauge volume. These segregations were confirmed *ex situ* by TEM investigations, underlining that *in situ* X-ray diffraction experiments are well-suited for examining microstructural processes during LPBF as they occur.

Second goal – Stress-related phenomena Beyond the microstructure and phase composition, the formation and evolution of stresses were investigated in two stages and reported in chapters P2 and P3. Initially, lattice strains and their progressions were used to derive conclusions about the internal stresses. In the center of the sample, in-plane strains were higher than out-of-plane strains, which was related to tensile stresses in TD and a subsequent transverse contraction in BD. At the sample edge, the opposite was found, with strains in BD surpassing those in TD. A drop in the lattice spacings was observed during laser exposure right before a sharp increase when the laser scanned across the gauge volume. This short decrease is linked to a compressive stress zone ahead of the heat-affected zone created by the laser. Additionally, the TGM model by Mercelis and Kruth [Mer06] was verified, and a mechanism for clarifying directional differences in the stress field was introduced.

Considering the difference between TD and BD in the lattice spacing progressions, spatially and temporally resolved stress differences were calculated. A low scanning speed and laser power resulted in a more homogeneous stress distribution than higher laser powers and scanning speeds. The observation of a fixed gauge volume in the center of the sample over the whole production process revealed that the laser changes the stress state of the sample up to the final layer during the LPBF process. With increasing distance to the top surface, the observed gauge volume experiences an increase in stress difference, which reaches a maximum about eight layers below the surface¹ and tapers off with higher layer numbers. Higher laser powers and scanning speeds shifted this stress maximum into deeper layers. While there is a positive stress difference (higher stress in TD than in BD) close to the surface at the edge of the sample as well, a stress inversion is found there with increasing distance to the top layer. Based on the *in situ* results, a mechanistic model to describe the formation of stresses at the part-scale was developed and confirmed by an *ex situ* stress distribution measurement.

Third goal – Temperature evaluation The *in situ* diffraction experiments revealed several thermal phenomena. In a single layer, heat is accumulated in the areas that are exposed last, leading to higher temperatures there. These increased temperatures impact microstructural features such as grain growth and may result in unwanted inhomogeneity. In addition to this so-called lateral heat accumulation, vertical heat accumulation was also observed. With increased build height, heat conduction away from the working plane is slowed down as the distance to the substrate, which acts as a heatsink, increases.

While these phenomena were deduced from the plain lattice strain progressions, a novel temperature evaluation approach was presented in chapter P3. In a near-surface gauge volume, the laser impact results in a characteristic lattice spacing progression with a sharp increase and a maximum right as the laser reaches the gauge volume, after which the lattice spacings decrease and taper off. The peak in the lattice spacings coincides with the maximum temperature. If this maximum temperature is sufficiently high, the mechanical properties of the solid material plummet, leading to plastic deformation and stress relief. Therefore, the lattice strain peak in a near-surface gauge volume can be assumed as purely thermal and correlated to the maximum

¹Given a layer thickness of 50 μm , laser power $P_L = 50 \text{ W}$, $v_L = 50 \text{ mm s}^{-1}$, L-scanning.

temperature. If the stress state before laser exposure is also considered, the temperatures for the whole duration of laser exposure can be calculated.

It has to be noted that there are likely large temperature gradients in the gauge volume during laser exposure, purely from geometrical considerations of the gauge volume size and the melt pool size. A single diffraction pattern can not depict these gradients as it represents an integrated average over a given duration of exposure. Despite attempts to deconvolve temperature superpositions via (moving) difference patterns, which have been inconclusive, a single gauge volume temperature was used for the temperature evaluation in the present work.

Fourth goal – Absolute stress values Based on the temperature evaluation approach described above, absolute stress values were calculated and reported in chapter P3, too. The temperatures were used to determine the elastic constants and the stress-free lattice spacing. Under the assumption of a biaxial stress state, which is reasonable based on geometrical considerations of the sample, the internal stresses in TD and BD were calculated. The resulting stress progressions showed tensile stresses before laser exposure, which sharply drop close to zero, coinciding with the temperature peak. As the gauge volume cools, the stresses increase to their previous magnitude.

Overall, the objectives of this thesis were very well achieved. Significant insights into the stress-forming mechanisms, phase transformations, and microstructure evolution were obtained. Nevertheless, there is still a great need for research to extend the fundamental process understanding further. *In situ* diffraction experiments with high-energy synchrotron X-rays have proven to be a viable tool for this task.

For future experiments, various advancements should be pursued on

1. The equipment level.
2. The experiment level.
3. The data evaluation level.

The LPBF device used in the present work functioned very well and fulfilled the goal of accurately replicating the industrial LPBF process. However, for future developments, two additions would be desirable. Firstly, the ability to rotate the process chamber in relation to the incident synchrotron beam would allow the determination of strains in the through-thickness direction, which is not possible with the current setup. Of course, rotating the incidence angle would transform the gauge volume into a parallelepiped, which would have to be accounted for with suitable corrections. Still, this rotation would allow the determination of the triaxial stress state of the sample and present a significant step for the accurate determination of internal stresses.

The other prerequisite for absolute stress values is knowledge of the sample's temperature distribution, especially in the gauge volume. As described, a temperature evaluation approach directly from the diffraction patterns was developed in this work, but an augmentation via metrological and numerical methods would be advantageous. Surface temperatures could be measured by pyrometry or thermography. In combination with temperature sensors at the substrate, temperature gradients between the surface and the substrate could be evaluated to approximate the temperatures in the gauge volume. Further accuracy would be gained through numerical modeling of the temperatures in the part. In any case, supplementing the temperature approximations from the lattice spacings with additional temperature data would enhance the accuracy and certainty of the stress calculations.

At the intersection of the equipment and experiment level, the possibilities offered by current X-ray area detectors should be fully exploited. The DECTRIS DECTRIS Pilatus3 X CdTe 2M detector has a maximum frame rate of 250 Hz, which could not be fully utilized in the present study. However, further improvements of the temporal resolution are necessary, especially when moving the experiments towards conventional, industrially used process parameters. Such experiments

could investigate conventional, complex scanning strategies, geometrical effects such as overhang structures, and preheating the substrate and powder bed.

A further supplement on the experimental level would be using a „dummy“ or mock part to evaluate the actual impact of irradiated loose powder. As discussed in chapter P2 and chapter P3, the X-ray beam passes through unmelted powder before and after the actual part. The two powder layers in front and behind of the part are only 250 μm in thickness, so their contribution to the diffraction pattern is minor compared to the 2.5 mm thickness of the part. The insertion of a 2.5 mm thick dummy part made from a non-diffracting material such as glassy carbon could quantify the impact of the powder. A diffraction image with a full powder bed and the dummy part could be used as a background image to subtract from the actual *in situ* diffraction patterns.

Advancements on the data evaluation level include multi-peak analyses. Titanium showed overlapping peaks for most reflections due to the concurrent existence of the α/α' phases. While attempts to deconvolve these peaks were made, success has been limited so far, and further efforts should be made in this regard in future investigations. The powder background pattern described above would be beneficial in this regard, too.

The present work has shown that *in situ* X-ray diffraction experiments are a valuable tool for gaining unprecedented insight into stresses, phase transformations, and microstructure development during LPBF processing. Extending the insights laid out in this thesis, and including process parameters with increased complexity, complemented by numerical modeling, will significantly advance the fundamental understanding of the process.

Part IV

Appendix

References

- [Abo19] N. T. Aboulkhair, M. Simonelli, L. Parry, I. Ashcroft, C. Tuck, and R. Hague. “3D printing of Aluminium alloys: Additive Manufacturing of Aluminium alloys using selective laser melting”. *Progress in Materials Science* **106** (2019), p. 100578.
DOI: 10.1016/j.pmatsci.2019.100578.
- [Ali18] H. Ali, H. Ghadbeigi, and K. Mumtaz. “Processing Parameter Effects on Residual Stress and Mechanical Properties of Selective Laser Melted Ti6Al4V”. *Journal of Materials Engineering and Performance* **27** (2018), pp. 4059–4068.
DOI: 10.1007/s11665-018-3477-5.
- [Als11] J. Als-Nielsen and D. McMorrow. *Elements of Modern X-ray Physics*. 2. ed. Chichester: Wiley, 2011.
DOI: 10.1002/9781119998365.
- [Ami21] B. Aminforoughi, S. Degener, J. Richter, A. Liehr, and T. Niendorf. “A Novel Approach to Robustly Determine Residual Stress in Additively Manufactured Microstructures Using Synchrotron Radiation”. *Advanced Engineering Materials* **23** (2021), p. 2100184.
DOI: 10.1002/adem.202100184.
- [And18] L. S. Anderson, A. M. Venter, B. Vrancken, D. Marais, J. van Humbeeck, and T. H. Becker. “Investigating the Residual Stress Distribution in Selective Laser Melting Produced Ti-6Al-4V using Neutron Diffraction”. In: *Mechanical stress evaluation by neutron and synchrotron radiation - MECA SENS 2017*. Ed. by D. Marais, T. M. Holden, and A. M. Venter. Materials research proceedings. Millersville, PA: Materials Science Forum LLC, 2018, pp. 73–78.
DOI: 10.21741/9781945291678-11.
- [Art20] K. Artzt, T. Mishurova, P.-P. Bauer, J. Gussone, P. Barriobero-Vila, S. Evsevlev, G. Bruno, G. Requena, and J. Haubrich. “Pandora’s Box-Influence of Contour Parameters on Roughness and Subsurface Residual Stresses in Laser Powder Bed Fusion of Ti-6Al-4V”. *Materials (Basel, Switzerland)* **13** (2020).
DOI: 10.3390/ma13153348.
- [Ash15] G. Ashiotis, A. Deschildre, Z. Nawaz, J. P. Wright, D. Karkoulis, F. E. Picca, and J. Kieffer. “The fast azimuthal integration Python library: pyFAI”. *Journal of Applied Crystallography* **48** (2015), pp. 510–519.
DOI: 10.1107/S1600576715004306.

References

- [Att17] H. Attar, S. Ehtemam-Haghighi, D. Kent, X. Wu, and M. S. Dargusch. “Comparative study of commercially pure titanium produced by laser engineered net shaping, selective laser melting and casting processes”. *Materials Science and Engineering: A* **705** (2017), pp. 385–393.
DOI: 10.1016/j.msea.2017.08.103.
- [Bac10] F. Bachmann, R. Hielscher, and H. Schaeben. “Texture Analysis with MTEX – Free and Open Source Software Toolbox”. *Solid State Phenomena* **160** (2010), pp. 63–68.
DOI: 10.4028/www.scientific.net/SSP.160.63.
- [Bar18] P. Barriobero-Vila, J. Gussone, A. Stark, N. Schell, J. Haubrich, and G. Requena. “Peritectic titanium alloys for 3D printing”. *Nature communications* **9** (2018), p. 3426.
DOI: 10.1038/s41467-018-05819-9.
- [Bar19a] R. Barros, F. J. G. Silva, R. M. Gouveia, A. Saboori, G. Marchese, S. Biamino, A. Salmi, and E. Atzeni. “Laser Powder Bed Fusion of Inconel 718: Residual Stress Analysis Before and After Heat Treatment”. *Metals* **9** (2019), p. 1290.
DOI: 10.3390/met9121290.
- [Bar19b] J. L. Bartlett and X. Li. “An overview of residual stresses in metal powder bed fusion”. *Additive Manufacturing* **27** (2019), pp. 131–149.
DOI: 10.1016/j.addma.2019.02.020.
- [Bas16] A. Basak and S. Das. “Epitaxy and Microstructure Evolution in Metal Additive Manufacturing”. *Annual Review of Materials Research* **46** (2016), pp. 125–149.
DOI: 10.1146/annurev-matsci-070115-031728.
- [Ber20] K. M. Bertsch, G. Meric de Bellefon, B. Kuehl, and D. J. Thoma. “Origin of dislocation structures in an additively manufactured austenitic stainless steel 316L”. *Acta Materialia* **199** (2020), pp. 19–33.
DOI: 10.1016/j.actamat.2020.07.063.
- [Bia20] P. Bian, J. Shi, Y. Liu, and Y. Xie. “Influence of laser power and scanning strategy on residual stress distribution in additively manufactured 316L steel”. *Optics & Laser Technology* **132** (2020), p. 106477.
DOI: 10.1016/j.optlastec.2020.106477.
- [Bil05] D. H. Bilderback, P. Elleaume, and E. Weckert. “Review of third and next generation synchrotron light sources”. *Journal of Physics B: Atomic, Molecular and Optical Physics* **38** (2005), S773–S797.
DOI: 10.1088/0953-4075/38/9/022.
- [Bli13] J. Bliedtner, H. Müller, and A. Barz. *Lasermaterialbearbeitung: Grundlagen - Verfahren - Anwendungen - Beispiele ; mit 110 Tabellen*. München: Carl Hanser Verlag GmbH & Co. KG, 2013.
DOI: 10.3139/9783446429291.
- [Buc14] D. Buchbinder, W. Meiners, N. Pirch, K. Wissenbach, and J. Schrage. “Investigation on reducing distortion by preheating during manufacture of aluminum components using selective laser melting”. *Journal of Laser Applications* **26** (2014), p. 012004.
DOI: 10.2351/1.4828755.

- [Cal20] N. P. Calta, V. Thampy, D. R. Lee, A. A. Martin, R. Ganeriwala, J. Wang, P. J. Depond, T. T. Roehling, A. Y. Fong, A. M. Kiss, C. J. Tassone, K. H. Stone, J. Nelson Weker, M. F. Toney, A. W. van Buuren, and M. J. Matthews. “Cooling dynamics of two titanium alloys during laser powder bed fusion probed with in situ X-ray imaging and diffraction”. *Materials & Design* **195** (2020), p. 108987.
DOI: 10.1016/j.matdes.2020.108987.
- [Cal18] N. P. Calta, J. Wang, A. M. Kiss, A. A. Martin, P. J. Depond, G. M. Guss, V. Thampy, A. Y. Fong, J. N. Weker, K. H. Stone, C. J. Tassone, M. J. Kramer, M. F. Toney, A. van Buuren, and M. J. Matthews. “An instrument for in situ time-resolved X-ray imaging and diffraction of laser powder bed fusion additive manufacturing processes”. *The Review of scientific instruments* **89** (2018), p. 055101.
DOI: 10.1063/1.5017236.
- [Cas08] C. Casavola, S. L. Campanelli, and C. Pappalettere. “Experimental analysis of residual stresses in the selective laser melting process”. In: *11th International Congress and Exhibition on Experimental and Applied Mechanics 2008*. Red Hook, NY: Curran, 2008.
- [Cec19] F. Ceccanti, A. Giorgetti, and P. Citti. “A Support Structure Design Strategy for Laser Powder Bed Fused Parts”. *Procedia Structural Integrity* **24** (2019), pp. 667–679.
DOI: 10.1016/j.prostr.2020.02.059.
- [Che20] C. Chen, Z. Xiao, H. Zhu, and X. Zeng. “Distribution and evolution of thermal stress during multi-laser powder bed fusion of Ti-6Al-4 V alloy”. *Journal of Materials Processing Technology* **284** (2020), p. 116726.
DOI: 10.1016/j.jmatprotec.2020.116726.
- [Che04] J. Chen, L. Li, D. Weidner, and M. Vaughan. “Deformation experiments using synchrotron X-rays: in situ stress and strain measurements at high pressure and temperature”. *Physics of the Earth and Planetary Interiors* **143-144** (2004), pp. 347–356.
DOI: 10.1016/j.pepi.2003.09.021.
- [Cla20] S. J. Clark, C. L. A. Leung, Y. Chen, L. Sinclair, S. Marussi, and P. D. Lee. “Capturing Marangoni flow via synchrotron imaging of selective laser melting”. *IOP Conference Series: Materials Science and Engineering* **861** (2020), p. 012010.
DOI: 10.1088/1757-899X/861/1/012010.
- [DAv18] R. A. D’Aveni. *The pan-industrial revolution: How new manufacturing titans will transform the world*. Boston: Houghton Mifflin Harcourt, 2018.
- [Deb18] T. DebRoy, H. L. Wei, J. S. Zuback, T. Mukherjee, J. W. Elmer, J. O. Milewski, A. M. Beese, A. Wilson-Heid, A. De, and W. Zhang. “Additive manufacturing of metallic components – Process, structure and properties”. *Progress in Materials Science* **92** (2018), pp. 112–224.
DOI: 10.1016/j.pmatsci.2017.10.001.

References

- [Dec20] Dectris Ltd. *Pilatus3 R/S/X Detector System: User Manual: Document Version v1.2.0*. 2020.
URL: https://media.dectris.com/220621-User_Manual-DECTRIS_PILATUS3.pdf (visited on March 26, 2022).
- [Deh15] R. R. Dehoff, M. M. Kirka, W. J. Sames, H. Bilheux, A. S. Tremsin, L. E. Lowe, and S. S. Babu. "Site specific control of crystallographic grain orientation through electron beam additive manufacturing". *Materials Science and Technology* **31** (2015), pp. 931–938.
DOI: 10.1179/1743284714Y.00000000734.
- [Den17] E. R. Denlinger, M. Gouge, J. Irwin, and P. Michaleris. "Thermomechanical model development and in situ experimental validation of the Laser Powder-Bed Fusion process". *Additive Manufacturing* **16** (2017), pp. 73–80.
DOI: 10.1016/j.addma.2017.05.001.
- [Deu21] Deutsches Elektronen-Synchrotron DESY. *P07 - High Energy Materials Science Beamline: Unified Data Sheet*. 2021.
URL: https://photon-science.desy.de/facilities/petra_iii/beamlines/p07_high_energy_materials_science/unified_data_sheet_p07/index_eng.html (visited on March 26, 2022).
- [DiW16] Di Wang, C. Song, Y. Yang, and Y. Bai. "Investigation of crystal growth mechanism during selective laser melting and mechanical property characterization of 316L stainless steel parts". *Materials & Design* **100** (2016), pp. 291–299.
DOI: 10.1016/j.matdes.2016.03.111.
- [Din11] J. Ding, P. Colegrove, J. Mehnen, S. Ganguly, P. M. Sequeira Almeida, F. Wang, and S. Williams. "Thermo-mechanical analysis of Wire and Arc Additive Layer Manufacturing process on large multi-layer parts". *Computational Materials Science* **50** (2011), pp. 3315–3322.
DOI: 10.1016/j.commatsci.2011.06.023.
- [DuP19] A. Du Plessis, C. Broeckhoven, I. Yadroitsava, I. Yadroitsev, C. H. Hands, R. Kunju, and D. Bhate. "Beautiful and Functional: A Review of Biomimetic Design in Additive Manufacturing". *Additive Manufacturing* **27** (2019), pp. 408–427.
DOI: 10.1016/j.addma.2019.03.033.
- [Eig95] B. Eigenmann and E. Macherauch. "Röntgenographische Untersuchung von Spannungszuständen in Werkstoffen". *Materialwissenschaft und Werkstofftechnik* **26** (1995), pp. 148–160.
DOI: 10.1002/mawe.19950260310.
- [Gan19] R. K. Ganeriwala, M. Strantza, W. E. King, B. Clausen, T. Q. Phan, L. E. Levine, D. W. Brown, and N. E. Hodge. "Evaluation of a thermomechanical model for prediction of residual stress during laser powder bed fusion of Ti-6Al-4V". *Additive Manufacturing* **27** (2019), pp. 489–502.
DOI: 10.1016/j.addma.2019.03.034.

- [Goe20] S. Goel, M. Neikter, J. Capek, E. Polatidis, M. H. Colliander, S. Joshi, and R. Pederson. “Residual stress determination by neutron diffraction in powder bed fusion-built Alloy 718: Influence of process parameters and post-treatment”. *Materials & Design* **195** (2020), p. 109045.
DOI: 10.1016/j.matdes.2020.109045.
- [Gol20] K. Gola, B. Dubiel, and I. Kalembe-Rec. “Microstructural Changes in Inconel 625 Alloy Fabricated by Laser-Based Powder Bed Fusion Process and Subjected to High-Temperature Annealing”. *Journal of Materials Engineering and Performance* **29** (2020), pp. 1528–1534.
DOI: 10.1007/s11665-020-04605-3.
- [Gon14] X. Gong, T. Anderson, and K. Chou. “Review on Powder-Based Electron Beam Additive Manufacturing Technology”. *Manuf. Rev.* **1** (2014), pp. 507–515.
DOI: 10.1115/ISFA2012-7256.
- [Hag21] N. Haghdadi, M. Laleh, M. Moyle, and S. Primig. “Additive manufacturing of steels: a review of achievements and challenges”. *Journal of Materials Science* **56** (2021), pp. 64–107.
DOI: 10.1007/s10853-020-05109-0.
- [Ham98] A. P. Hammersley. *FIT2D: An Introduction and Overview: ESRF Internal Report*. 1998.
URL: https://www.esrf.fr/computing/scientific/FIT2D/FIT2D_INTRO/fit2d.html (visited on March 26, 2022).
- [Han18] Q. Han, H. Gu, S. Soe, R. Setchi, F. Lacan, and J. Hill. “Manufacturability of AlSi10Mg overhang structures fabricated by laser powder bed fusion”. *Materials & Design* **160** (2018), pp. 1080–1095.
DOI: 10.1016/j.matdes.2018.10.043.
- [HAS21] HASYLAB. *PETRA III - Facility Information: Brilliant light for DESY users*. 2021.
URL: https://photon-science.desy.de/facilities/petra_iii/facility_information/index_eng.html (visited on March 26, 2022).
- [Hau97] V. Hauk, ed. *Structural and Residual Stress Analysis by Nondestructive Methods: Evaluation - application - assessment*. Amsterdam: Elsevier, 1997.
DOI: 10.1016/B978-0-444-82476-9.X5000-2.
- [He09] B. B. He. *Two-Dimensional X-Ray Diffraction*. Hoboken, NJ, USA: John Wiley & Sons, Inc, 2009.
DOI: 10.1002/9780470502648.
- [Hoc20a] S. Hocine, S. van Petegem, U. Frommherz, G. Tinti, N. Casati, D. Grolimund, and H. van Swygenhoven. “A miniaturized selective laser melting device for operando X-ray diffraction studies”. *Additive Manufacturing* **34** (2020), p. 101194.
DOI: 10.1016/j.addma.2020.101194.
- [Hoc20b] S. Hocine, H. van Swygenhoven, S. van Petegem, C. S. T. Chang, T. Maimaitiyili, G. Tinti, D. Ferreira Sanchez, D. Grolimund, and N. Casati. “Operando X-ray diffraction during laser 3D printing”. *Materials Today* **34** (2020), pp. 30–40.
DOI: 10.1016/j.mattod.2019.10.001.

References

- [Hua20] S. Huang, S. L. Sing, G. de Looze, R. Wilson, and W. Y. Yeong. “Laser powder bed fusion of titanium-tantalum alloys: Compositions and designs for biomedical applications”. *Journal of the mechanical behavior of biomedical materials* **108** (2020), p. 103775.
DOI: 10.1016/j.jmbbm.2020.103775.
- [Jae20] E. J. Jaeschke, S. Khan, J. R. Schneider, and J. B. Hastings, eds. *Synchrotron Light Sources and Free-Electron Lasers*. Cham: Springer International Publishing, 2020.
DOI: 10.1007/978-3-030-23201-6.
- [Kam19] A. M. Kamat and Y. Pei. “An analytical method to predict and compensate for residual stress-induced deformation in overhanging regions of internal channels fabricated using powder bed fusion”. *Additive Manufacturing* **29** (2019), p. 100796.
DOI: 10.1016/j.addma.2019.100796.
- [Kar21] M. Karmuhilan and S. Kumanan. “A Review on Additive Manufacturing Processes of Inconel 625”. *Journal of Materials Engineering and Performance* (2021).
DOI: 10.1007/s11665-021-06427-3.
- [Kin14] W. E. King, H. D. Barth, V. M. Castillo, G. F. Gallegos, J. W. Gibbs, D. E. Hahn, C. Kamath, and A. M. Rubenchik. “Observation of keyhole-mode laser melting in laser powder-bed fusion additive manufacturing”. *Journal of Materials Processing Technology* **214** (2014), pp. 2915–2925.
DOI: 10.1016/j.jmatprotec.2014.06.005.
- [Klu15] J. A. Klug, M. S. Weimer, J. D. Emery, A. Yanguas-Gil, S. Seifert, C. M. Schlepütz, A. B. F. Martinson, J. W. Elam, A. S. Hock, and T. Proslir. “A modular reactor design for in situ synchrotron x-ray investigation of atomic layer deposition processes”. *The Review of scientific instruments* **86** (2015), p. 113901.
DOI: 10.1063/1.4934807.
- [Kor20] A. M. Korsunsky. “Engineering Materials Science Using Synchrotron Radiation”. In: *Synchrotron Light Sources and Free-Electron Lasers*. Ed. by E. J. Jaeschke, S. Khan, J. R. Schneider, and J. B. Hastings. Cham: Springer International Publishing, 2020, pp. 1777–1802.
DOI: 10.1007/978-3-030-23201-6_64.
- [Kor09] A. M. Korsunsky, M. Sebastiani, and E. Bemporad. “Focused ion beam ring drilling for residual stress evaluation”. *Materials Letters* **63** (2009), pp. 1961–1963.
DOI: 10.1016/j.matlet.2009.06.020.
- [Kro22] E. Krohmer. *Dissertation in progress*. Technische Universität Berlin, Institut für Werkzeugmaschinen und Fabrikbetrieb, 2022.
- [Kru12] J.-P. Kruth, J. Deckers, E. Yasa, and R. Wauthlé. “Assessing and comparing influencing factors of residual stresses in selective laser melting using a novel analysis method”. *Proceedings of the Institution of Mechanical Engineers, Part B: Journal of Engineering Manufacture* **226** (2012), pp. 980–991.
DOI: 10.1177/0954405412437085.

- [Kun20] J. Kunz, A. Boontanom, S. Herzog, P. Suwanpinij, A. Kaletsch, and C. Broeckmann. “Influence of hot isostatic pressing post-treatment on the microstructure and mechanical behavior of standard and super duplex stainless steel produced by laser powder bed fusion”. *Materials Science and Engineering: A* **794** (2020), p. 139806.
DOI: 10.1016/j.msea.2020.139806.
- [LeR18] S. Le Roux, M. Salem, and A. Hor. “Improvement of the bridge curvature method to assess residual stresses in selective laser melting”. *Additive Manufacturing* **22** (2018), pp. 320–329.
DOI: 10.1016/j.addma.2018.05.025.
- [Leu18] C. L. A. Leung, S. Marussi, R. C. Atwood, M. Towrie, P. J. Withers, and P. D. Lee. “In situ X-ray imaging of defect and molten pool dynamics in laser additive manufacturing”. *Nature communications* **9** (2018), p. 1355.
DOI: 10.1038/s41467-018-03734-7.
- [Lev19] N. C. Levkulich, S. L. Semiatin, J. E. Gockel, J. R. Middendorf, A. T. DeWald, and N. W. Klingbeil. “The effect of process parameters on residual stress evolution and distortion in the laser powder bed fusion of Ti-6Al-4V”. *Additive Manufacturing* **28** (2019), pp. 475–484.
DOI: 10.1016/j.addma.2019.05.015.
- [Lhu20] P. Lhuissier, X. Bataillon, C. Maestre, J. Sijobert, E. Cabrol, P. Bertrand, E. Boller, A. Rack, J.-J. Blandin, L. Salvo, and G. Martin. “In situ 3D X-ray microtomography of laser-based powder-bed fusion (L-PBF)—A feasibility study”. *Additive Manufacturing* **34** (2020), p. 101271.
DOI: 10.1016/j.addma.2020.101271.
- [Liu16] Y. Liu, Y. Yang, and Di Wang. “A study on the residual stress during selective laser melting (SLM) of metallic powder”. *The International Journal of Advanced Manufacturing Technology* **87** (2016), pp. 647–656.
DOI: 10.1007/s00170-016-8466-y.
- [Lu15] Y. Lu, S. Wu, Y. Gan, T. Huang, C. Yang, L. Junjie, and J. Lin. “Study on the microstructure, mechanical property and residual stress of SLM Inconel-718 alloy manufactured by differing island scanning strategy”. *Optics & Laser Technology* **75** (2015), pp. 197–206.
DOI: 10.1016/j.optlastec.2015.07.009.
- [Lüt07] G. Lütjering and J. C. Williams. *Titanium: With 51 tables*. 2. ed. Engineering materials and processes. Berlin and Heidelberg: Springer, 2007.
- [Mac73] E. Macherauch, H. Wohlfahrt, and U. Wolfstieg. “Zur zweckmäßigen Definition von Eigenspannungen”. *HTM Journal of Heat Treatment and Materials* **28** (1973), pp. 201–211.
DOI: 10.1515/htm-1973-280305.

References

- [Mal21] E. Maleki, S. Bagherifard, M. Bandini, and M. Guagliano. “Surface post-treatments for metal additive manufacturing: Progress, challenges, and opportunities”. *Additive Manufacturing* **37** (2021), p. 101619.
DOI: 10.1016/j.addma.2020.101619.
- [Mar18] G. Marchese, M. Lorusso, S. Parizia, E. Bassini, J.-W. Lee, F. Calignano, D. Manfredi, M. Terner, H.-U. Hong, D. Ugues, M. Lombardi, and S. Biamino. “Influence of heat treatments on microstructure evolution and mechanical properties of Inconel 625 processed by laser powder bed fusion”. *Materials Science and Engineering: A* **729** (2018), pp. 64–75.
DOI: 10.1016/j.msea.2018.05.044.
- [Mat02] M. Matsumoto, M. Shiomi, K. Osakada, and F. Abe. “Finite element analysis of single layer forming on metallic powder bed in rapid prototyping by selective laser processing”. *International Journal of Machine Tools and Manufacture* **42** (2002), pp. 61–67.
DOI: 10.1016/S0890-6955(01)00093-1.
- [Mer06] P. Mercelis and J.-P. Kruth. “Residual stresses in selective laser sintering and selective laser melting”. *Rapid Prototyping Journal* **12** (2006), pp. 254–265.
DOI: 10.1108/13552540610707013.
- [Mos21] M. H. Mosallanejad, B. Niroumand, A. Aversa, D. Manfredi, and A. Saboori. “Laser Powder Bed Fusion in-situ alloying of Ti-5%Cu alloy: Process-structure relationships”. *Journal of Alloys and Compounds* **857** (2021), p. 157558.
DOI: 10.1016/j.jallcom.2020.157558.
- [Moy12] S. Moylan, J. Slotwinski, A. Cooke, K. Jurrens, and M. A. Donmez. “Proposal for a standardized test artifact for additive manufacturing machines and processes”. In: *23rd Annual International Solid Freeform Fabrication Symposium*. Ed. by David L Bourell, Richard H. Crawford, Carolyn C Seepersad, Joseph J. Beaman, and Harris L. Marcus. University of Texas, 2012, pp. 902–920.
- [Muk17] T. Mukherjee, V. Manvatkar, A. De, and T. DebRoy. “Mitigation of thermal distortion during additive manufacturing”. *Scripta Materialia* **127** (2017), pp. 79–83.
DOI: 10.1016/j.scriptamat.2016.09.001.
- [New14] M. Newville, T. Stensitzki, D. B. Allen, and A. Ingargiola. *LMFIT: Non-Linear Least-Square Minimization and Curve-Fitting for Python*. 2014.
DOI: 10.5281/ZENODO.11813.
- [Nor22] G. Nordet, C. Gorny, Y. Mayi, J. Daligault, M. Dal, A. Efferelli, E. Blanchet, F. Coste, and P. Peyre. “Absorptivity measurements during laser powder bed fusion of pure copper with a 1 kW cw green laser”. *Optics & Laser Technology* **147** (2022), p. 107612.
DOI: 10.1016/j.optlastec.2021.107612.
- [Noy87] I. C. Noyan and J. B. Cohen. *Residual Stress: Measurement by Diffraction and Interpretation*. New York, NY: Springer New York, 1987.
DOI: 10.1007/978-1-4613-9570-6.

- [Oh04] M. S. Oh, J.-Y. Lee, and J. K. Park. “Continuous cooling β -to- α transformation behaviors of extra-pure and commercially pure Ti”. *Metallurgical and Materials Transactions A* **35** (2004), pp. 3071–3077.
DOI: 10.1007/s11661-004-0052-5.
- [Ost21] A. Ostovari Moghaddam, N. A. Shaburova, M. N. Samodurova, A. Abdollahzadeh, and E. A. Trofimov. “Additive manufacturing of high entropy alloys: A practical review”. *Journal of Materials Science & Technology* **77** (2021), pp. 131–162.
DOI: 10.1016/j.jmst.2020.11.029.
- [Pat20] S. Patel and M. Vlasea. “Melting modes in laser powder bed fusion”. *Materialia* **9** (2020), p. 100591.
DOI: 10.1016/j.mtl.2020.100591.
- [Per06] PerkinElmer. *XRD 1621 AN/CN Digital X-Ray Detector: Reference Manual: Digital Imaging*. 2006.
URL: https://www.aps.anl.gov/files/APS-Uploads/DET/Detector-Pool/Area-Detectors/PerkinElmer/Manual_PKIaSi_XRD1621_2008-07-30.pdf (visited on March 26, 2022).
- [Pha20] M.-S. Pham, B. Dovggy, P. A. Hooper, C. M. Gurlay, and A. Piglione. “The role of side-branching in microstructure development in laser powder-bed fusion”. *Nature communications* **11** (2020), p. 749.
DOI: 10.1038/s41467-020-14453-3.
- [Pha19] T. Q. Phan, M. Strantza, M. R. Hill, T. H. Gnaupel-Herold, J. Heigel, C. R. D’Elia, A. T. DeWald, B. Clausen, D. C. Pagan, J. Y. Peter Ko, D. W. Brown, and L. E. Levine. “Elastic Residual Strain and Stress Measurements and Corresponding Part Deflections of 3D Additive Manufacturing Builds of IN625 AM-Bench Artifacts Using Neutron Diffraction, Synchrotron X-Ray Diffraction, and Contour Method”. *Integrating Materials and Manufacturing Innovation* **8** (2019), pp. 318–334.
DOI: 10.1007/s40192-019-00149-0.
- [Pis21] J. Pistor, C. Breuning, and C. Körner. “A Single Crystal Process Window for Electron Beam Powder Bed Fusion Additive Manufacturing of a CMSX-4 Type Ni-Based Superalloy”. *Materials (Basel, Switzerland)* **14** (2021).
DOI: 10.3390/ma14143785.
- [Pri13] M. B. Prime and A. T. DeWald. “The Contour Method”. In: *Practical Residual Stress Measurement Methods*. Ed. by G. S. Schajer. Chichester, UK: John Wiley & Sons, Ltd, 2013, pp. 109–138.
DOI: 10.1002/9781118402832.ch5.
- [Rai07] R. Rai, J. W. Elmer, T. A. Palmer, and T. DebRoy. “Heat transfer and fluid flow during keyhole mode laser welding of tantalum, Ti–6Al–4V, 304L stainless steel and vanadium”. *Journal of Physics D: Applied Physics* **40** (2007), pp. 5753–5766.
DOI: 10.1088/0022-3727/40/18/037.

References

- [Raz21] A. Raza, T. Fiegl, I. Hanif, A. Markström, M. Franke, C. Körner, and E. Hryha. “Degradation of AlSi10Mg powder during laser based powder bed fusion processing”. *Materials & Design* **198** (2021), p. 109358.
DOI: 10.1016/j.matdes.2020.109358.
- [Reh05] O. Rehme and C. Emmelmann. “Reproducibility for properties of selective laser melting products”. In: *Lasers in manufacturing 2005*. Ed. by E. Beyer. Stuttgart: AT-Fachverl., 2005, pp. 227–232.
- [Rei08] W. Reimers, A. R. Pyzalla, A. K. Schreyer, and H. Clemens. *Neutrons and Synchrotron Radiation in Engineering Materials Science: From fundamentals to material and component characterization*. Weinheim and Chichester: Wiley, 2008.
DOI: 10.1002/9783527621927.
- [Rob15] A. L. Robinson. “History of Synchrotron Radiation”. *Synchrotron Radiation News* **28** (2015), pp. 4–9.
DOI: 10.1080/08940886.2015.1059228.
- [Rob18] J. Robinson, I. Ashton, P. Fox, E. Jones, and C. Sutcliffe. “Determination of the effect of scan strategy on residual stress in laser powder bed fusion additive manufacturing”. *Additive Manufacturing* **23** (2018), pp. 13–24.
DOI: 10.1016/j.addma.2018.07.001.
- [Sae15] K. Saeidi, X. Gao, Y. Zhong, and Z. J. Shen. “Hardened austenite steel with columnar sub-grain structure formed by laser melting”. *Materials Science and Engineering: A* **625** (2015), pp. 221–229.
DOI: 10.1016/j.msea.2014.12.018.
- [San20] E. Santecchia, S. Spigarelli, and M. Cabibbo. “Material Reuse in Laser Powder Bed Fusion: Side Effects of the Laser—Metal Powder Interaction”. *Metals* **10** (2020), p. 341.
DOI: 10.3390/met10030341.
- [Sch13] N. Schell, A. King, F. Beckmann, T. Fischer, M. Müller, and A. Schreyer. “The High Energy Materials Science Beamline (HEMS) at PETRA III”. *Materials Science Forum* **772** (2013), pp. 57–61.
DOI: 10.4028/www.scientific.net/MSF.772.57.
- [P3] F. Schmeiser, E. Krohmer, C. Wagner, N. Schell, E. Uhlmann, and W. Reimers. “In situ microstructure analysis of Inconel 625 during laser powder bed fusion”. *Journal of Materials Science* **57** (2022), pp. 9663–9677.
DOI: 10.1007/s10853-021-06577-8.
- [Sch21] J. Schröder, A. Evans, T. Mishurova, A. Ulbricht, M. Sprengel, I. Serrano-Munoz, T. Fritsch, A. Kromm, T. Kannengießner, and G. Bruno. “Diffraction-Based Residual Stress Characterization in Laser Additive Manufacturing of Metals”. *Metals* **11** (2021), p. 1830.
DOI: 10.3390/met11111830.

- [Sci17] U. Scipioni Bertoli, G. Guss, S. Wu, M. J. Matthews, and J. M. Schoenung. “In-situ characterization of laser-powder interaction and cooling rates through high-speed imaging of powder bed fusion additive manufacturing”. *Materials & Design* **135** (2017), pp. 385–396.
DOI: 10.1016/j.matdes.2017.09.044.
- [Ser21] I. Serrano-Munoz, A. Evans, T. Mishurova, M. Sprengel, T. Pirling, A. Kromm, and G. Bruno. “The Importance of Subsurface Residual Stress in Laser Powder Bed Fusion IN718”. *Advanced Engineering Materials* (2021), p. 2100895.
DOI: 10.1002/adem.202100895.
- [Sha01] V. Shankar, K. Bhanu Sankara Rao, and S. Mannan. “Microstructure and mechanical properties of Inconel 625 superalloy”. *Journal of Nuclear Materials* **288** (2001), pp. 222–232.
DOI: 10.1016/S0022-3115(00)00723-6.
- [Shi04] M. Shiomi, K. Osakada, K. Nakamura, T. Yamashita, and F. Abe. “Residual Stress within Metallic Model Made by Selective Laser Melting Process”. *CIRP Annals* **53** (2004), pp. 195–198.
DOI: 10.1016/S0007-8506(07)60677-5.
- [Shm06] U. Shmueli, H. Fuess, T. Hahn, H. Wondratschek, U. Müller, E. Prince, A. Authier, V. Kopský, D. B. Litvin, M. G. Rossmann, E. Arnold, S. Hall, and B. McMahon. *International Tables for Crystallography*. Vol. B. Chester, England: International Union of Crystallography, 2006.
DOI: 10.1107/97809553602060000102.
- [Son20] X. Song, S. Feih, W. Zhai, C.-N. Sun, F. Li, R. Maiti, J. Wei, Y. Yang, V. Oancea, L. Romano Brandt, and A. M. Korsunsky. “Advances in additive manufacturing process simulation: Residual stresses and distortion predictions in complex metallic components”. *Materials & Design* **193** (2020), p. 108779.
DOI: 10.1016/j.matdes.2020.108779.
- [Spi19] L. Spieß, G. Teichert, R. Schwarzer, H. Behnken, and C. Genzel. *Moderne Röntgenbeugung*. Wiesbaden: Springer Fachmedien Wiesbaden, 2019.
DOI: 10.1007/978-3-8348-8232-5.
- [Sun18] Z. Sun, X. Tan, S. B. Tor, and C. K. Chua. “Simultaneously enhanced strength and ductility for 3D-printed stainless steel 316L by selective laser melting”. *NPG Asia Materials* **10** (2018), pp. 127–136.
DOI: 10.1038/s41427-018-0018-5.
- [Tay21] H. C. Taylor, E. A. Garibay, and R. B. Wicker. “Toward a common laser powder bed fusion qualification test artifact”. *Additive Manufacturing* **39** (2021), p. 101803.
DOI: 10.1016/j.addma.2020.101803.
- [Tia20a] Y. Tian, R. Palad, and C. Aranas. “Microstructural evolution and mechanical properties of a newly designed steel fabricated by laser powder bed fusion”. *Additive Manufacturing* **36** (2020), p. 101495.
DOI: 10.1016/j.addma.2020.101495.

References

- [Tia20b] Z. Tian, C. Zhang, D. Wang, W. Liu, X. Fang, D. Wellmann, Y. Zhao, and Y. Tian. “A Review on Laser Powder Bed Fusion of Inconel 625 Nickel-Based Alloy”. *Applied Sciences* **10** (2020), p. 81.
DOI: 10.3390/app10010081.
- [Uhl17] E. Uhlmann, E. Krohmer, F. Hohlstein, and W. Reimers. “Development of an experimental setup for in situ strain evaluation during Selective Laser melting”. In: *Proceedings of the 28th Annual International Solid Freeform Fabrication Symposium*. 2017, pp. 1472–1480.
- [Uhl20] E. Uhlmann, E. Krohmer, F. Schmeiser, N. Schell, and W. Reimers. “A laser powder bed fusion system for in situ x-ray diffraction with high-energy synchrotron radiation”. *The Review of scientific instruments* **91** (2020), p. 075104.
DOI: 10.1063/1.5143766.
- [Voi21] T. Voisin, J.-B. Forien, A. Perron, S. Aubry, N. Bertin, A. Samanta, A. Baker, and Y. M. Wang. “New insights on cellular structures strengthening mechanisms and thermal stability of an austenitic stainless steel fabricated by laser powder-bed-fusion”. *Acta Materialia* **203** (2021), p. 116476.
DOI: 10.1016/j.actamat.2020.11.018.
- [Vra14] B. Vrancken, V. Cain, R. Knutsen, and J. van Humbeeck. “Residual stress via the contour method in compact tension specimens produced via selective laser melting”. *Scripta Materialia* **87** (2014), pp. 29–32.
DOI: 10.1016/j.scriptamat.2014.05.016.
- [Wah19] B. Wahlmann, F. Galgon, A. Stark, S. Gayer, N. Schell, P. Staron, and C. Körner. “Growth and coarsening kinetics of gamma prime precipitates in CMSX-4 under simulated additive manufacturing conditions”. *Acta Materialia* **180** (2019), pp. 84–96.
DOI: 10.1016/j.actamat.2019.08.049.
- [Wah21] B. Wahlmann, E. Krohmer, C. Breuning, N. Schell, P. Staron, E. Uhlmann, and C. Körner. “In Situ Observation of γ' Phase Transformation Dynamics During Selective Laser Melting of CMSX-4”. *Advanced Engineering Materials* **23** (2021), p. 2100112.
DOI: 10.1002/adem.202100112.
- [Wak20] Y. Wakai, T. Ogura, S. Nakano, N. Sato, S. Kajino, and S. Suzuki. “Melting behavior in laser powder bed fusion revealed by in situ X-ray and thermal imaging”. *The International Journal of Advanced Manufacturing Technology* **110** (2020), pp. 1047–1059.
DOI: 10.1007/s00170-020-05828-3.
- [Wal21] J. Walker, J. R. Middendorf, C. C. Lesko, and J. Gockel. “Multi-material laser powder bed fusion additive manufacturing in 3-dimensions”. *Manufacturing Letters* (2021).
DOI: 10.1016/j.mfglet.2021.07.011.

- [Wan19] X. Wang and K. Chou. “The effects of stress relieving heat treatment on the microstructure and residual stress of Inconel 718 fabricated by laser metal powder bed fusion additive manufacturing process”. *Journal of Manufacturing Processes* **48** (2019), pp. 154–163.
DOI: 10.1016/j.jmapro.2019.10.027.
- [Wan20] Y. Wang, C. Yu, L. Xing, K. Li, J. Chen, W. Liu, J. Ma, and Z. Shen. “Grain structure and texture of the SLM single track”. *Journal of Materials Processing Technology* **281** (2020), p. 116591.
DOI: 10.1016/j.jmatprotec.2020.116591.
- [Wan17] Z. Wang, E. Denlinger, P. Michaleris, A. D. Stoica, D. Ma, and A. M. Beese. “Residual stress mapping in Inconel 625 fabricated through additive manufacturing: Method for neutron diffraction measurements to validate thermomechanical model predictions”. *Materials & Design* **113** (2017), pp. 169–177.
DOI: 10.1016/j.matdes.2016.10.003.
- [Was62] G. Wassermann and J. Grewen. *Texturen metallischer Werkstoffe*. Zweite, neubearbeitete und erweiterte Auflage. Berlin, Heidelberg: Springer Berlin Heidelberg, 1962.
DOI: 10.1007/978-3-662-13128-2.
- [Wei16] H. L. Wei, J. W. Elmer, and T. DebRoy. “Origin of grain orientation during solidification of an aluminum alloy”. *Acta Materialia* **115** (2016), pp. 123–131.
DOI: 10.1016/j.actamat.2016.05.057.
- [Wil18] R. J. Williams, C. M. Davies, and P. A. Hooper. “A pragmatic part scale model for residual stress and distortion prediction in powder bed fusion”. *Additive Manufacturing* **22** (2018), pp. 416–425.
DOI: 10.1016/j.addma.2018.05.038.
- [Wit07] P. J. Withers, M. Preuss, A. Steuwer, and J. W. L. Pang. “Methods for obtaining the strain-free lattice parameter when using diffraction to determine residual stress”. *Journal of Applied Crystallography* **40** (2007), pp. 891–904.
DOI: 10.1107/S0021889807030269.
- [Woh20] T. Wohlers, I. Campbell, O. Diegel, R. Huff, and J. Kowen. *Wohlers Report 2020: 3D Printing and Additive Manufacturing Global State of the Industry*. 2020.
- [Xia20] Z. Xiao, C. Chen, H. Zhu, Z. Hu, B. Nagarajan, L. Guo, and X. Zeng. “Study of residual stress in selective laser melting of Ti6Al4V”. *Materials & Design* **193** (2020), p. 108846.
DOI: 10.1016/j.matdes.2020.108846.
- [Yad21] I. Yadroitsev, I. Yadroitsava, A. Du Plessis, and E. MacDonald, eds. *Fundamentals of Laser Powder Bed Fusion of Metals*. Additive manufacturing materials and technologies. Amsterdam, Kidlington, Oxford, and Cambridge, MA: Elsevier, 2021.
DOI: 10.1016/C2020-0-01200-4.

References

- [Yap15] C. Y. Yap, C. K. Chua, Z. L. Dong, Z. H. Liu, D. Q. Zhang, L. E. Loh, and S. L. Sing. “Review of selective laser melting: Materials and applications”. *Applied Physics Reviews* **2** (2015), p. 041101.
DOI: 10.1063/1.4935926.
- [Yin18] J. Yin, G. Peng, C. Chen, J. Yang, H. Zhu, L. Ke, Z. Wang, D. Wang, M. Ma, G. Wang, and X. Zeng. “Thermal behavior and grain growth orientation during selective laser melting of Ti-6Al-4V alloy”. *Journal of Materials Processing Technology* **260** (2018), pp. 57–65.
DOI: 10.1016/j.jmatprotec.2018.04.035.
- [Zaf21] A. Zafari and K. Xia. “Laser powder bed fusion of ultrahigh strength Fe-Cu alloys using elemental powders”. *Additive Manufacturing* **47** (2021), p. 102270.
DOI: 10.1016/j.addma.2021.102270.
- [Zha18] D. Zhang, S. Sun, D. Qiu, M. A. Gibson, M. S. Dargusch, M. Brandt, M. Qian, and M. Easton. “Metal Alloys for Fusion-Based Additive Manufacturing”. *Advanced Engineering Materials* **20** (2018), p. 1700952.
DOI: 10.1002/adem.201700952.
- [Zha21] T. Zhang and C.-T. Liu. “Design of titanium alloys by additive manufacturing: A critical review”. *Advanced Powder Materials* (2021), p. 100014.
DOI: 10.1016/j.apmate.2021.11.001.
- [Zha17] C. Zhao, K. Fezzaa, R. W. Cunningham, H. Wen, F. de Carlo, L. Chen, A. D. Rollett, and T. Sun. “Real-time monitoring of laser powder bed fusion process using high-speed X-ray imaging and diffraction”. *Scientific reports* **7** (2017), p. 3602.
DOI: 10.1038/s41598-017-03761-2.
- [Zwi74] U. Zwicker. *Titan und Titanlegierungen*. 1st ed. 1974. Vol. 21. Reine und angewandte Metallkunde in Einzeldarstellungen. Berlin, Heidelberg: Springer Berlin Heidelberg, 1974.
DOI: 10.1007/978-3-642-80587-5.

Standards and guidelines

- [E DIN 8580] Fertigungsverfahren – Begriffe, Einteilung (E DIN 8580:2020-01)

Full list of publications and related works

Publications in peer-reviewed journals as first author:

- F. Schmeiser, E. Krohmer, N. Schell, E. Uhlmann, and W. Reimers. “Experimental observation of stress formation during selective laser melting using in situ X-ray diffraction”. *Additive Manufacturing* **32** (2020), p. 101028.
DOI: 10.1016/j.addma.2019.101028
- F. Schmeiser, E. Krohmer, N. Schell, E. Uhlmann, and W. Reimers. “Internal Stress Evolution and Subsurface Phase Transformation in Titanium Parts Manufactured by Laser Powder Bed Fusion—An in situ X-ray Diffraction Study”. *Advanced Engineering Materials* **23** (2021), p. 2001502.
DOI: 10.1002/adem.202001502
- F. Schmeiser, E. Krohmer, C. Wagner, N. Schell, E. Uhlmann, and W. Reimers. “In situ Microstructure Analysis of Inconel 625 during Laser Powder Bed Fusion”. *Journal of Materials Science* **57** (2022), p. 9663-9677.
DOI: 10.1007/s10853-021-06577-8

Publications in peer-reviewed journals as co-author:

- E. Uhlmann, E. Krohmer, F. Schmeiser, N. Schell, and W. Reimers. “A laser powder bed fusion system for in situ x-ray diffraction with high-energy synchrotron radiation”. *Review of Scientific Instruments* **91**(7) (2021), p. 075104.
DOI: 10.1063/1.5143766
- E. Krohmer, F. Schmeiser, B. Wahlmann, J. Rosigkeit, G. Graf, P. Spoerk-Erdely, H. Clemens, P. Staron, C. Körner, W. Reimers, and E. Uhlmann. “Revealing dynamic processes in laser powder bed fusion with *in situ* X-ray diffraction at PETRA III”. *Review of Scientific Instruments* (2022).
DOI: 10.1063/5.0077105

Presentations and other publications:

- F. Schmeiser, E. Krohmer, E. Uhlmann, and W. Reimers. “In-situ experiment for selective laser melting”. GEMS Satellite Workshop (DESY Users Meeting). January 25, 2019, Hamburg, Germany (Invited presentation)
- F. Schmeiser, E. Krohmer, E. Uhlmann, and W. Reimers. “In situ Synchrotron-Röntgenbeugung zur Analyse der Eigenspannungsentwicklung bei der additiven Fertigung”. Arbeitsgemeinschaft Wärmebehandlung + Werkstofftechnik e. V. - Fachausschuss Eigenspannungen, Fall Meeting, November 5-6, 2019, Untermerzbach, Germany (Presentation)

Full list of publications and related works

- F. Schmeiser. “Stressed-out metal 3D printing — Laser-induced internal stresses revealed during printing”. Photon Science - Highlights and Annual Report 2020. DESY. 2020 (Invited article)
- F. Schmeiser, E. Krohmer, E. Uhlmann, and W. Reimers. “In-Situ Stress and Texture Analysis during Selective Laser Melting”. THERMEC 2021. June 1-5, 2021, Graz, Austria (Invited presentation)
- F. Schmeiser, E. Krohmer, E. Uhlmann, and W. Reimers. “In situ stress analysis during laser powder bed fusion using synchrotron radiation diffraction”. 11th International Conference on Residual Stresses 2022. March 27-30, 2022, Nancy, France (Presentation)

Acknowledgements

Danksagung

Die vorliegende Arbeit entstand während meiner Tätigkeit als wissenschaftlicher Mitarbeiter am Fachgebiet Metallische Werkstoffe an der Technischen Universität Berlin. Bei der Anfertigung der Arbeit wurde ich von vielen Menschen unterstützt, denen ich an dieser Stelle meinen Dank aussprechen möchte.

Zunächst danke ich Herrn Prof. Dr. Reimers für den Themenvorschlag, das stetige Interesse an meinem Fortschritt und die spannenden Diskussionen zu inhaltlichen Fragen. Seine Erfahrung, sein unermüdlicher Einsatz und seine Ideen haben mir wichtige Impulse für die Entwicklung von Problemlösungen im Laufe meiner Arbeit gegeben. Darüber hinaus danke ich ihm für die Begutachtung dieser Dissertation.

Herrn Prof. Dr. Genzel danke ich herzlich für die Übernahme eines Gutachtens und das Interesse an dieser Arbeit. Bei Herrn Priv.-Doz. Dr. Müller bedanke ich mich besonders für die Übernahme des Vorsitzes im Promotionsausschuss.

Außerdem danke ich der Deutschen Forschungsgemeinschaft (DFG) für die Förderung des Projektes Nr. 317078200.

Durch die gemeinsame Projektbearbeitung war Erwin Krohmer mein erster und wichtigster Ansprechpartner in allen LPBF-Belangen. Für die immer konstruktive, zielorientierte, zuverlässige und angenehme Zusammenarbeit sowie seine im wahrsten Sinne unermüdliche Arbeit bei den Messzeiten bin ich ihm sehr dankbar.

Meinen Kollegen am Fachgebiet Metallische Werkstoffe danke ich für die tolle Arbeitsatmosphäre und die gegenseitige Unterstützung. Ich bedanke mich bei Bettina Camin für die vielfältige Hilfe bei Messzeiten und allerlei anderen Angelegenheiten. Bei Sabine Quander möchte ich mich dafür bedanken, dass sie den Durchblick in allen Verwaltungsangelegenheiten hat. Alexander Treff danke ich für die Unterstützung in der Lehre. Alexander Poeche danke ich für die Messzeitunterstützung und die Diskussionen zu Python und allen anderen Themen. Mateus Dobecki danke ich für unzählige Messzeit-Nachtschichten, kritische fachliche Diskussionen und seinen hellen Kopf. Abschließend bedanke ich mich bei Jonas Schmidt für seine hartnäckig gute Laune, seine technischen Fähigkeiten und die immer humorvolle Zusammenarbeit.

Seit wir uns im Sommersemester 2012 im Bachelor-Studium kennengelernt haben, ist David Karl für mich eine große Inspiration in Sachen Kreativität, Selbstwirksamkeit und Eigeninitiative. Auch bei der Erstellung dieser Arbeit stand er mir stets mit Rat und Tat beiseite. Dafür möchte ich mich bei ihm bedanken.

Acknowledgements

Folgenden ZELMI-Mitarbeitern möchte ich für die Unterstützung bei diversen Charakterisierungsfragestellungen danken: Christoph Fahrenson für EBSD-Messungen, Jörg Nissen für die WDX-Untersuchungen, Christian Günther für die FIB-Präparation und Sören Selve für die TEM-Messungen.

Am Helmholtz-Zentrum Hereon möchte ich mich bei Norbert Schell, Jan Rosigkeit, Emad Mawaad, Jens Brehling, Ursula Tietz und Peter Staron für die großartige Unterstützung und das großzügige Entgegenkommen bei der Umsetzung unserer Messzeiten bedanken. Thorsten Hasenkamp vom DESY darf nicht unerwähnt bleiben. Ohne ihn wären die Messungen an der Seitenstation nicht möglich gewesen.

Bei der technischen Umsetzung der Experimente für diese Arbeit wäre ich ohne die tatkräftige Unterstützung vieler weiterer helfender Hände verloren gewesen. Mein Dank gilt Amadeus Pauer, Henry Angerstein, Matthias Schelhorn, Thomas Braun und Wilhelm Schulze. Für die tolle Zusammenarbeit und Unterstützung möchte ich Francisca Oberdiek, Simon Banhart und Felix Volk danken. Besonders hervorheben möchte ich Christian Wagner und Anton Thiel, die mit Fleiß, Wissen und Interesse hervorragende Abschlussarbeiten hervorgebracht und dadurch auch meine eigene Forschung erheblich vorangetrieben haben.

Abgesehen von der umfangreichen fachlichen Unterstützung, die ich erfahren habe, hätte diese Arbeit ohne die Menschen in meinem Umfeld nicht entstehen können. Meiner Familie, meinen Freunden, und besonders Cheyenne danke ich von ganzem Herzen für den Rückhalt während dieser Zeit.